Alma Mater Studiorum · University of Bologna

School of Science
Department of Physics and Astronomy
Master Degree in Physics

Study of $^{18}O+^{12,13}C$ fusion-evaporation reactions with the GARFIELD array

Supervisor:
Prof. Cristian Massimi

Co-supervisors:
Dr. Magda Cicerchia
Dr. Alberto Mengarelli

Submitted by:
Maria Vittoria Managlia

Academic Year 2020/2021

To Professor Mauro Bruno

Contents

Introduction

The study of medium-mass nuclei decay is one of the active areas of research in nuclear physics. In particular, the emission of light charged particles from fusion-evaporation nuclear reactions induced by light and medium-mass nuclei are analyzed at low energy (above the Coulomb barrier but below the 100 MeV/u) by the NUCL-EX collaboration [1]. In various works of the collaboration ([2]-[4]), the experimental data are compared with statistical code in order to verify the statistical behaviour of those reactions. In case of reactions where α-conjugated nuclei are involved some discrepancies between experimental and simulated data are observed in the decay channels with even residues, mainly if it is in coincidence with α particles. Such discrepancies are explained as related to the structure of the reaction partners and/or to the compound nucleus (CN). For a deeper investigation of this effect, the INFN NUCL-EX collaboration has recently proposed and carried out the ISOLIGHT experiment at the Legnaro National Laboratories using the GARFIELD+RCo setup. It was based on the study of three different reactions: ^{18}O+^{13}C at 112.5 MeV and ^{18}O+^{12}C at 122 and 300 MeV. The first two reactions produce two compound nuclei, ^{30}Si* and ^{31}Si* respectively, with the same excitation energy. Their comparison allows to investigate how the CN decay depends on the neutron excess in the system. In order to better highlight this dependence a further comparison could be made with the data of a previous NUCL-EX experiment in which the CN (^{28}Si*) was produced at the same excitation energy through the fusion of ^{16}O+^{12}C [4]. The third reaction is carried out at a higher energy: 300 MeV. The study of the comparison of the two reactions induced by ^{16}O+^{12}C at different energies, being the formed CN the same, permits to evidence the dependence of the CN decay mechanisms on the excitation energy.

The data taking of the ISOLIGHT experiment took place in two different phases: a first one in January 2020 for the ^{18}O+^{12}C at 300 MeV reaction and a second one in February 2021 for the reactions ^{18}O+^{13}C at 112.5 MeV and ^{18}O+^{12}C at 122 MeV.

In order to obtain experimental calibrated data available for data analysis, several steps must be strictly followed. Typically these include: the check of the electronic stability of the apparatus; the energy calibration of the detectors to obtain a conversion factor between the measured energy of the detected particles expressed in channels and in energy expressed in MeV; and the particle identification enabling to reconstruct the

dynamics of the interaction and recreate the characteristics of the produced particles starting from the detectors signals. The latter is an extremely time-consuming process due to the high number of detectors employed in the GARFIELD array.

Once experimental data are available, a comparison with the simulations can be performed. Simulations, however, are also used to understand where specific reaction mechanisms should be expected. Since in low energy reactions a prevailing fusion-evaporation mechanism is expected, GEMINI++ and HFℓ statistical decay codes simulating the evaporation mechanism from the compound nucleus are exploited.

The purpose of this thesis is to go across the various steps of a typical nuclear experiment conducted with the GARFIELD array: starting from the data taking, passing through the experimental data reconstruction (data cleaning, calibration, particle identification), concluding with a comparative analysis using a simulation code. Unfortunately, the complete experimental data reconstruction is still going on, therefore no experimental reconstructed data are reported in this work. This thesis is outlined as follows. In Chapter 1 a theoretical introduction of nuclear reaction mechanisms is reported with particular attention to fusion-evaporation reactions. Chapter 2 provides a detailed introduction of the GARFIELD+RCo multi-detector. Chapter 3 describes the details of the ISOLIGHT experiment, highlighting in particular the adopted procedures for the energy calibration and the particle identification. In Chapter 4 the simulation codes are described and the analysis of the simulated data is reported. The three reactions under study are simulated with the GEMINI++ code. This code, describing the decay from a hot source, is an ideal tool for taking into account the fusion-evaporation mechanism of the interaction. In order to show the effect of the GARFIELD detector on data, a software filter reproducing all the GARFIELD characteristics (energy threshold, angular coverage, ect.) is applied to the simulated data. These effects are analyzed in the single case of the ^{18}O+^{12}C reaction at 122 MeV. Particular attention is paid to the selection of complete events for a future comparison with experimental data once they will be fully reconstructed. In a following section, the three reactions are compared in order provide a general overview of their statistical behavior in the two cases:

- fusion-evaporation events produced with GEMINI++,
- complete (in charge) fusion-evaporation events after the application of the experimental apparatus filter.

Then, the events are simulated with an additional statistical code: HFℓ, developed within the NUCL-EX collaboration. The comparison of the GEMINI++ and HFl simulations for the ^{18}O+^{12}C reaction at 122 MeV is accomplished to point out possible differences in the description of the same fusion-evaporation reaction with the two codes. Eventually, for sake of completeness, Appendix A illustrates the analysis on the commissioning experiment carried out in January 2020 in order to test the performance of the GARFIELD electronics update.

Chapter 1

Nuclear reaction mechanisms

Atomic nuclei are quantum systems of particles called *nucleons* which can be distinguished in protons and neutrons. What binds these particles together inside nuclei is the so-called *nuclear force*, a short-range and sufficiently intense force to overcome the long-range Coulomb repulsion. Nucleons, in turn, are ultimately constituted by quarks and gluons. However, as long as the considered energy deposited in the system is not sufficient to excite sub-nucleonic degrees of freedom, it makes sense to consider nucleons as the effective elementary constituents of nuclei. This assumption of nuclei as sets of interacting nucleons constitutes the basis of most studies aimed at understanding the structure and dynamical properties of nuclear matter. The energy range in which this assumption is valid is referred to as *nucleonic regime*.

Ground-state nuclei provide poor information on nuclear matter. Therefore, nuclei must be excited to enable the investigation of large regions of the nuclear matter phase diagram and heavy-ion collisions result to be a unique tool in doing this. Depending on the initial conditions, extreme densities and temperatures can be reached in these collisions and reaction products can be either highly exotic[1] or hot[2] nuclei.

This chapter outlines the physical context in which the study reported in this thesis fits. Particular attention has been payed to heavy-ion collisions and their classifications (Sec.1.1) in terms of energy and impact parameter. In Sec.1.2 the elastic scattering process is described and Sec.1.3 is focused on fusion-evaporation reactions with a more detailed description of complete fusion and compound nucleus decay in Subsec.1.3.1 and Subsec.1.3.2, respectively.

[1]Nuclei with a very large number of nucleons (superheavy elements) or with unusual neutron/protons ratios.

[2]Nuclei with excitation energy close to or even higher than their total binding energies.

1.1 Heavy-ion collisions

In nuclear physics the term *nuclear reaction* refers to a process in which two nuclei interact exchanging momentum, energy and/or matter. In general, we speak of *scattering* process if the incident and outgoing particles are the same: if the outgoing particles are in their ground states, the interaction is referred to as *elastic* collision, in the opposite case as *inelastic* collision. On the other hand, when an exchange of matter takes place, the nucleus of a specific chemical element is converted into another with different atomic number. This conversion can be either due to a spontaneous change (*radioactive decays*) in the nucleus or induced by external means, i.e. *nuclear collisions*. In the latter case, an energetic projectile nucleus (*beam*) bombards another nucleus (*target*) which is normally at rest in the laboratory frame. In this interaction, reaction products such as other nuclei or nuclear composites are emitted. If the projectile has $A \geq 4$ we speak of *heavy-ion collisions* [5]. A conventional notation is normally adopted to represent the reaction mechanisms:

$$a + X \rightarrow Y + b \tag{1.1}$$

where a stands for the incident particle, X is the target nucleus and Y and b are the reaction products (usually, Y being the recoiling nucleus and b the outgoing particle). However, in some cases it might be convenient to use an alternative and more compact notation:

$$X(a, b)Y \tag{1.2}$$

for an immediate recognition of the common properties of a general class of reactions.

Nuclear collisions can be classified according to some global features [6]. The first one is the relative velocity v_{rel} between projectile and target before the impact. This speed is an index of the available center-of-mass kinetic energy that can be partially or entirely transformed into excitation energy during the interaction between the two colliding nuclei. The corresponding reduced wavelength related to the nucleon-nucleon interaction is given by:

$$\lambda = \frac{h}{m v_{rel}} \tag{1.3}$$

where m is the nucleon mass and h the Planck constant. Comparing λ with the mean nucleon-nucleon distance d_{n-n} ($\sim 2fm$) in a nucleus, two cases can be distinguished:

- $\lambda > d_{n-n}$. In this case, a single nucleon is affected by the average interaction due to the presence of all the other nucleons and not by single collisions between nucleons. In other words, a collective behaviour of nucleons during the collision is expected and the interaction can be described via a mean-field potential, i.e. one-body interaction.

- $\lambda < d_{n-n}$. In such a case, instead, the binding energy of nucleons becomes negligible. The target cannot be treated as a collective entity and the two-body interaction

is used to explain the process.

Actually, mean-field and nucleon-nucleon collision effects are always present, but one can be considered dominant on the other depending on the case under study. Another important and useful parameter to classify reaction mechanisms is the *impact parameter* b (Fig. 1.1) which is the distance between the asymptotic trajectory of the projectile and

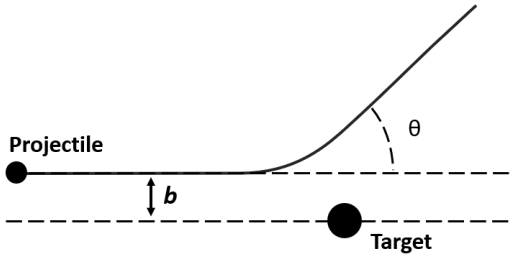

Figure 1.1: Sketch of an elastic scattering collision. b denotes the impact parameter and θ is the scattering angle of the projectile.

the parallel line passing through the center of the target. It is straightforward to notice that as the impact parameter decreases, the overlap of the density distributions of the nuclei during the collision increases. The minimum value of b for which nuclear forces are negligible with respect to the Coulomb interaction is known as "grazing" impact parameter b_{gr}. Roughly, this can be thought as the sum of target and projectile radii $b_{gr} \sim R_T + R_P$. Reactions with $b = b_{gr}$ are known as *grazing collisions*. When $b > b_{gr}$ elastic scattering occurs since the Coulomb interaction is dominant due to the large distance between target and projectile. On the other hand, if $b < b_{gr}$, nucleons begin to feel the strong interaction and the process becomes inelastic.

In the following subsections the main reaction mechanisms involving heavy ions in the different energy regions as a function of the impact parameter are described.

1.1.1 Mean field energy range

In the energy range below 15 MeV per nucleon (MeV/u), different reaction mechanisms can occur. In case of central collisions ($b \sim 0$), the impact between projectile and target can lead to their fusion. The reaction product is what is called a *compound nucleus* (CN), a metastable system with an average life of about $10^{-19} \div 10^{-18}$ s [7]. The evolution of this system does not depend on how it was produced. Once the CN reaches the thermal and chemical equilibrium, a de-excitation phase follows with its subsequent decay. In peripheral collisions ($b \leq b_{gr}$), instead, only very few nucleons are involved in the interaction. Namely, the most superficial nucleons of the projectile primarily interact at the surface of the target nucleus, with the remaining nucleons of

both partners serving as passive spectators. Reactions with this feature are called *direct reactions*. As a consequence, only small amounts of energy can be exchanged by the most peripheral nucleons. Contrary to the compound nucleus reaction, in this case the reaction products have a "memory" of the entrance channel and the reaction products are similar to the projectile and to the target; therefore, they are called *quasi projectile* (QP) and *quasi target* (QT), respectively.

Finally, at larger b ($b \sim b_{graz}$), the interaction between projectile and target is minimal. Only few nucleons are transferred between the two colliding partners which are only slightly perturbed.

Since in a semiclassical approach b is related to the *orbital angular momentum* l by:

$$b = l\lambda \tag{1.4}$$

in the lower energy regime, the various reaction processes can be also classified as a function of l. According to Eq.1.4, the grazing angular momentum l_{gr} is associated to b_{gr}. Fig. 1.2 shows the different reaction mechanisms for different values of l. For instance,

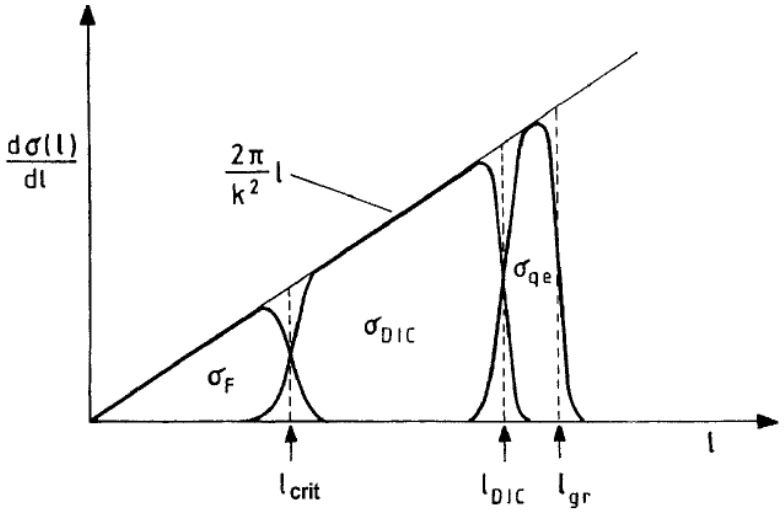

Figure 1.2: Schematic diagram of the contribution of the various reactions to the differential cross section as a function of the values of l in low incident energy heavy-ion reactions.

the values $l < l_{crit}$[3] identify the region of CN formation following the complete fusion of the reaction reagents (σ_F). Values between l_{crit} and l_{DIC} determine the region of deep inelastic collisions (DIC) (σ_{DIC}), a process in which the two partners re-separate after a contact phase during which matter and a significant amount of energy are exchanged.

[3] l_{crit} is the *critical angular momentum* and separates the processes of inelastic dissipation and of fusion.

Finally, $l_{DIC} < l < l_{gr}$ corresponds to the "quasi-elastic" collisions region (σ_{qe}) while higher values of l identify elastic scattering processes (σ_e).

1.1.2 Fermi energy range

The expression "Fermi energy domain" refers to energies between 15 and 200 MeV/u, a transition region in which both two-body and one-body mechanisms strongly compete. In the former, energy may be dissipated through elastic nucleon-nucleon collisions, while in the latter the energy dissipation occurs through the interaction of individual nucleons with the nuclear mean field. Regardless of the dissipation process, the thermalization timescale is comparable to the interaction time which is defined as:

$$\tau_{inter} = \frac{R}{v_{rel}} \tag{1.5}$$

where R is of the order of the sum of the radii of the two interacting nuclei. Therefore, the following conclusions can be drawn:

- A considerable fraction of the available energy may be thermalized during the interaction between projectile and target. Very hot fragments can therefore be created in nucleus-nucleus collisions.
- However, a fraction of the available energy may not be thermalized during the collision leading to the so-called *pre-equilibrium emission*, a fast emission prior to thermalization.

As far as central collisions in this energy range are concerned, on average not all nucleons of the projectile get stuck inside the target during the interaction. In the early stage of the collision, some of them may escape and be emitted as light particles before the remnants of the two colliding nuclei fuse. The mass of the system which is formed is clearly smaller than the sum of the masses of the two colliding partners. Such a partial fusion is referred to as *incomplete*.

At low excitation energies a nucleus can be conceived as a liquid, whereas at higher energies it can be regarded as a gas. Therefore, the presence of an energy transition region can be expected. It is in this intermediate energy range (Fermi domain) that the *multifragmentation* process arises, i.e. the simultaneous emission of more than two ($N_{frag} > 2$) fragments by the excited nucleus. The evolution of the multifragmentation phenomenon is linked to the problem of liquid-gas type phase transitions in nuclear matter. It can be said that multifragmentation represents the intermediate mechanism between the decay process at low energy (evaporation) and that at high energy (vaporization).

1.1.3 Relativistic energy range

A brief description of reaction mechanisms occurring within the relativistic energy range is provided here for completeness. Only the relevant aspects are shortly summarized since the experimental study described in this thesis is focused on the fusion-evaporation reactions.

Heavy-ion collisions at energies between 200 MeV/u and 1 GeV/u feature a wavelength associated with nucleon-nucleon collisions shorter than the nucleon size. Thus, the main dissipation process in relativistic heavy-ion collisions is the hadronic cascades. Moreover, the relative velocity between projectile and target nucleons exceeds the Fermi velocity v_F. It follows that the so-called *participant-spectator picture* is adopted to describe the process. Basically, this states that nucleons which do not fall within the overlapping zone of the two colliding nuclei do not suffer hard nucleon-nucleon collisions and can be considered as the spectators of the interaction, whereas the other ones are the participants (Fig. 1.3). At the early stages of the study of the physics of partici-

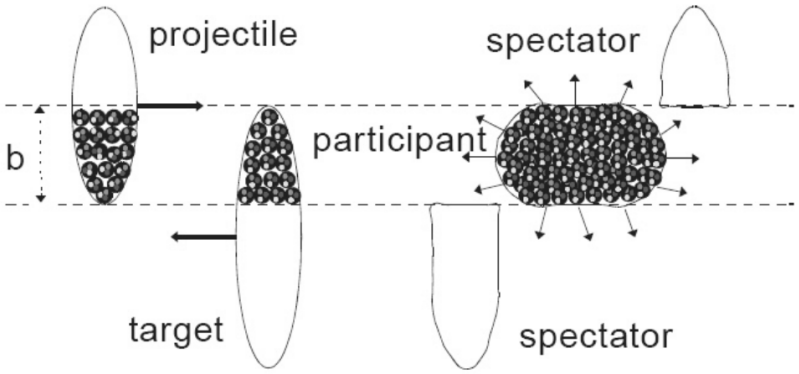

Figure 1.3: Situation before the relativistic heavy-ion collision on the left and subsequent creation of dense matter after the collision on the right.

pants/spectators the spectators were thought to be released almost cold upon separation from the participant zone. On the contrary, it turned out that hot spectators nuclei reaching excitation energies comparable to their binding energies can be observed. Being produced in semi-peripheral collisions, the corresponding nuclear matter results to be hot but uncompressed unlike central collisions at lower bombarding energy. Peripheral collisions therefore provide valuable information on the physics of hot nuclei, without disturbance by compression effects. As far as participants are concerned, nucleons which are mutually swept out from target and projectile form a kind of "fireball" which decays as an ideal gas [8]. With b decreasing and by considering central collisions, the excitation energies in question increase and a transition occurs from multifragmentation to vaporization of the system, i.e. a complete breakup of the nucleus into its components.

1.2 Elastic scattering

Almost everything we know about nuclear and atomic physics has been discovered by means of scattering experiments. The elastic scattering process is the simplest of all nuclear reactions. As mentioned in Sec.1.1, in this kind of process the nuclei at the entrance channel are not different from those at the exit channel. Therefore, basically, the incident particle undergoes a deviation in its trajectory due to the interaction with other particles and/or potentials, while the total kinetic energy and the momentum of the system are conserved. For instance, it was through an experiment on elastic scattering that in 1911 Rutherford discovered the existence of a nucleus inside the atom. He came to this conclusion observing that if a gold sheet is bombarded with α particles, most of them are undeflected whereas a small percentage bounced off the gold foil at very large angles (Fig. 1.4). This could be explained by assuming that the atom consists of a

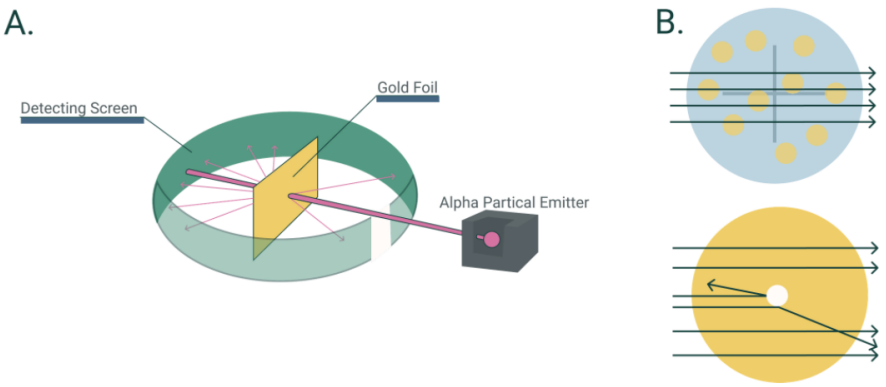

Figure 1.4: **A**. The experimental setup for Rutherford's gold foil experiment. A radioactive element emitting α particles is directed toward a thin sheet of gold foil surrounded by a screen which would allow the detection of the deflected particles. **B**. The plum-pudding atomic model (top) states that all of the α particles should pass through the gold foil with little or no deflection. Rutherford, instead, found that a small percentage of α particles are deflected at large angles, which could be explained by an atom with a very small, dense, positively-charged nucleus at its center (bottom).

tiny, dense, positively charged nucleus in which most of the atomic mass is concentrated around which the electrons orbit. The atomic model accepted at that time (Thomson's plum pudding) was then replaced by the Rutherford's planetary model.

Both classical and quantum mechanical approaches describe scattering phenomena in terms of cross section σ which in general represents the probability that a given process occurs. The elastic scattering between point-like particles occurring through a spherically

symmetrical potential can be described with a classical approach, for sake of simplicity. Under these assumptions, the collision is determined by the value assumed by the impact parameter b [9]: particles included in the annular region $(b,b+db)$ are scattered inside the angular region $(\theta, \theta - d\theta)$ which corresponds to a solid angle $d\Omega$. Fig. 1.5 shows that a greater impact parameter corresponds to a smaller diffusion angle. Let N_0 be the

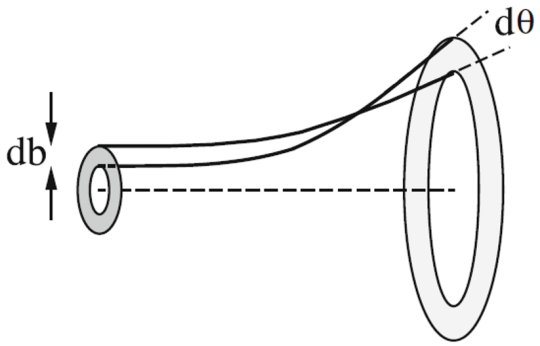

Figure 1.5: Elastic scattering of charged particles reaching the region of surface $2\pi bdb$ around a fixed massive diffusion center producing a Coulomb type potential. Normally the scattering centers are heavy nuclei. The incident particles are elastically scattered in the angular region $(\theta, \theta - d\theta)$ [9].

number of incident particles per unit of time and area. Then the number of incident particles scattered elastically per unit of time in the interval $(\theta, \theta - d\theta)$ is given by:

$$dN = 2\pi N_0 bdb = N_0 d\sigma \tag{1.6}$$

where $d\sigma = 2\pi bdb$ is the surface of the annular ring crossed by the incident particles scattered in the angular range $(\theta, \theta - d\theta)$. The *differential cross section* is defined as the quantity:

$$d\sigma(\theta) = \frac{d\sigma}{d\Omega} d\Omega = \frac{d\sigma}{d\Omega} 2\pi sin\theta d\theta = -2\pi bdb. \tag{1.7}$$

By considering $d\Omega = 2\pi sin\theta d\theta$ the elementary solid angle, we obtain:

$$\frac{d\sigma}{d\Omega}(\theta) = -\frac{b}{sin\theta}\frac{db}{d\theta}. \tag{1.8}$$

It should be noticed that the minus sign is needed if dN is considered as the difference between initial and final particles. Eq1.8 represents the differential cross section according to a classical approach and it is valid in general.

By considering the specific case of Coulomb elastic diffusion. The Coulomb potential due to a charge scattering center Ze is:

$$U(r) = \frac{Ze}{r}. \tag{1.9}$$

It can be shown [9] that from the conservation of energy and momentum the impact parameter is given by:

$$b = \frac{Zze^2}{2E_c} cot\frac{\theta}{2} \tag{1.10}$$

with z and E_c charge and kinetic energy of the incident particle, respectively. Knowing this and making a replacement in Eq.1.2 one gets the Rutherford's classical formula for elastic scattering between two spinless charged particles:

$$\frac{d\sigma}{d\Omega}(\theta) = -\frac{b}{sin\theta}\frac{db}{d\theta} = \frac{(Zze^2)^2}{(4E_c)^2}\frac{1}{sin^4(\theta/2)}. \tag{1.11}$$

In order to obtain the total cross section, it is necessary to integrate the differential cross section over the whole solid angle. So in general, we have:

$$\sigma = \int \frac{d\sigma}{d\Omega} = \int_0^{2\pi} d\phi \int_0^{\pi} sin\theta \frac{d\sigma}{d\Omega}. \tag{1.12}$$

The cross section has the dimension of an area and it is expressed in barn unit where $1b = 10^{-24} cm^2$. Still following the classical approach, the cross section can be thought as the area around a target particle within which the presence of a second particle generates two body interaction phenomena. In other words, the cross section can be interpreted as the effective surface area seen by the impinging particle.

The study of the Rutherford scattering has very important implications from an experimental point of view. Within this thesis work, for instance, elastic scattering processes are considered in order to perform the energy calibration of the detectors of the experimental apparatus (Chapter 3). Furthermore, the elastic scattering of ^{16}O onto a ^{197}Au target at 95 MeV has been studied in a commissioning experiment in order to test the recent electronic upgrade performed on the GARFIELD detector. A more detailed description of the commissioning analysis can be found in App. A. Fig. 1.6 illustrates the Rutherford scattering trend of the experimental points (black dots) from the commissioning experiment compared with the theoretical curve given by the formula 1.11 (red line).

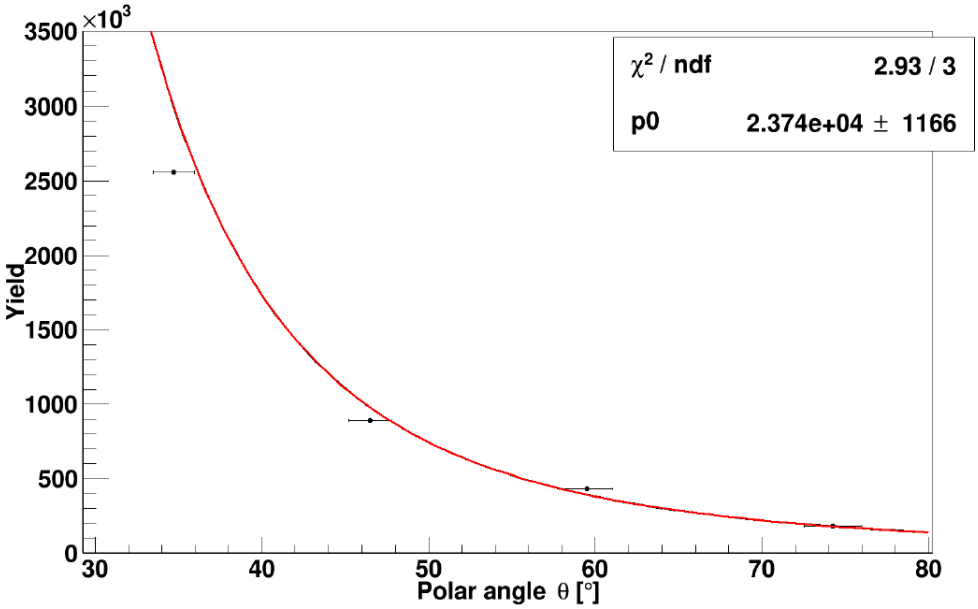

Figure 1.6: Experimental Rutherford elastic behaviour of the reaction ^{16}O+^{197}Au at 95 MeV (black dots) in the angular region $30° - 80°$ of the GARFIELD array. The experimental yields are normalized to the solid angle. The red line represents the one-parameter fit function applied.

1.3 Fusion-evaporation reactions

Fusion-evaporation mechanisms are an important tool for probing the possible deviations from a purely statistical decay of the compound nucleus that is formed during the reaction, thus highlighting non-statistical effects such as those due to clusterized structure. Within this thesis work, ^{18}O+^{12,13}C fusion-evaporation reactions at different bombarding energies are investigated.

In the mean field energy range and in case of central collisions ($b << b_{gr}$ and $b < b_{crit}$), the two nuclei undergo a sizable overlap during the collision. This results in a large amount of energy and angular momentum transfer from the relative motion to the internal degrees of freedom. This energy transfer is shared among many of the nucleons of the combined projectile + target system. Every single nucleon is subject to an average increase in energy which, however, is not enough to free it from the nucleus. As many other collisions between nucleons occur, there are both a statistical distribution in energies and a small probability for a single nucleon to gain a large enough share of the energy to escape for such bombarding energies. These reactions have a definite intermediate state called *compound nucleus* resulting from the complete fusion of the two colliding partners which occur after the absorption of the incident particle, but

before the emission of the outgoing particle/particles. Therefore CN's mass and charge are given by the sum of mass and charge of the two partners. This compound nucleus is a relatively long-lived intermediate state of particle-target composite system which lives several times longer than the time needed for the transition of the incident particle across the target (10^{-21} s). The time scale of compound nucleus reactions is of the order of 10^{-18} s – 10^{-16} s. As mentioned in Subsec. 1.3, the evolution of the system does not depend on the way the CN is formed. Once the equilibrium in the distribution of energy and angular momentum is established, the CN decays in two different ways according to the type of nucleus, its excitation energy and its spin. One possibility is the *fission* in which the compound is divided into two fragments because of the strong nuclear force and the Coulomb repulsion. The other possibility is through a process known as *evaporation* in which the CN loses its excitation energy by emitting light particles and gamma radiation. The resulting nuclear fragment is referred to as *evaporation residue* (ER). However, for higher impinging energy some clusters of nucleons or single nucleons can be emitted before the system reaches its full thermalization. This phenomenon is called pre-equilibrium emission. Due to this fast emission (with a time scale $\sim 10^{-22}$ s) the formed CN features a reduced mass and excitation energy.

1.3.1 Complete fusion

The term *complete fusion* describes a situation in which projectile and target merge forming a unique system which can reach a thermodynamical equilibrium[4]. Symbolically, this can be written as

$$(A_1, Z_1) + (A_2, Z_2) \rightarrow (A_1 + A_2, Z_1 + Z_2)_{E_{ex},j} \tag{1.13}$$

where the final state is completely characterized by its total mass, charge, energy and angular momentum. In terms of energy balance in the nuclear fusion, the excitation energy E_{ex} of the CN results in the following formula

$$E_{ex} = E_{CM} + Q_F = E_{CM} + c^2(M_1 + M_2 - M_{1+2}) \tag{1.14}$$

with E_{CM} corresponding to the center-of-mass bombarding energy, Q_F the gain in binding energy due to the formation of CN in its ground state and M_1, M_2 and M_{1+2} the ground-state masses of projectile, target and CN, respectively. With bombarding energies above the fusion barrier, CN excitation energy values around $40-50$ MeV for a wide range of projectile and compound nucleus masses ($A_1 \leq 80, A_1 + A_2 < 300$) are observed [10]. With these features, a "cold" CN with $E_{ex} < 40$ MeV cannot be formed. Therefore, this system will decay either by light-particle evaporation or by fission and the nature of the final products will depend on the respective probability of these processes.

[4]It can be noticed that this definition is identical to the classical concept of compound nucleus introduced by Niels Bohr.

A first estimation of the fusion cross section can be derived assuming that projectile and target can interact only in two ways: either by elastic scattering or by the absorption resulting in the formation of the CN. This situation can be described by introducing the effective potential

$$V_b(r) = V(r) + E\frac{b^2}{r^2} \tag{1.15}$$

where the first term stands for the Coulomb-plus-nuclear scattering potential and the second one for the centrifugal potential. Fig. 1.7 shows the values of the effective

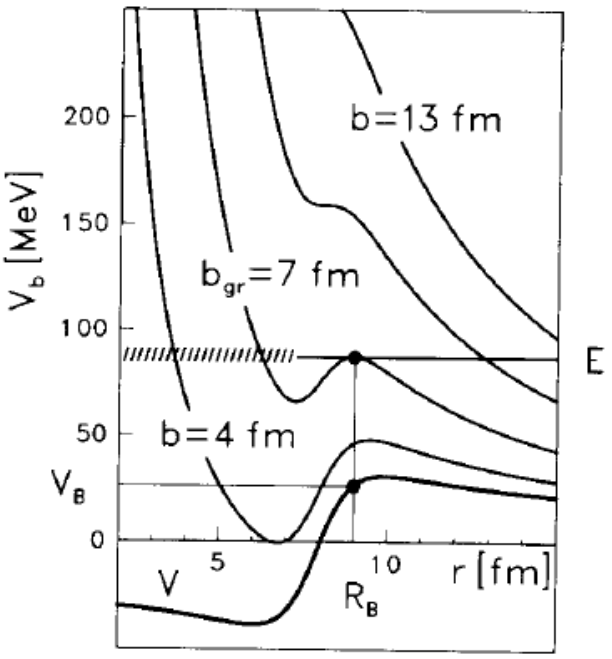

Figure 1.7: Scattering potential $V(r)$ and effective potential $V_b(r)$ for different values of the impact parameter b for the system ^{18}O+^{58}Ni. Notice that for $b = b_{gr}$ the height of the Coulomb barrier coincides with the energy E [11].

potential for various impact parameters b. It can be noticed that with the exception of very large b values, the effective potential features a barrier being repulsive on the outer flank and becoming attractive on the inner flank. In this simple picture, the *grazing impact parameter* b_{gr} is the impact parameter cut-off value which determines whether the projectile will be reflected by the barrier ($b > b_{gr}$) or overcome the barrier proceeding towards the interior fusing with the target ($b < b_{gr}$). This clear distinction given by b_{gr} obviously applies only in this approximation where the system either undergoes elastic scattering or fuses. If direct or deep-inelastic collisions start to become relevant, b_{gr}

separates the region of quasi-elastic from that of deep-inelastic processes. The *total fusion cross section* is expressed as [11]:

$$\sigma_F = \int_0^{b_{gr}} 2\pi b db = \pi b_{gr}^2. \tag{1.16}$$

One can explicit the energy dependence of the fusion cross section by inserting the value $b_{gr} = R_B\sqrt{1 - \frac{V_B}{E}}$ where R_B and V_B are the barrier radius and the corresponding value of the scattering potential shown in Fig. 1.7 thus obtaining:

$$\sigma_F(E) = \pi R_B^2\Big(1 - \frac{V_B}{E}\Big). \tag{1.17}$$

This result within the classical limit is adequate for the total fusion cross section at bombarding energies not too close to the fusion barrier. On the contrary, for higher bombarding energies high orbital angular momenta are involved. Therefore, a more detailed description is usually required and the total absorption cross section can be written in terms of l as:

$$\sigma_F(E) = \frac{\pi}{k^2}\sum_{l=0}^{\infty}(2l+1)T_l \tag{1.18}$$

where T_l represents the transmission coefficients which define the probability of the formation of a CN with energy and angular momentum depending on the impinging energy and angular momentum. In this derivation the sharp-cut-off approximation for T_l is adopted:

$$T_l = \begin{cases} 1 \text{ for } l < l_{gr} \\ 0 \text{ for } l > l_{gr}. \end{cases} \tag{1.19}$$

Finally, the general expression of the cross section for a transition from the entrance channel α via the corresponding CN to a specific exit channel β is:

$$\sigma_{\alpha\to\beta} = \sum_J \sigma_J(\alpha)\frac{\Gamma_J(\beta)}{\Gamma_J}. \tag{1.20}$$

Here $\sigma_J(\alpha)$ stands for the fusion cross section for channel α, $\Gamma_J(\beta)$ is the decay width of the CN into channel β and Γ_J is its total decay width at J angular momentum.

1.3.2 Compound nucleus decay

As previously discussed, the compound nucleus is an intermediate transitory system which follows the fusion of projectile and target. More in general, compound-nucleus reactions can be divided in two phases. In the first one fusion takes place whereas in the second one the compound nucleus decays by evaporation or fission. According to what

discussed in Sec. 1.3.1, the fusion cross section is equal to the *total* compound reaction cross section, i.e. the sum of the CN cross section over all the possible exit channels:

$$\sigma_F(\alpha) = \sum_{\beta} \sigma_{CN_{\alpha\to\beta}}. \tag{1.21}$$

In addition to the condition that projectile and target have to be in close contact, many degrees of freedom must be involved in the collision in order to get a compound nucleus. This is not the case if the colliding partners are both light nuclei. Depending on the incident energy, several narrow isolated resonances rise when a low-energy light projectile fuses with a heavy target. Furthermore, if both nuclei are heavy ions the CN system gains complexity and cannot be described as an individual state any longer, thus requiring an approach with statistical methods [10]. It was Wolfenstein, later followed by Hauser and Feshbach, who introduced the statistical formalism to derive the CN cross section. In short, this assumes that once the CN is formed, its decay is completely determined by the statistical weights of the various possible final states regardless of the nuclear structure. Over the years this approach has laid the foundations of current statistical decay models. To better understand in which states the system will preferentially decay, an excited nucleus characterized by mass A, excitation energy E^*, charge Z and angular momentum J is considered. The well-known Fermi golden rule:

$$\frac{\mathrm{d}N_{i\to f}}{\mathrm{d}t} \propto |M_{i\to f}|^2 \rho_f \tag{1.22}$$

provides the transition probability from an initial state i to a final state f [6]. According to the statistical model, all the transition matrices $M_{i\to f}$ are equal. This means that the probability of observing a given exit channel is solely governed by its density of states ρ_f. By applying this formula for the evaporation case where a parent nucleus i emits in the final state f a particle b with spin s and kinetic energy in the range $(\epsilon,\ \epsilon + d\epsilon)$, the corresponding emission probability per unit of time can be written as:

$$P_b(\epsilon) = C_0 \rho_f(E_f^*) dE_f^* (2s+1) \frac{4\pi p^2 dp V}{h^3}. \tag{1.23}$$

For simplicity, one can see this quantity as the product of three terms. C_0 is a normalization constant obtained from the *detailed principle* stating that microscopic phenomena are time reversal invariant. Thanks to this property the decay probability can be linked to the reverse fusion reaction rate P_F, i.e. the number of fusion per unit of time between particle b and final nucleus f leading to the initial nucleus i:

$$\frac{P_b(\epsilon) d\epsilon}{n_f} = \frac{P_F}{n_i}. \tag{1.24}$$

The second term is given by the product of the density of states $\rho_f(E_f^*)$ available for the daughter nucleus with excitation energy E_f^* and energy interval dE_f^*. What is left,

$(2s+1)4\pi p^2 dpV/h^3$, represents the number of states of the emitted particle with a linear momentum between p and $p+dp$. V can be thought as the volume in which the decay takes place. The number of available states n_i in Eq. 1.24 can be expressed as $n_i = \rho_i(E^*)dE^*$ while the fusion rate can be written as $P_F = v\sigma_F(\epsilon)/V$ with v being the particle velocity. By considering all these expressions, the final formula for the emission probability per unit of time is:

$$P_b(\epsilon)d\epsilon = \frac{\rho_f(E_f^*)}{\rho_i(E^*)}(2s+1)\frac{4\pi p^2}{h^3}\sigma_F(\epsilon)d\epsilon. \tag{1.25}$$

It is straightforward to notice that the evaporation de-excitation channel will be favoured with a large number of accessible states. This result emphasizes the fundamental role played by the density of states as previously discussed. As already mentioned, the capture cross section is expressed as in Eq. 1.18 and according to the approximation in Eq. 1.19 two cases might be distinguished:

$$\sigma_F(\epsilon) = \begin{cases} \pi R^2\left(1 - \frac{B_b^{Coul}}{\epsilon}\right) & \text{for } \epsilon \geq B_b^{Coul} \\ 0 & \text{for } \epsilon \leq B_b^{Coul} \end{cases} \tag{1.26}$$

B_b^{Coul} being the Coulomb barrier associated with the emission of particle b. The number of states available for a nucleus with an excitation energy between E^* and $E^* + \Delta E^*$, instead, features an exponential evolution of the kind:

$$\rho(E^*) \propto e^{E^*/T} \tag{1.27}$$

where T is the temperature and contains the dependence on the corresponding entropy S of the system:

$$\beta = \frac{1}{T} = \frac{dS}{dE^*} \approx \frac{\Delta ln\rho(E^*)}{\Delta E^*}. \tag{1.28}$$

By considering all these expressions and by replacing them in Eq. 1.25, $P_b(\epsilon)$ results to be:

$$P_b(\epsilon) = \frac{\epsilon - B_b^{Coul}}{T^2} e^{-(\epsilon - B_b^{Coul})/T} \quad \text{for } \epsilon \geq B_b^{Coul} \tag{1.29}$$

The energy E_f^* is expressed as a function of ϵ, namely $E_f^* = E_{fmax}^* - \epsilon$ and the exponential term comes from the relation in Eq.1.27. T is the temperature of the final nucleus and can be thought to be independent on ϵ only for significant excitations. In other words, for nuclei close to their ground state this formalism is not valid. It can be noticed that the emission $P_b(\epsilon)$ follows a Maxwellian distribution typical of the decay of an equilibrated nucleus. It is worthwhile to remark that the result in Eq. 1.29 has been obtained with no assumption on nuclear structure. The microcanonical description of isolated systems, the density of states, the entropy of the system and its temperature were the

only ingredients used in this derivation. By combining all these elements, the absolute value of the nuclear density of states could be calculated. All the considerations made for the evaporation de-excitation channel also apply to the whole decay chain of a CN which can be depicted as a sequence of single particle emissions up to the final state. In this case T stands for the mean temperature since every evaporated particle leaves the CN in a new state with an excitation energy lower than that of the parent nucleus. Fig. 1.8 shows an illustrative picture of a fusion reaction followed by an evaporation chain. The final Maxwellian spectrum is given by the sum of all the contributions due to

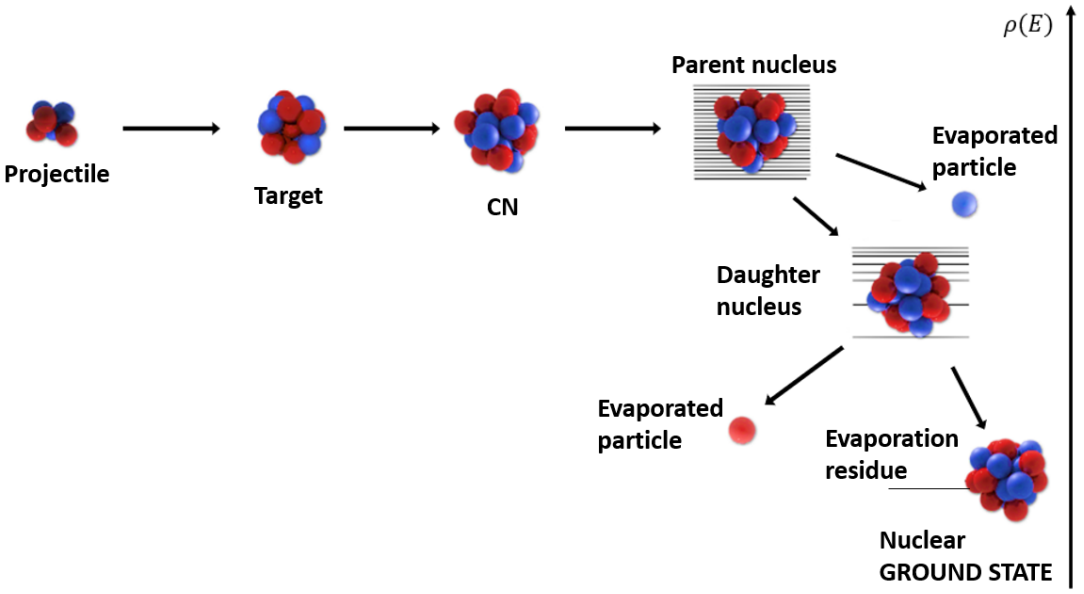

Figure 1.8: Diagram of a fusion-evaporation reaction and following compound nucleus decay. Notice that the decay chain of the CN starts when the nucleus is excited in its continuum whereas discrete states of the daughter nucleus are populated in the last step of the decay.

the single evaporation steps. The decay chain arrests when the daughter nucleus has an excitation energy below the particle emission threshold. At this stage, the evaporation residue de-excites by emitting γ-rays. The integration of Eq. 1.29 before normalization provides comparative information on how the different particles compete with each other in terms of emission probability. The total emission probability of a given particle b is essentially governed by the final density of states of the daughter nucleus:

$$P_b \propto \rho(E^* - Q_b - B_b^{Coul}). \tag{1.30}$$

This means that for similar Q values the emission of particles for which the Coulomb barrier is low is favoured. This explains why neutrons are highly favoured in the decay

of heavy nuclei [6]. The experimental evidences of the formation of a CN are manifold. For instance, because of the long time scale of the reaction and the "memory loss" of the compound nucleus about its mode of formation, the angular distribution of the products in the center-of-mass reference frame shows a symmetry about $\theta = 90°$ as shown in Fig. 1.9. Here θ is the emission angle of the reaction product with respect the beam

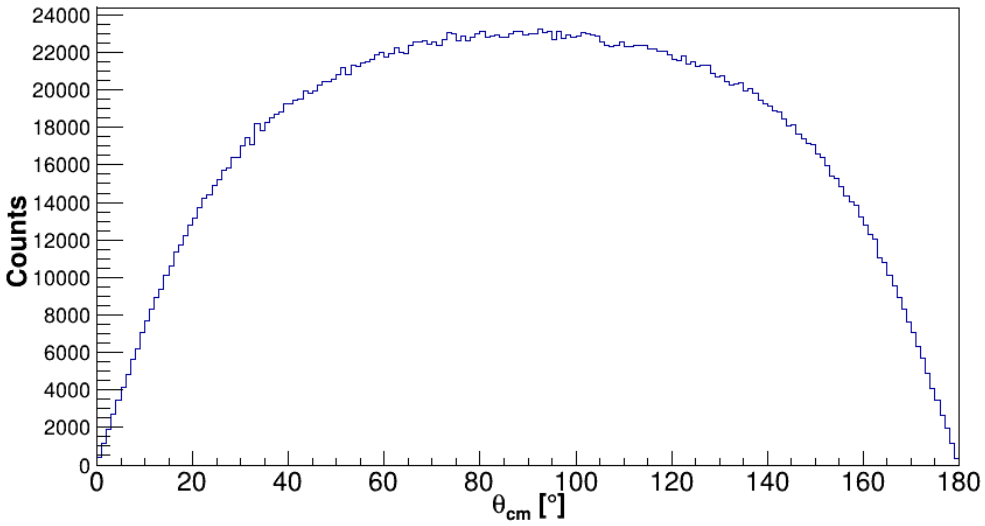

Figure 1.9: GEMINI simulation of angular distribution in center-of-mass reference frame of CN reaction products for the $^{18}O+^{nat}C$ at 122 MeV system.

direction. Another CN evidence comes from the energy spectra of the products. Thermal equilibration implies that particles emitted from the compound nucleus have a Maxwell-Boltzmann distribution, very much like vapour molecules escaping from a liquid. The characteristic form of a Maxwellian distribution is reported in Fig. 1.10.

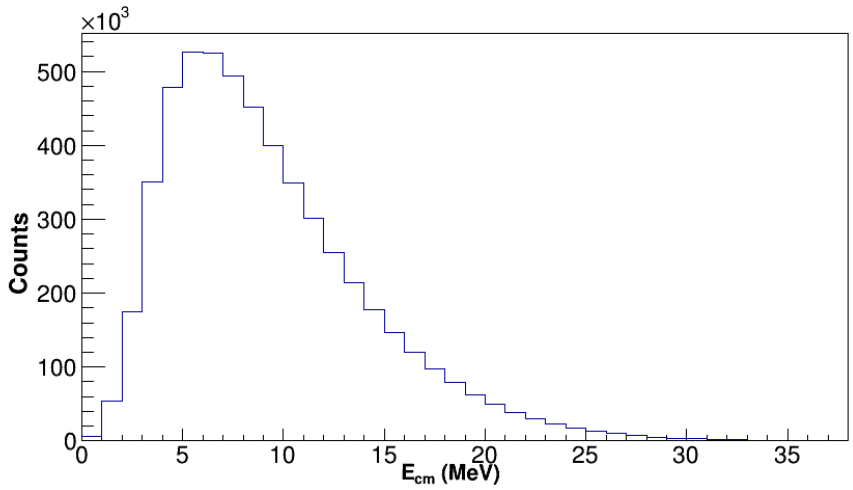

Figure 1.10: GEMINI simulation of α particle energy spectrum in center-of-mass reference frame for the ^{18}O+^{nat}C at 122 MeV system.

In Fig.1.11 the center of mass energy spectra of different particles normalized to the number of events for one of the studied reactions ($^{18}O+^{13}C$ at 112.5 MeV) are reported.

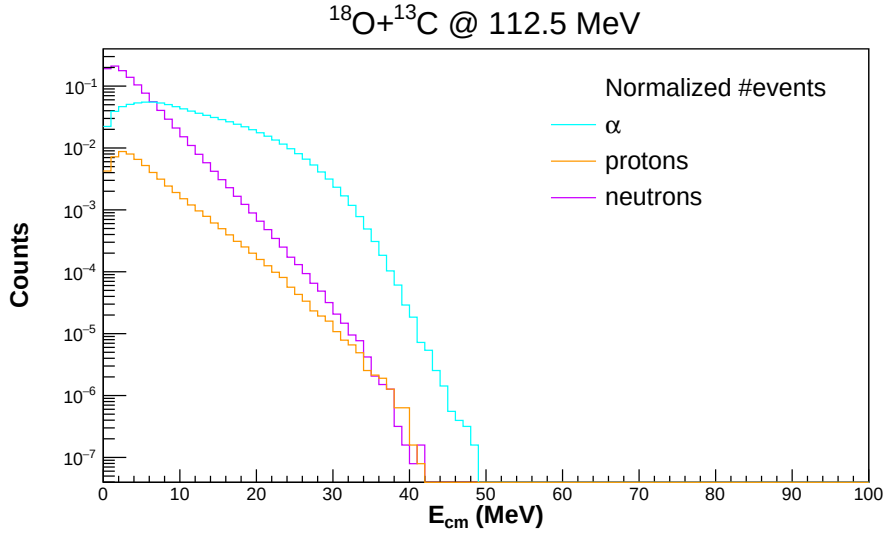

Figure 1.11: Comparison of center of mass energy spectra of different particles for the 18O+13Cat 112.5 MeV system: α-particles (cyan), protons (orange) and neutrons (purple). The distributions are normalized to the number of events.

Chapter 2

The experimental apparatus

The GARFIELD + Ring Counter (RCo), installed at Legnaro National Laboratories INFN, is a detection array for charged particles and fragments covering almost the whole solid angle [12]. This apparatus has been conceived in order to satisfy very demanding performances. In particular, the use of the ancillary RCo allows us to obtain good identification capability for fragment ($Z \geq 3$), high granularity at forward angles and an excellent isotopic separation of light charged particles ($Z \leq 2$) in all covered range. This setup enables a complete reconstruction of the events and a good characterization of the different competing reaction mechanisms.

The present chapter is aimed to describe the main features and working principles of the experimental apparatus. The GARFIELD detectors are presented in Sec. 2.1, while the Ring Counter detectors (ionization chamber, silicon strips and CsI(Tl) scintillators) in Sec. 2.2. The last part of this chapter is focused on the electronics (Sec. 2.3) and on the online data monitor (Sec. 2.4).

2.1 The GARFIELD apparatus

GARFIELD, acronym for *General ARray for Fragment Identification and for Emitted Light particles in Dissipative Collisions*, is a multi-purpose detector aimed to identify intermediate mass fragments and light charged particles. It consists of two large cylindrical shaped drift chambers, one backward C_1 and one forward C_2, filled with CF_4 gas at typical pressure of 50 mbar for the C_2 and 20-25 mbar for the C_1. The two chambers are placed back to back with respect to the target and with the axis in the same direction as the incident beam (Fig. 2.1).

The forward chamber covers the polar angular region from $29,5°$ to $82,5°$ in the laboratory framework, whereas the backward one from $97,5°$ to $150,4°$. Furthermore, the latter has a side gap of $\Delta\phi \simeq 45°$ which can be used for the placement of different ancillary detectors. The combination of these two chambers allows to cover almost the

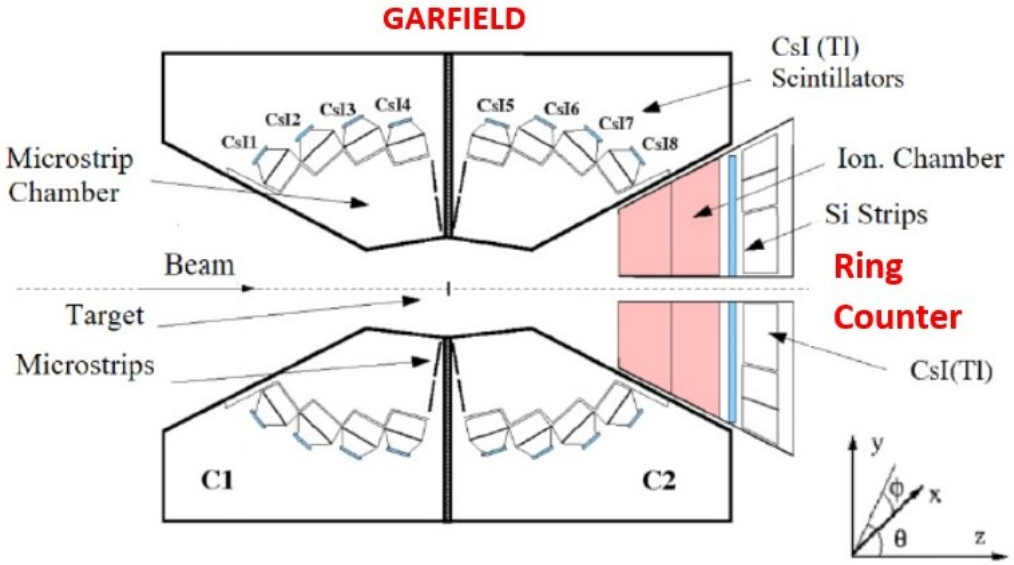

Figure 2.1: A sketch of the GARFIELD apparatus coupled with the RCo. The beam is sent from left to right against the target in the center, between the two chambers C1 and C2. In the bottom right-hand corner the frame of reference used to pinpoint the different detectors is shown.

whole solid angle between 30° and 150° with respect to the beam axis. The drift chambers C_1 and C_2 are mechanically divided into 21 and 24 azimuthal sectors respectively. Each sector contains four CsI(Tl) crystal scintillators and two microstrip gas chamber pads (MSGC) azimuthally divided in two sub pads. As shown in Fig. 2.2, the CsI(Tl) are arranged in a radial configuration with respect to the interaction point and constitute the boundaries of the sensitive gas volume. Thus, considering 4 CsI(Tl) and 4 MSGC pads per sector, there are 168 and 192 detection modules in C_1 and C_2, respectively.

MSGC and CsI(Tl) act as two stages of the detection system. The first provides information on the particle energy lost ΔE through ionization in the gas, while the latter on the residual energy E. The $\Delta E - E$ technique allows us to identify and accurately measure the energy of the reaction products.

In dealing with 4π apparatus, the possibility of two different particles hitting the same detector simultaneously cannot be neglected. This phenomenon is referred to as *double hit* and can be avoided requiring an high granularity of the detector. This can be achieved when a large number of detectors are used and this is the case of GARFIELD with its overall 360 detection modules. Each of them covers an angular range of about $\Delta\phi = 7.5°$ and $\Delta\theta = 14°$ if the chambers are used as ionization chambers. Moreover,

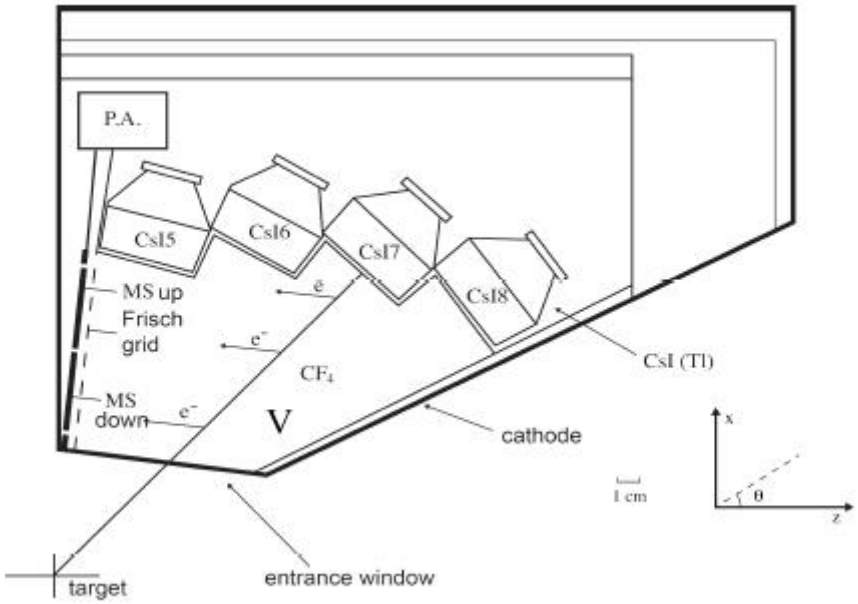

Figure 2.2: Scheme of a drift sector of GARFIELD.

using MSGC to measure the collection time of the produced ionization (*drift time*), an even more precise azimuthal resolution ($\sim 1°$) can be reached.

The whole system is contained in a 6 m long scattering chamber with a diameter of 3.2 m where a condition of high-vacuum ($10^{-5} \div 10^{-6}$ Pa) is created. This is achieved through several steps. This high-vacuum condition plays a fundamental role since it prevents energy dissipation of the beam in the residual gases inside the chamber.

The target is placed in the gap between the two GARFIELD chambers on a mechanical guide orthogonal to the beam. An automated system permits to change the target during the experiment avoiding the opening of the chamber and, consequently, the wasting time in emptying and filling processes. The target holder consists of 12 different positions. At the end of the beam-line three magnetic focusers are placed just before the entrance of the chamber. They are used to correctly collimate on the target the beam coming from the accelerator.

2.1.1 Drift chamber and MSGC microstrip detectors

The operating principle of ionization chambers relies on the ion-electron pairs production due to the passage of a charged particle through the gas. In the present case, the particles produced in the reaction enter the drift chamber through the $6 - \mu$m thick entrance window (0.78 mg/cm^2) and interact with the gas [13]. This interaction is governed by the Coulomb force and can lead either to excitation or ionization of the gas molecules. It

is in the latter that electron-ion pairs, which are the charge carriers, are created. These are also referred to as *primary ionization*. The mean number of pairs created depends on the ionization energy of the gas (minimum amount of energy required to remove the most loosely bound electron) and it is proportional to the energy lost ΔE by the fragment. Once created, it is important that these pairs remain in a free state long enough to be collected. For this reason their *recombination* must be hindered. This is possible thanks to the presence of an electric field generated by a drift cathode at around -1000 V, a Frisch grid at 60 V and a field cage. In general, under the electric field action, the ionized electrons are accelerated toward the anode, the ions toward the cathode. Therefore, the electric field in GARFIELD is shaped in order to force the ionization electron to drift towards the microstrip pads. Moreover, it has to be as homogeneous as possible in order to achieve a constant electron drift velocity and a straight trajectory. This allows us to deduce the flight path from the measurement of drift time knowing a reference time, i.e. the time the particle reaches the scintillator. Typical values of the electric field inside GARFIELD chambers are of the order of 10^4 V/m and the field is oriented in such a way that the electrons of the primary ionization are forced to drift toward the microstrip pads.

The MSGC operation takes advantage of the *avalanche effect* in the gas which consists in the amplification of the signals of the primary ionization electrons. A Frisch grid (Fig. 2.3) placed at 3 mm from the microstrip plane delimits a region in which the drift field

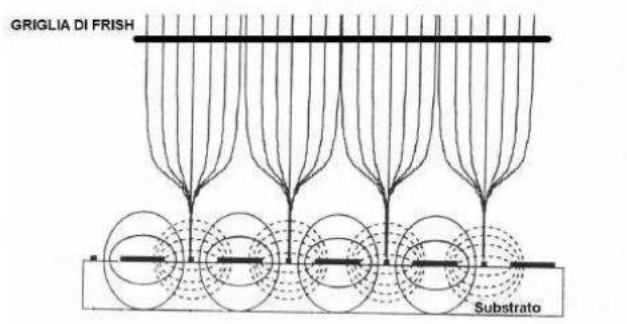

Figure 2.3: Drift lines of the electric field inside the gas drift chamber with microstrips as collecting anodes.

is radial (with a dependence of $\sim 1/r$ where r is the distance from the anode wire) and very intense, about 10^7 V/m. Under the action of such a strong field, electrons undergo a sudden acceleration near the microstrips starting thus the multiplication effect (avalanche effect). The final number of electrons is proportional to the number of the primary electrons and so to the energy of the particle ionizing the gas.

Each GARFIELD microstrip pad has a specially designed trapezoidal shape and it is equipped with alternated metal cathodic and anodic electrodes deposited through photo-

lithography technique on glass. Each pad is arranged almost perpendicularly (85° in θ) to the beam axis and is divided in four charge collection areas, conventionally named 1A, 1B, 2A and 2B (Fig. 2.4). Looking at the glass pads with the small base downward,

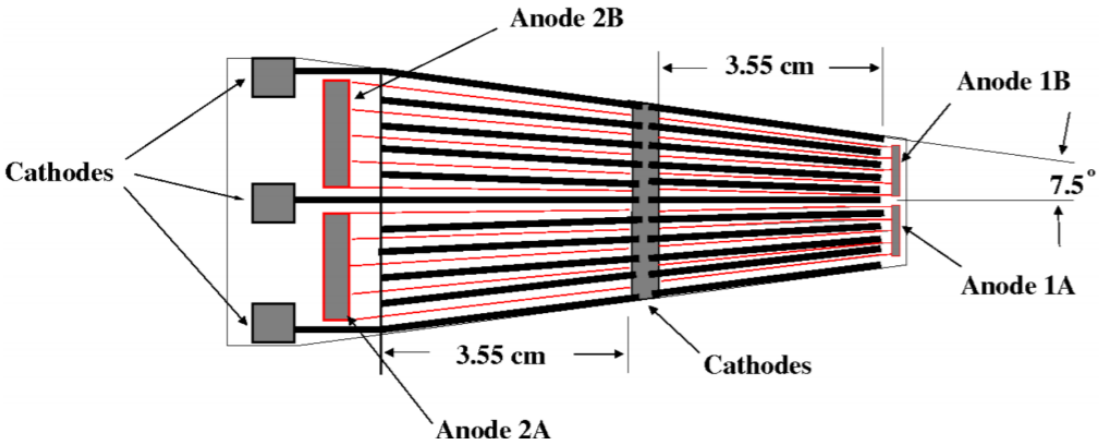

Figure 2.4: Scheme of a MSGC of the GARFIELD apparatus.

the numbers 1 and 2 refer to the nearest and furthest halves from the beam, while the letters A and B respectively stand for the left and right sides (Fig. 2.5). The anodes

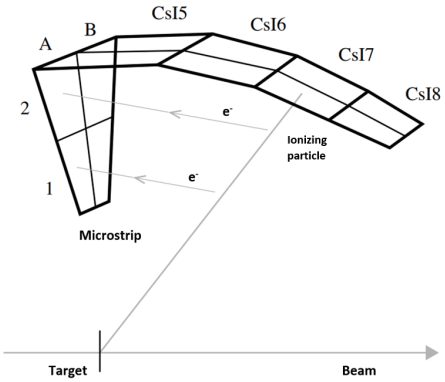

Figure 2.5: 3D sketch of the GARFIELD drift chamber cell. The naming convention used is shown.

are electrically connected to the four collecting areas and biased at 430 V, whereas the cathodes are all grounded [12]. The division of each pad in four areas provides four independent signal collection modules, hence ΔE values to be used, together with the scintillators, for $\Delta E - E$ correlations. Specifically, the longitudinal division in sections guarantees a higher precision on the azimuth angle.

The CF_4 gas is used to fill the chambers [12]. Thanks to its high density (0.19 mg/cm^3 at 50 mbar pressure and at a temperature of 20°) and high electrons drift velocity (10 cm/μs at 1 V/cm/mbar) the working pressure can be relatively low (50 $\div$ 200 mbar). This enables the use of a thinner entrance window being subject to lower pressures and lower voltage of the field cage, thus reducing the damage caused by possible discharges. An automatic recirculating and filtering system makes the gas continuously flow in the chamber in order to minimize oxygen contamination.

One of the main advantages of using microstrips as gas detectors is that, even with a gas at 50 mbar, gain factors of $30 - 50$ are achieved making the detection of very low energy (few MeV/u) particles possible. Hence, the request of a low energy threshold is satisfied. High counting rates and high gains can be achieve thanks to MSGC wide dynamic identification range and high signal-to-noise ratio for low ionization ions. Finally, being installed in drift chambers, MSGC enables the measurement of the particle track.

2.1.2 CsI(Tl) crystals scintillators

Scintillators make use of the fact that certain materials (*scintillating materials*), when traversed by radiation, emit a small flash of light, referred to as *scintillation*.

The scintillation process in inorganic crystals is related to their electronic band structure (Fig. 2.6). When a charged particle enters the scintillating material, it can either

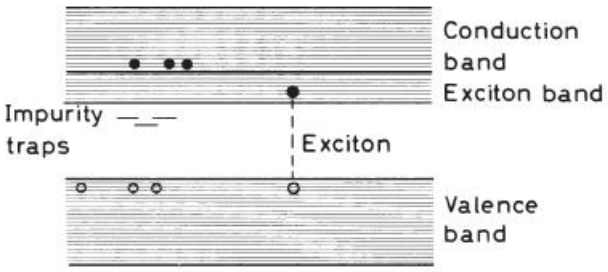

Figure 2.6: Scheme of the scintillation process in an inorganic scintillator, such as CsI(Tl) crystals.

ionize or excite one of the atoms of the crystal. In the former case, electrons of the valence band acquire enough energy to pass in the conduction band creating electron-hole pairs. In the latter, electrons are excited to the exciton band, located just below the conduction band, thus creating *excitons*, states in which the electron is electrostatically bound to the hole. Once a free hole or an exciton-hole has ionized an impurity center, if an electron falls into the opening left by one of them, a transition from an excited state to the ground state occurs with the emission of radiation [13]. The time evolution of the scintillation emission is normally given as the sum of two exponential terms with different decay times: a short one ($\tau_s \sim 0.75\ \mu s$) and a long one ($\tau_l \sim 5\ \mu s$) also referred

to as *fast* and *slow* components. As a consequence, the current pulse produced by the scintillation light in the photodiode can be described as:

$$i_l(t) = \frac{dQ_L(t)}{dt} = \frac{Q_s}{\tau_s} e^{\frac{-t}{\tau_s}} + \frac{Q_l}{\tau_l} e^{\frac{-t}{\tau_l}} \tag{2.1}$$

where Q_s and Q_l are the charges respectively produced by the short and long components of scintillation and $Q_L(t)$ is the total collected charge at time t which is given by:

$$Q_L = \int_0^\infty \frac{dQ_L(t)}{dt} dt = Q_s + Q_l. \tag{2.2}$$

Since fast and slow components depend on the kind of the incident particle (mass, energy and charge), it is possible to identify the ions by means of an analysis of the impulse form, a technique better known as *pulse shape analysis* (PSA). Examples of this technique can be found in Chapter 3.

Crystal scintillators are usually doped in order to improve their light emission efficiency, to reduce the self-absorption of the emitted scintillation and to get the desired wavelength of the output light for an optimal matching with the absorption spectra of the photodiode (Fig. 2.7).

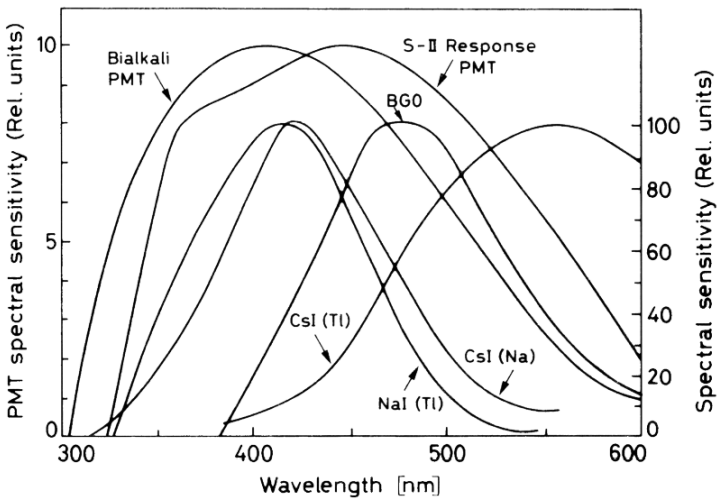

Figure 2.7: Emission spectra of different scintillators and absorption spectra of photodiodes. For a proper functioning, the emission spectra of the scintillator have to overlap the emission spectra of the photodiode as much as possible.

Each GARFIELD sector features four CsI(Tl) scintillators whose shape has been designed in order to optimize the geometrical efficiency. According to the GARFIELD partition in sectors mentioned above, there are 96 crystals in the forward chamber and

84 in the backward, each of which covers $\Delta\phi = 15°$ and $\Delta\theta \simeq 15°$. The crystals have a variable thickness of about $3 - 4$ cm in order to stop the charged products expected in the energy range of interest, and a different shape, as shown in Fig. 2.8, according to the different θ angles they are positioned in. The CsI(Tl) crystals act as the last stage

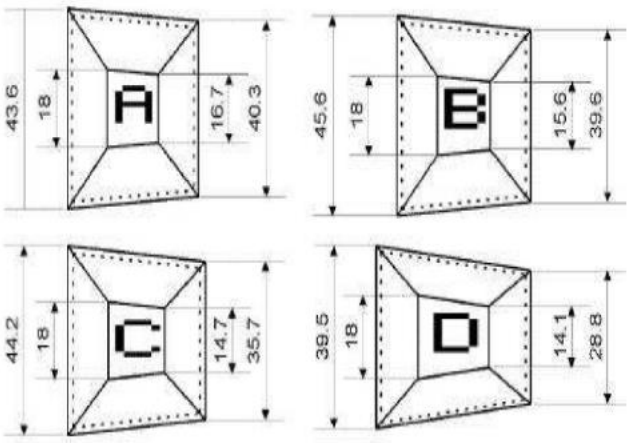

Figure 2.8: Different shapes of CsI(Tl) crystals. Letter A refers to the crystal nearest to the MSGC plane (θ bigger).

of detection of the reaction products passing through the gas volume by measuring their residual energy. Together with the MSGC they allow a $\Delta E - E$ correlation. In this case, a thallium (Tl) doping of about 1200 ppm is used. The energy resolution of CsI(Tl) is about 3 % for 5 MeV α particles and $2 - 3\%$ for 8 MeV/u Li and C elastically scattered beams on Au target [12]. Ranges of different particles in CsI(Tl) are shown in Fig. 2.9.

Crystals are optically coupled to Hamamatsu S3204-05 photodiodes closely connected to the pre-amplifiers. In order to avoid possible loss of the produced light and to shield them from the external light, the crystals are wrapped in a white diffusive paper and covered by a layer of aluminated *mylar*. Photodiodes are preferred to photomultiplier tubes for the following characteristics: greater stability, lower power dissipation, smaller size and bias voltage ($\sim$ 100 V) enabling operation at very low pressure.

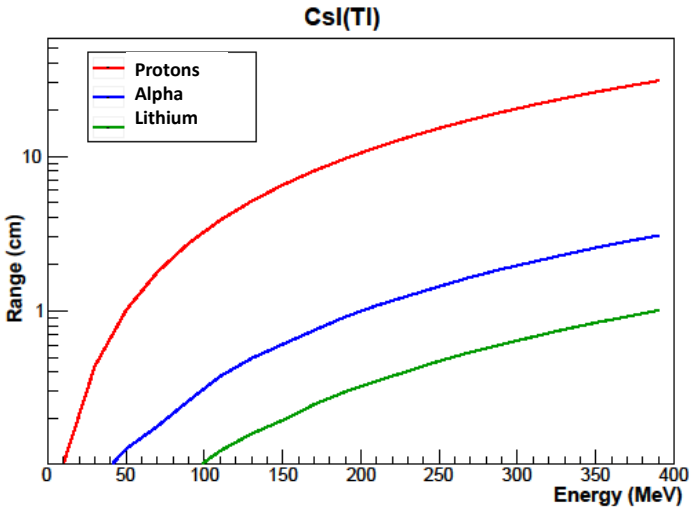

Figure 2.9: Range of protons (red line), α-particle (blue line) and lithium (green line) as a function of the incident energy in CsI(Tl).

2.2 Ring Counter

The Ring Counter (RCo) is a three-stage annular detector array with a truncated cone shape covering the polar angle range $5° < \theta < 17.0°$. As shown in Fig. 2.1, it is located at the exit of the forward chamber and it is conceived to be centered at 0° with respect to the beam axis. RCo can identify the particles through PSA and $\Delta E - E$ telescope techniques. It features a cylindrical symmetry along the beam axis and it is partitioned into 8 azimuthal sectors each of which covers an angle $\Delta\phi = 45°$ (Fig. 2.10). The first

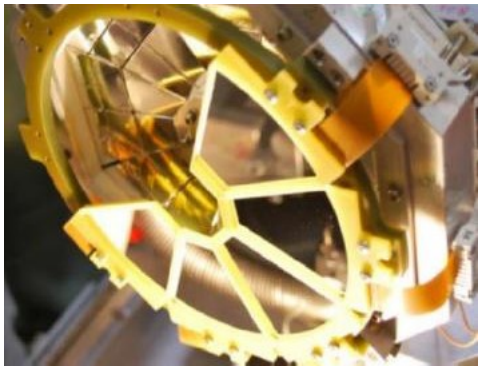

Figure 2.10: Ring Counter. The division in 8 azimuthal sectors can be seen.

stage is an ionization chamber (IC), followed by a strip silicon detector (Si). The last

stage is formed by CsI(Tl) scintillators. Specifically, each of the 8 sectors consists of one IC, one silicon *pad* segmented in eight *strips* and six 4.5−cm thick CsI(Tl) crystals [12]. So, overall, there are 48 Cesium Iodide crystals, each one covering half sector in the azimuthal coordinate (Fig. 2.11).

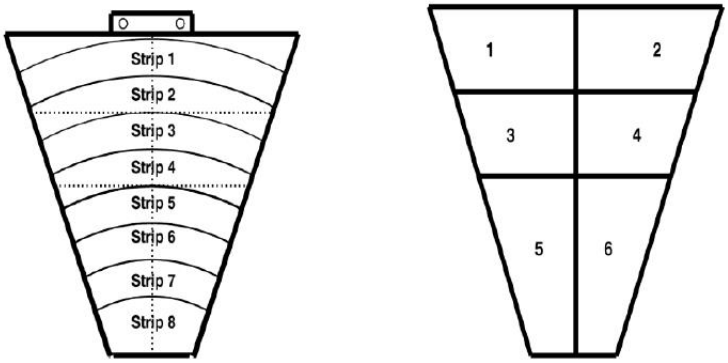

Figure 2.11: The RCo Si strips (left) and the superimposition (right) with the corresponding Cesium crystals. Note that at least two silicon strips correspond to each crystal.

Due to the partition in sectors mentioned above, the azimuth angle of particles reaching the scintillators is known with an accuracy of 22.5°.

Different screens can be positioned in front of the RCo via a remotely controlled collimator system. These screens are used for focusing, shielding or collimating purposes and can be moved under vacuum while running the experiment. The RCo is mounted on a sliding aluminum support and can be remotely moved back and forth in order to replace the front collimator.

2.2.1 Ionization chamber (IC)

Since an optimized geometric efficiency and minimum active losses of the area are desired, the drift chamber is designed in such a way that its *dead zone* coincides with the one of the silicon detector of the second stage. It is 6 cm long and contains three $1.5 - \mu$m thick electrodes of aluminized mylar: an intermediate anode and two grounded cathodes placed at the entrance and exit of the chamber. The cathodes are azimuthally segmented into eight parts following the 8-sector partition of the RCo. As opposed to GARFIELD chambers, the IC of the RCo does not contain any Frisch grids and the drift field has an axial direction. This configuration allows us to obtain the same reduced electric field by applying half the voltage that would be needed in absence of the intermediate anode. Furthermore, in order to minimize discharges to surrounding materials, the anode is completely contained in the gas volume and the others are grounded. The ionization chamber of the RCo is filled with the same gas as GARFIELD's drift chambers: CF_4.

The gas is continuously cleaned as it flows inside the chamber while maintaining the pressure constant through a remote control valve; before entering the chamber, the gas is filtered in order to remove residual oxygen and water vapour.

2.2.2 The silicon detectors

It has been demonstrated that better Z and A identification properties are achievable by exploiting silicon detectors with good resistivity uniformity [14]. As a consequence, the RCo is equipped with silicon detectors made using nTD (*neutron Trasmutation Doped*) silicon type, characterized by a better doping uniformity compared to the silicon normally used. This property reduces the dependence of the induced signal shape on the incidence point. Silicon detectors are used in rear-injection mode [17] in order to enhance the pulse shape discrimination capability by forcing the particle through the low field side [15, 17]. As mentioned above, each sector in which the RCo is divided contains a 300 μm thick silicon pad segmented into 8 strip covering a solid angle of $2-6$ msr. Moreover, a *guard ring* completes each pad; it is mounted all around the strips and properly biased in order to minimize the field distortion effects in the inter-strip region (220 μm wide). Inactive parts such as supports and spaces between the strips, containing the guard rings, reduce the active area to 90% of total one. This design makes the charge carriers splitting and *cross-talk* (i.e. the signal coming from contiguous strips) almost negligible. As far as the technical characteristics of the detectors are concerned, the bulk resistivity is of the order of 3400 Ω·cm and the full depletion voltage is 100 V with a recommended bias of 120 V. Each strip has a reverse current of about 30 nA. Thanks to the small thickness window of the silicon detectors (50 nm junction side, 350 nm ohmic side) a low threshold is obtained even in the reverse mounting configuration. Typical values of energy threshold for particles punching through the detectors are 6 MeV/u for protons and α-particles and $7-11$ MeV/u for light fragments.

2.2.3 CsI(Tl) scintillators

The third and last detection stage of each sector of the RCo consists of 6 CsI(Tl) $45-$mm thick crystal scintillators. These crystals are similar to those in GARFIELD but they have a different percentage of thallium doping, in the range of $1500-2000$ ppm, so as to enhance their light output and consequently an overall $2-3\%$ energy resolution can be reached when detecting 5.5 MeV α particles emitted by ^{241}Am source. Their smaller dimensions enable a better doping and a better scintillation response and collection efficiency of the single detector. All 48 scintillators are optically coupled with Hamamatsu S2744-08 photodiodes with an active area of 10×20 mm^2. As shown in Fig. 2.11, the polar angular region corresponding to the 4 Si inner strips is azimuthally covered by 2 of these scintillators, each with $\Delta\phi = 22.5°$. On the other hand, the region of the 4

outer strips is covered by 4 crystals, each covering half of the polar and azimuthal range defined by the strips. The pre-amplifiers are the same as those used in GARFIELD.

2.2.4 Monitor detector

At a much smaller angle ($\sim 1°$), inside the scattering chamber, a plastic scintillator is positioned aimed at counting elastic scattering events by Coulomb potential. These events are also referred to as *Rutherford collisions* and their cross section strongly depends on the angle and it is given by:

$$\sigma_{Ruth} \propto \frac{1}{sin^4(\frac{\theta}{2})} \tag{2.3}$$

For this reason, the exact location of the plastic detector inside the chamber is of great importance. The counting of these events is used to normalize the measurements of the other detector. This means that, once the Rutherford cross section at a given angle θ is known, an absolute cross section can be obtained.

2.3 Electronics

The signals coming from the detectors of the GARFIELD + RCo apparatus are collected by means of the pre-ampliefiers with different gains, and are reprocessed and stored through digital electronics. Every time a particle deposits energy in the active volume of a detector, a current pulse is produced in the reading circuit. The charge associated with this pulse is proportional to the incident energy and it is obtained by integrating the pulse into the *charge pre-amplifier*. The resulting output signal is then processed by an appropriate electronic chain. In order to minimize the noise contribution, the pre-amplifiers are mounted inside the scattering chamber. They are cooled with water cooling system which allows to dissipate the heat generated by the pre-amplifiers themselves. In the case of RCo, they are mounted on the same sliding plate of RCo in metallic boxes, which shield them from external fields; the pre-amplifiers are thermally connected to the boxes cooled by a water cooling system ($T_{H_2O} \sim 12^o$C). On the other hand, in case of GARFIELD, the pre-amplifiers are placed inside the gas volume very close to each detector; a water cooling system to keep the temperature under control has been provided around the GARFIELD chambers.

Originally, a *Fast- Sampling Analog-to-Digital Converter* (ADC) digitizes the signals of the whole RCo and CsI(Tl) crystals of GARFIELD. Currently, the pre-amplifiers output from all the detectors of the apparatus are analyzed by a programmable *Digital Signal Processor* (DSP) which performs advanced online data reduction [16]. This online selection via filtering and shaping algorithms reduces the amount of acquired data. In fact, relevant physical quantities, such as amplitude, current and rise time of the charge

signal, can be derived by exploiting the DSP. Nevertheless, in order to check the behaviour of the card every 1000 events a complete waveform is sent to the acquisition by the DSP for further off-line checks and debugging analysis. The extracted information, expressed in numerical form and stored into files, is ready for the analysis. An internal FIFO (*First In First Out*) storage memory, which operates at $125 \cdot 10^6$ samples/s, continuously records the ADC output values [17]. Basically, it is a sort of circular *buffer* since its first locations are continuously rewritten while a trigger signal arrives determining the beginning of the data recording process. On the other hand, analog electronics is used to process the MSGC signals of the drift chambers by means of a charge amplifier and a *peak sensing* ADC. The following figure (Fig. 2.12) illustrates the diagram of an acquisition channel where the input stage of the analog signal, the digitization section (ADC), the FIFO memory, the trigger section and the DSP are shown.

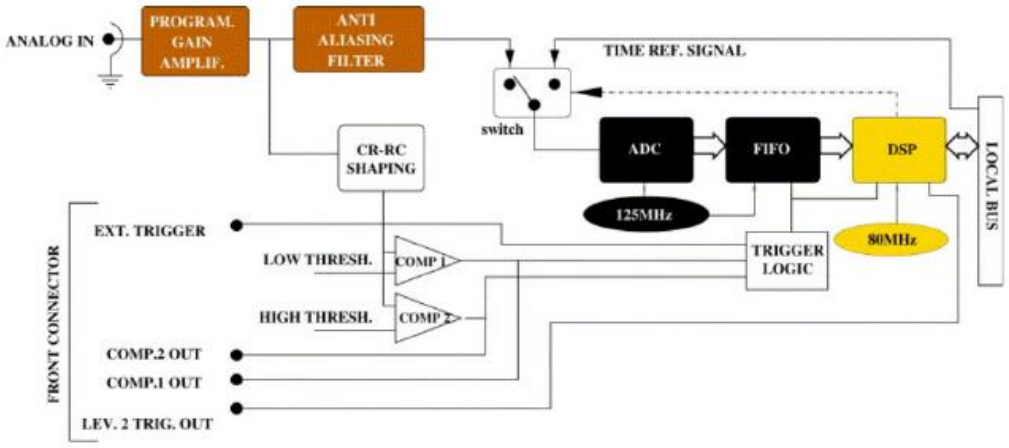

Figure 2.12: Block diagram of a digital acquisition channel.

2.3.1 Pulser

In order to verify the stability of the electronic chain, pulser runs were acquired ocasionally. A pulser is a signal generator that produces pulses at different voltages, but similar in shape to that coming from the detectors on the pre-amplifiers. The acquisition of this type of run provides a test of the stability and linearity of gain which may be sensitive to environmental conditions such as temperature variations.

2.3.2 Trigger system

The term *trigger* refers to a system that uses criteria to rapidly select particle interactions of potential interest for physics analysis. In other words, it is a logical signal produced when an event of interest occurs in the detector. Therefore, the choice of the particular trigger logic to be used is crucial for each experiment since it is closely related to the reaction mechanisms to be studied. In this way, particular physical conditions are imposed using logical combinations of trigger signals.

These selections can be performed by using two different kinds of triggers: *local triggers* and *validation signals*. The former are generated from a detector signal that has exceeded its acquisition threshold by means of a *Constant Fraction Discrimination* (CFD). Examples of local triggers are the ones generated by GARFIELD CsI(Tl) crystals or by the RCo silicon detectors. A validation signal, instead, is generated by a *trigger box* (Fig. 2.13), a VME card (CAEN V1495) programmed to perform coincidence and trigger task by means of a *Field Programmable logic array* (FPGA). The various local

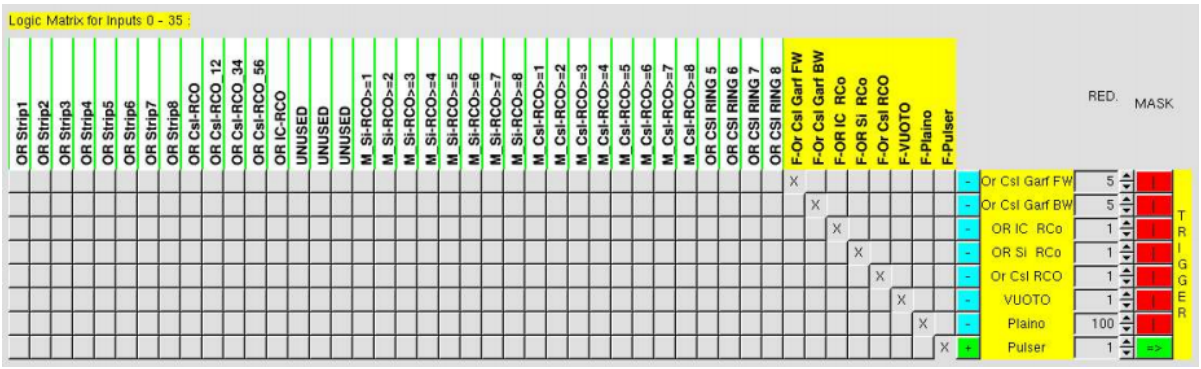

Figure 2.13: Logic array of the trigger box reported for illustrative purposes only. The trigger shown are different from those used during the experiment studied in this thesis.

triggers are collected in the trigger box which produces a validation signal that starts the acquisition and the gathering of the signals of all the hit detectors. A reduction factor "X" is associated to each trigger determining the number of occurrences X after which the acquisition starts. Tab. 2.1 reports the standard triggers used in GARFIELD

N°	Trigger	Reduction	Description
0	OR CsI GARF FWD	5	OR of the GARFIELD forward chamber scintillators
1	OR CsI GARF BWD	5	OR of the GARFIELD backward chamber scintillators
2	OR IC RCo	1	OR of the different parts of IC
3	OR Si RCo	1	OR among the RCo strips
4	OR CsI RCo	1	OR among the RCo CsI(Tl)
5	Plastic Monitor	100	Plastic Scintillators
6	Pulser	1	Pulse Generator

Table 2.1: Trigger logics used during the experiment with their settable reduction factors.

experiments. The OR of the GARFIELD CsI (N° 1 and N°2) triggers are used to have a 4π coverage. The OR of the RCo IC is enabled in presence of heavy fragments which is not the case studied in this thesis. On the other hand, the OR of CsI RCo and the OR of Si RCo are activated when studying reactions with higher cross section at forward angles. Trigger 5 refers to plastic scintillators placed at forward angles to evaluate elastic Rutherford scattering events in order to normalize counts to the absolute cross sections. Finally, trigger 6 is a pulser trigger aimed to control the stability of the whole electronic chain. This is particularly useful when summing data from several measurement runs.

2.4 GARFIELD monitor

The acquired data and the operation of the detectors are online monitored by means of a graphical interface program, named *GARFIELD Monitor*. It is a ROOT-based software that allows us to visualize several predefined 1D and 2D histograms, filled either with raw experimental data or with preprocessed variables. As an example, in Fig. 2.14, the counting rates in each detector of the apparatus are presented.

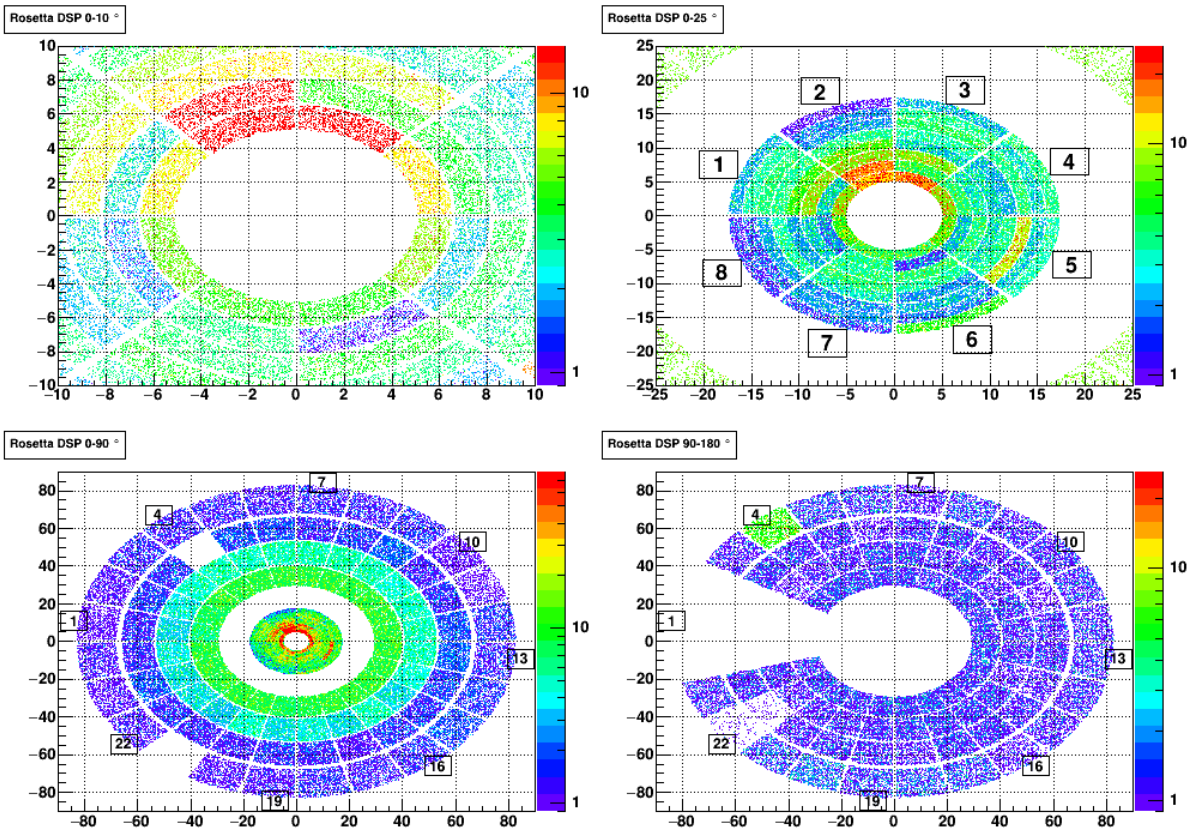

Figure 2.14: Graphical representation of counting rate in each detector of GARFIELD+RCo array: X=$\theta_{lab} \cdot sin(\phi_{lab})$ and Y=$\theta_{lab} \cdot cos(\phi_{lab})$. In upper panels the hit on RCo are shown for $\theta = 0° - 10°$ (left panel) and for $\theta = 0° - 25°$ (right panel). In the lower panels, countings of the forward chamber of GARFIELD and RCo ($\theta = 0° - 90°$) on the left and countings of the backward chamber of GARFIELD ($\theta = 0° - 90°$) on the right. The three missing sectors in the backward chamber are clearly visible.

On X and Y axis the combination of the polar and azimuthal angles

$$\begin{aligned} X &= \theta_{lab} \cdot sin(\phi_{lab}) \\ Y &= \theta_{lab} \cdot cos(\phi_{lab}) \end{aligned} \tag{2.4}$$

covered by each detector are represented in order to easily visualize the complete array. The resulting distribution is called "rosetta". The four panels in the figure refer to different polar angular coverage: the upper left panel shows a zoom of the inner silicon strip of the RCo; the upper right panel reports the whole RCo angular region; the lower panels illustrate the GARFIELD forward (plus RCo in left panel) and backward (right panel) angular coverage.

Chapter 3

The ISOLIGHT experiment: energy calibration and particle identification

This chapter is aimed at describing the ISOLIGHT experiment carried out by the NUCL-EX collaboration. After a brief description of the Tandem-PIAVE-ALPI acceleration complex in Sec. 3.1, the physical motivations that laid the foundation of this experimental campaign are reported in Sec. 3.2. The whole experimental conditions (covered angles and triggers) under which the experiment was performed are analyzed in Sec. 3.2.1. The energy calibration procedure of the Si strips and IC detectors of the RCo is discussed in detail in Sec. 3.4, while a general description is provided for the CsI(Tl) crystals. A final section (Sec. 3.5.3) is dedicated to an exhaustive description of the procedure adopted in order to identify the reaction products in mass and charge.

3.1 The Tandem-PIAVE-ALPI accelerator complex

At Legnaro National Laboratories heavy ion beams are provided by the accelerator complex Tandem-ALPI-PIAVE [18]. It consists of the Van de Graaf XTU Tandem accelerator, a superconducting linear accelerator ALPI and a positive ions injector PIAVE. In general, the electrostatic accelerator is based on two acceleration stages. Firstly, ions are generated by an external source and extracted with a positive charge state; secondly the charge state is transformed from positive to negative by crossing a charge-exchange region filled with gas. Indeed by playing on the relative electron affinity, ions feature an high probability of capturing electrons from the gas. At this stage, the negative ions enter the low energy side of the tandem and are accelerated towards a high voltage terminal (HVT) in the centre of the accelerator. On arriving at the HVT, the ions go through an electron stripper (a carbon foil) to be positively charged by losing many electrons.

The repulsive electrostatic field then further accelerates the ions in the second half of the accelerator. At the end, the outgoing particles are driven towards the measurement apparatus by means of magnetic deflectors and lenses. Fig. 3.1 shows the operational sketch a two stages electrostatic accelerator.

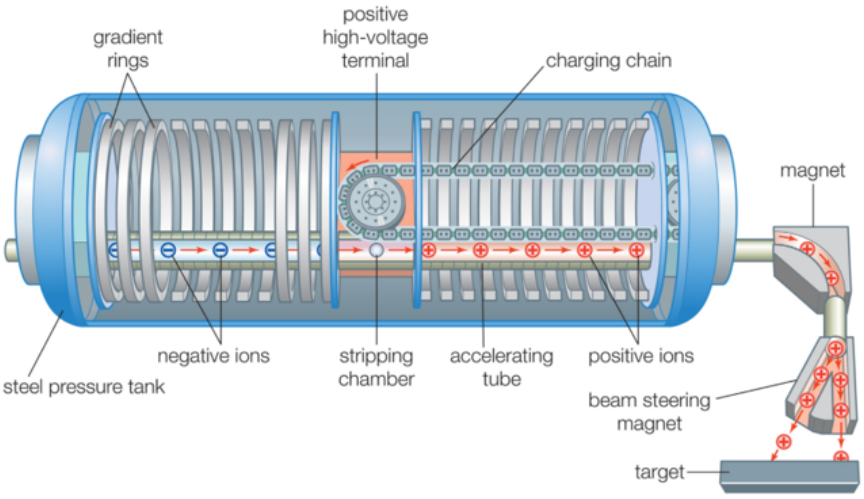

Figure 3.1: Operational sketch of a two-stage tandem accelerator [19].

The XTU Tandem accelerator at LNL consists of a horizontal tank filled with SF_6 insulating at 7 atm and it is routinely operated at terminal high voltages of up to 15 MV. The accelerator is able to accelerate ions from protons to ^{197}Au and can be operated with both continuous and pulsed beams. The pulsing system is based on 5 MHz choppers and bunchers and the time width of beam pulses is of the order of 1 ns. The XTU Tandem accelerator can operate in a standalone mode or as a positive ion injector for the ALPI superconducting linac. In Italian ALPI stands for "Acceleratore Lineare Per Ioni". It is a linear accelerator based on superconducting Quarter-Wave Resonator (QWR) cavities (Fig. 3.2) operated at liquid He temperature.

These cavities are displaced according to a U shape. The acceleration of high current ion beams with $A > 100$ cannot be sustained by the Tandem accelerator due to the high consumption of the carbon stripper foils. For this reason, the additional positive ions injector PIAVE was installed at LNL. Unlike the Tandem, PIAVE can only operate in conjunction with ALPI. The injector exploits an Electron Cyclotron Resonance (ECR) ion source placed on a high voltage platform that can be operated up to 400 kV. Once the high charge and high current ion beams are extracted from the source, they are accelerated with two Superconducting Radio-Frequency Quadrupoles (SRFQ) and 8 superconducting QWR cavities to match the energy at the entrance in ALPI. The combination of electrostatic and superconducting RF accelerators provides heavy ion beams

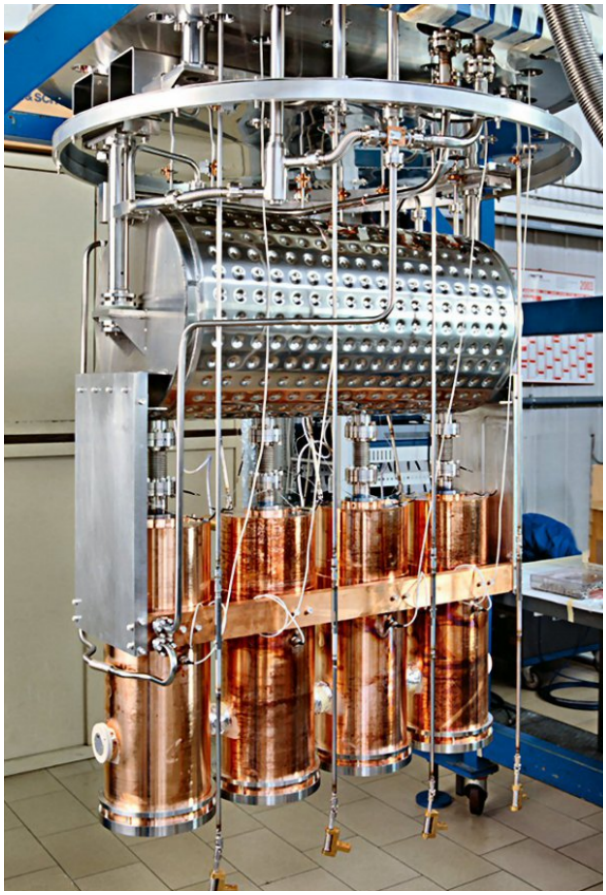

Figure 3.2: Assembled group of 4 accelerating, high purity copper-based, cavities [20].

with energies of up to 20 MeV/u and beam currents of up to 20 pnA.

3.2 The experiment

The medium-mass nuclei decay has been studied over the years by the INFN NUCL-EX collaboration focusing on the possible structure effects. In particular, the comparison of experimental data to statistical-model calculations shows discrepancies that stress non-purely statistical effects in decay channels with even residues where α-particles are emitted, similar to those due to clusterized structures. The ISOLIGHT experiment was proposed to investigate the effect of entrance channel structures (like α-clustering) on the decay modes of excited compound nuclei formed in fusion reactions. In this campaign, the studied reactions are: ^{18}O+^{13}C at 112.5 MeV and ^{18}O+^{12}C at 122 and 300 MeV. The first two reactions are chosen in order to obtain two compound nuclei at the same excitation energy (^{30}Si* and ^{31}Si* respectively). The study of these two reactions, compared to the

even-even CN formed in the system $^{16}O+^{12}C$ ($^{28}Si^{*}$) previously studied by the NUCL-EX collaboration [4], allows us to investigate how the compound nucleus decay depends on the neutron content of the system. On the other hand, the third reaction at a higher energy enables the study of the CN decay mechanisms as a function of the excitation energy. This turns out to be an important tool to indicate whether the cluster structures are still present while drastically increasing the excitation energy.

The ISOLIGHT experiment took place in two phases: the first part was carried out in 2020, while the second one in 2021; more details are reported in Tab. 3.1. Besides the runs to study the physics cases, pulser and elastic scattering runs have been also carried out to test the stability of the electronic chain (SubSec. 2.3.1) and to perform the energy calibration of the detectors (Sec. 3.4), respectively. It must be pointed out that in the

ISOLIGHT part 1 (January 2020) 300 MeV	
Elastic run	$^{18}O+^{197}Au$ at 300 MeV
Pulser run	
Physics run	$^{18}O+^{12}C$ at 300 MeV
Electronics gains change	
Physics run	$^{18}O+^{12}C$ at 300 MeV
ISOLIGHT part 2 (February 2021) 112.5−122 MeV	
Elastic run	$^{18}O+^{197}Au$ at $112.5-122$ MeV
Pulser run	
Physics run	$^{18}O+^{13}C$ at 112.5 MeV and $^{18}O+^{12}C$ at 122 MeV

Table 3.1: Summary of the ISOLIGHT experimental campaign.

first experimental part a change in the electronic gains was made. It was not followed by a further acquisition of elastic runs.

During the experiments the beams are accelerated by the Tandem XTU described above and impinges on a 70 $\frac{\mu g}{cm^2}$ thick ^{nat}C, on a 100 $\frac{\mu g}{cm^2}$ thick ^{13}C and on 200 $\frac{\mu g}{cm^2}$ ^{197}Au targets arranged on a target holder inside the GARFIELD array which can be remotely controlled without opening the chamber and consequently without wasting time in emptying and filling procedures. In order to provide the energy calibration of the detectors, elastic scattering reactions were carried out as well: ^{18}O beams at 122 MeV and at 112.5 MeV impinged on ^{197}Au.

3.2.1 Experimental conditions

Before starting the experiment, it is important to ensure that the beam is focalized on the target position to which the detectors are referred. For this purpose, an additional Al_2O_3 target with a little hole in the center has been used to focalize the beam. Indeed, this material has the property of emitting light when hit by the beam. Therefore, the beam was moved until it completely disappeared inside the hole. As already discussed in Sec. 2.1, the polar angle regions covered by the GARFIELD forward and backward chambers in the laboratory framework are $29,5° \div 82,5°$ and $97,5° \div 150,4°$ respectively. In Tab. 3.2 the angular region ($\theta_{min} \div \theta_{max}$) covered by each GARFIELD CsI(Tl) are reported. Tab. 3.3, instead, reports the polar angle intervals and radii corresponding to

		θ_{min}	θ_{max}	θ_C	**distance (mm)**
	CsI 1	139.9°	150.4°	145.2°	216
GARFIELD	**CsI 2**	127.5°	138.5°	133.0°	194
backward	**CsI 3**	113.5°	126.5°	120.0°	172
	CsI 4	97.5°	112.0°	104.8°	150
	CsI 5	68.0°	82.5°	75.3°	150
GARFIELD	**CsI 6**	53.0°	66.0°	60.0°	172
forward	**CsI 7**	41.0°	52.0°	47.0°	194
	CsI 8	29.5°	40.0°	34.9°	216

Table 3.2: Polar angular region ($\theta_{min} \div \theta_{max}$) covered by each GARFIELD CsI(Tl) crystal. The distance of the scintillators from the target is reported as well. θ_c stands for the angle at which a particle is emitted if it perpendicularly impinges on the crystal face.

each Si strip of the RCo.

During the measurements, a set of triggers was used in order to select events of interest during the acquisition phase. Referring to Tab. 2.1, the runs were acquired enabling triggers N° 3 and 4. They represent the logic OR of Si and the logic OR of CsI(Tl) of the RCo, respectively. These triggers were activated when at least one detector produced a signal enabling the analysis of the events in which at least one particle was detected in the forward cone (RCo). This trigger was chosen because in direct kinematics the reaction products of fusion-evaporation processes are predominantly emitted at forward angles. However, not all strips were included in the OR combination as strips 8 were removed from trigger 3. Indeed, for the systems under study, the grazing angle[5] turns

[5]Angular cut-off value determining whether the projectile will be rejected by the barrier ($\theta > \theta_{gr}$)

	θ_{min}	θ_{max}	Internal radius (mm)	External radius (mm)
Strip 1	15.6°	16.9°	77.9	85.0
Strip 2	14.2°	15.5°	70.8	77.8
Strip 3	12.8°	14.2°	63.7	70.7
Strip 4	11.4°	12.8°	56.6	63.6
Strip 5	10.0°	11.4°	49.4	56.4
Strip 6	8.6°	10.0°	42.4	56.4
Strip 7	7.1°	8.5°	35.2	42.2
Strip 8	5.3°	7.1°	26.2	35.1

Table 3.3: Polar angular region ($\theta_{min} \div \theta_{max}$) covered by each RCo Si strip.

out to be larger than the RCo aperture. The elastic scattering, therefore, can over-stress the strips and in order to protect the strips 8 an aluminium shield was placed in front of them. As a consequence, strips 8 were not responsible for the trigger generation and were acquired only in a slave configuration if the triggers came from the other strips.

3.3 Electronic noise signals rejection

Once acquired, the data must undergo a data reduction process. This step is needed to remove all signals originated from electronic noise exceeding the on-line detection thresholds, being these not caused by physical events. The noise removal is performed by applying conditions on acquisition parameters like for the time constant fraction discriminator t_{cfd} and on baselines of detectors (Fig. 3.3 and Fig. 3.4). The first one is the time at which a constant fraction of the signal amplitude is reached, whereas the second is a mean value calculated from a fixed sample of points at the beginning of the signal and represents a reference point. In conclusion, through the application of thresholds on these signals it can be reliably inferred that what is revealed is due to an actual physical event. Therefore, a collection of "raw" events is obtained.

or overcome the barrier proceeding towards the interior fusing with the target ($\theta < \theta_{gr}$).

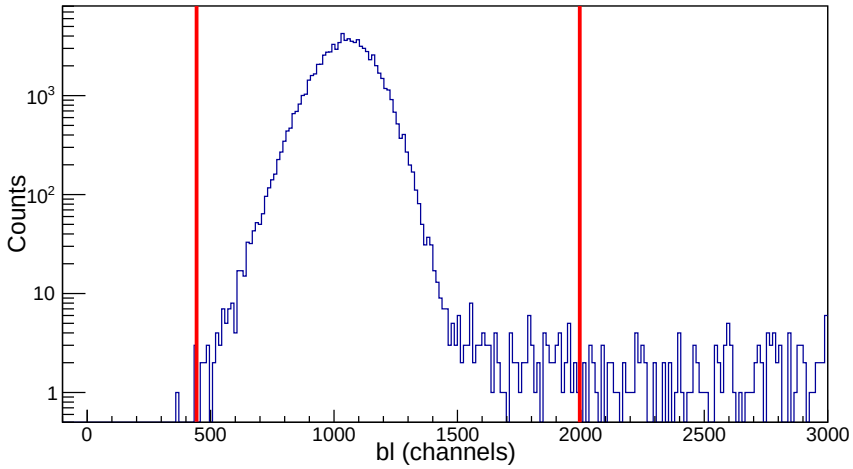

Figure 3.3: Example of thresholds applied to baseline: sector 8 Si strip 1 of the RCo.

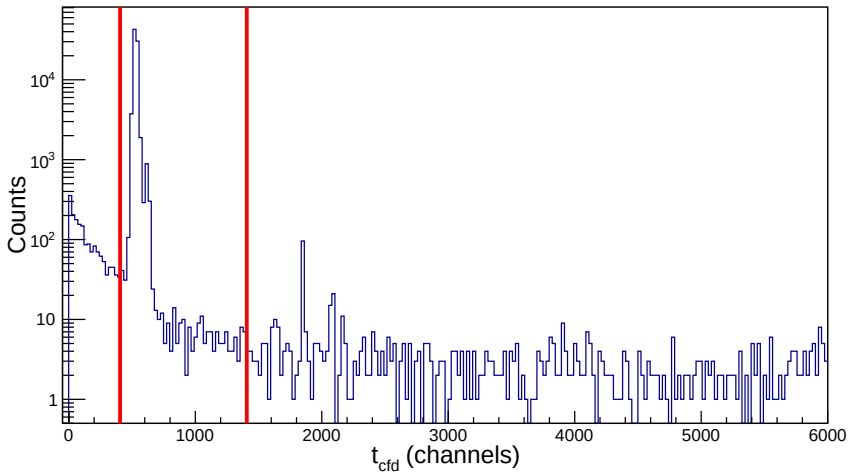

Figure 3.4: Example of thresholds applied to t_{cfd}: sector 8 Si strip 1 of the RCo.

3.4 Energy calibration

A crucial point of the data analysis is the detector energy calibration of each detector of the whole apparatus. It allows us to obtain a conversion factor between the measured energy of the detected particles expressed in channels and the energy expressed in MeV. This procedure turns out to be straightforward for detectors with a linear response to the deposited energy such as the GARFIELD MSGC, the RCo ionization chamber and silicon strips. For these kinds of detectors, the energy calibration can be performed by

associating the peak position of the energy spectrum with the known deposited energy for given particles in specific events, namely elastic scattering reactions. This is the reason why during the experiment some calibration runs with a ^{197}Au target were taken as well. This target was chosen in order to focus on elastic diffusion.

However, other kinds of detectors like CsI(Tl) require more complex calibration procedure. Indeed, the *Light-Output* (*LO*) response of these scintillators is not linearly proportional to the deposited energy in the detector and a simple conversion factor from the LO to the deposited energy cannot be obtained. Although many different attempts to obtain an analytical form to convert the LO to the deposited energy are reported in the literature [21], the NUCL-EX collaboration adopted a semi-empirical formula to express the relation between the LO amplitude in channel and the deposited energy for different values of Z and A. The formula reads

$$LO(Z_{eff}, E) = (d_1 + d_2 e^{-d_3 Z_{eff}})(1 + d_4 Z_{eff}) E^{d_5 - d_6 e^{-d_7 Z_{eff}}} \tag{3.1}$$

where LO dependence on the atomic number and mass number of the incident ion is contained in the $Z_{eff} = (AZ^2)^{1/3}$ factor. The d_i parameters with $i = 1..7$ were set by means of elastic diffusion measurements where the various LO peak positions were easily associated with the calculated deposited energy for ion beams ranging from $Z = 1$ to $Z = 28$ [22]. It is assumed that the uncalibrated light response of the CsI(Tl) has an energy dependence on the energy of the acquired signal that follows Eq. 3.1 with the only exception of a multiplicative factor. In order to obtain this factor, referred to as β-factor by the collaboration, the ratio between the theoretical value for a set of known ions and energies derived by applying the formula 3.1 and the experimental amplitude value is calculated. Even if the Eq. 3.1 has been specifically obtained for the GARFIELD CsI(Tl) crystals, it can also be applied to the RCo scintillators. In this case, however, the presence of the silicon layers must be taken into account. Once the silicon strips have been calibrated (as it will be discussed later), the amount of energy lost in the silicon of each ion that reaches the CsI(Tl) is calculated. When the crossed thickness are known, it is possible to calculate the value of the deposited energy in the CsI(Tl) and apply Eq. 3.1 obtaining a distribution of the points like the one shown in Fig. 3.5. The energy calibration procedure for Si strip detectors and IC of the RCo is explained in details in the following section.

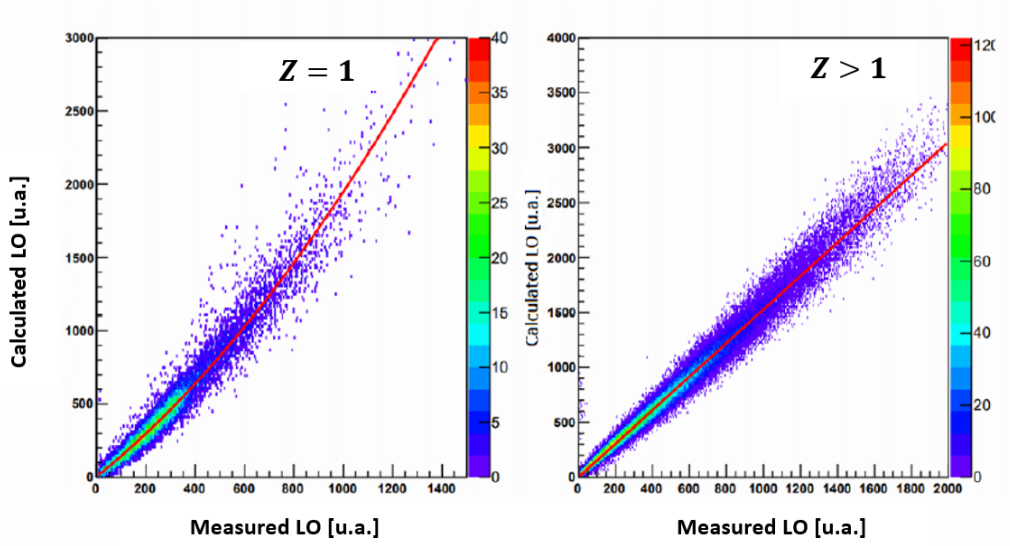

Figure 3.5: Correlation *LO calculated* vs *LO measured* for RCO CsI(Tl) crystals. Distribution for $Z = 1$ fitted through a parabola, while for $Z > 1$ with a straight line. The parameters returned by the fit correspond to the β-factors for the RCo [23].

3.4.1 Energy calibration of RCo IC

The RCo Si strips and IC, together with GARFIELD MSGC, as already mentioned in Sec. 3.4, are detectors with a linear response to the deposited energy. In these cases, the applied calibration procedure is straightforward: the conversion factor between the acquired amplitude in channels to an energy value can be easily obtained by identifying an elastic scattering peak in an energy spectrum. The choice of considering the elastic peak is due to the fact it is a very well-distinguishable physical event and therefore it is possible to select it with high precision. As far as the RCo ionization chamber is concerned, the $^{18}O+^{197}Au$ at 122 and 112.5 MeV elastic scattering runs performed during the measurements have been considered. In practice, in order to get the experimental value in channels of the elastic scattering peak, the $\Delta E - E\ IC - Si$ correlations (Fig. 3.6) have been inspected where the elastic region is clearly distinguishable. Once the elastic peak is graphically cut, the projection on the y axis of this selection is fitted with a gaussian whose mean value corresponds to the experimental value of the energy position of the elastic peak expressed in channels (Fig. 3.7). The experimental points thus obtained are then correlated to the theoretical points, i.e. the calculated deposited energy, obtained from the energy loss tables.

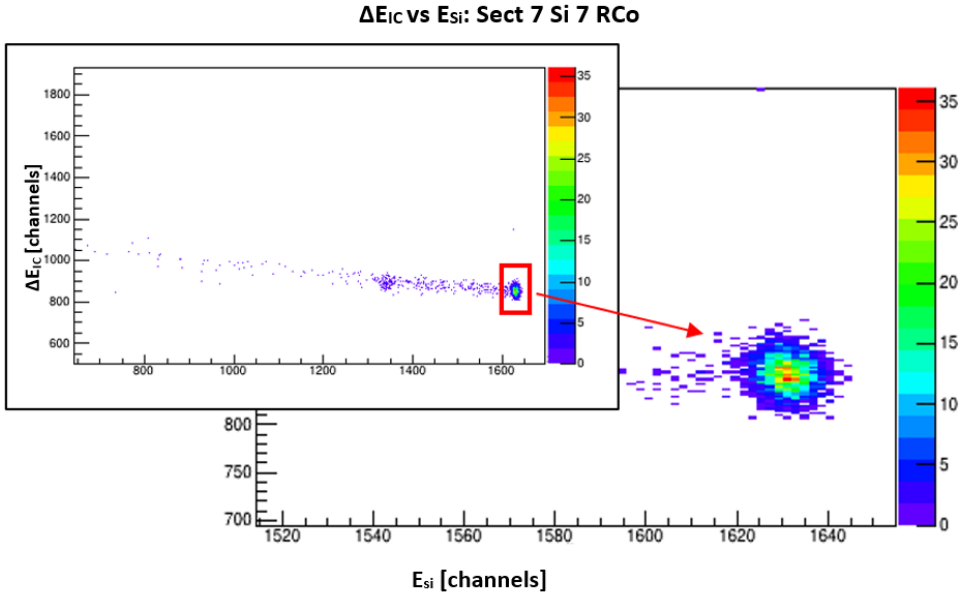

Figure 3.6: $\Delta E - E\ IC - Si$ correlation between IC and Si of sector 7 silicon strip 7 of RCo for the system ^{18}O+^{197}Au at 122 MeV. The insert shows the full correlation whereas the underneath panel shows a zoom on the elastic peak region selected with the red box.

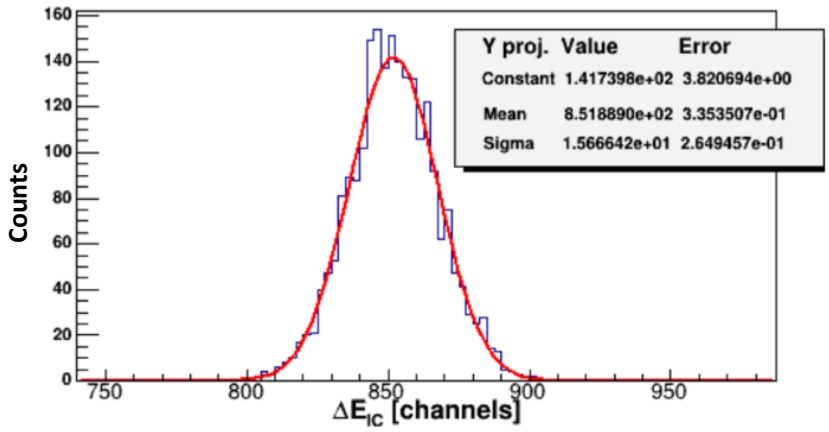

Figure 3.7: Projection on y axis of the underneath plot of Fig. 3.6. The red line is the gaussian fit applied to the curve.

Fig. 3.8 shows the calibration curve including all the aforementioned elastic scattering points. It can be seen how the points follow a linear trend for the energy calibration curve. This allows us to exclude non-linear effects in the reading electronics. The p_0 and p_1 values returned by the fit constitute the calibration parameters which are passed to the package ODIE (Chapter 4), a complex framework developed by the collaboration elaborating raw data set in calibrated physical data.

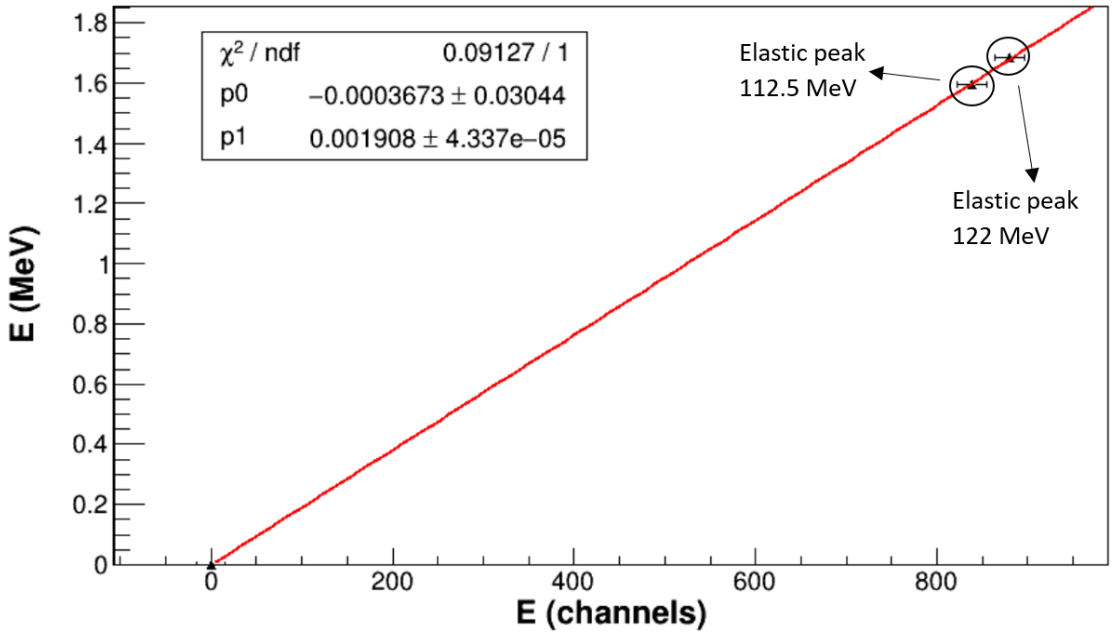

Figure 3.8: Calibration line for RCo ionization chamber for sector 7.

3.4.2 Energy calibration of RCo Silicon strips

For the silicon detectors the scattering diffusion measurements are normally carried out in two separate phases: in the first one the RCo ionization chamber is filled with the gas, while in the second the chamber is emptied. For the measurements without gas, signals coming from the silicon detectors correspond to the energy values calculated from the Rutherford expression for the elastic scattering taking into account the dead layers of the detector. On the other hand, when the gas is present the calculated energy values are obtained by subtracting the energy loss which occurs in the first stage due to the presence of a layer of gas before the Si strip detectors. What is expected is that the measured electric signals in channels are linearly proportional to the energy of the diffused detected particle. Eventually, by fitting these experimental points a curve (line) can be obtained

that best approximates the relation between the amplitude of the signals supplied by the instrumentation and the calculated energy.

As far as the reactions at 112.5 and 122 MeV are concerned, a single energy calibration of the Si detectors is sufficient since the two measurements considered were carried out under the same experimental conditions during the same shift of the experiment (February 2021). In this case, the calibration lines have been extrapolated considering five points as shown in Fig. 3.9. As in the previous case, elastic scattering points have

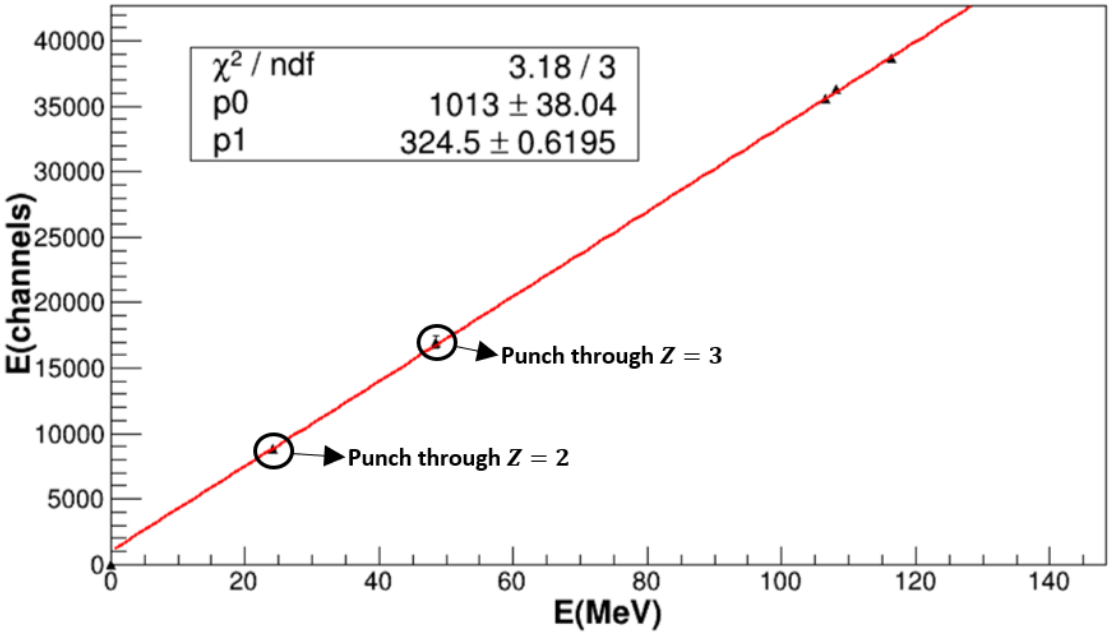

Figure 3.9: Calibration line for RCo sector 4 Silicon strip 5.

been considered which are the three shown in the upper right part of the figure. In particular, starting from the more energetic, they refer to the reaction ^{18}O+^{197}Au at 122 MeV with the gas in the RCo IC, at 112.5 MeV with no gas in the IC and at 112.5 MeV with the gas in RCo. Two additional points have been taken into account which correspond to the energies at which the punch through of the α ($Z = 2$) and of the lithium ($Z = 3$) in the Si strip occurs. In other words, it is the energy above which these particles are detected in the CsI(Tl) of the RCo. In analogy to the experimental position of the elastic peak, the punch through can be selected by inspecting the PSA Si correlations. In the lower panel of the Fig. 3.10 the punch through for $Z = 2$ and $Z = 3$ are highlighted surrounding them with two red circles.

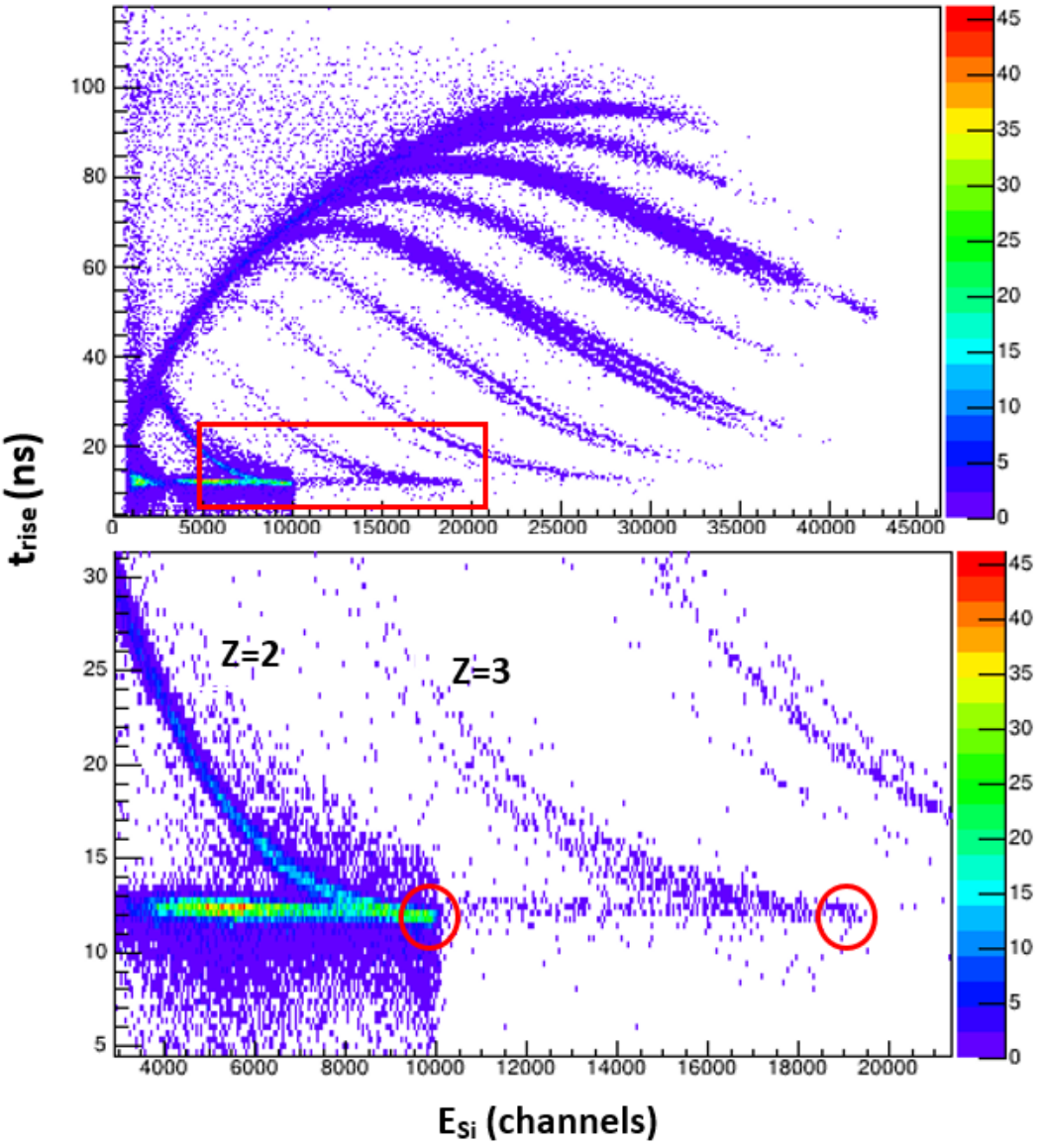

Figure 3.10: Si PSA correlation for the ^{18}O+^{12}C at 122 MeV. Upper panel: Whole E_{Si} and t_{rise} coverage. Lower panel: zoom in the punch through region for $Z = 2$ and $Z = 3$.

As already mentioned, in the first part of the ISOLIGHT experiment no useful elastic runs have been acquired after the change in the electronics gains. Therefore, for the ^{18}O+^{12}C system at 300 MeV 3 calibration points corresponding to the punch through of different particles are taken into account. In particular, the punch through of $Z = 2$

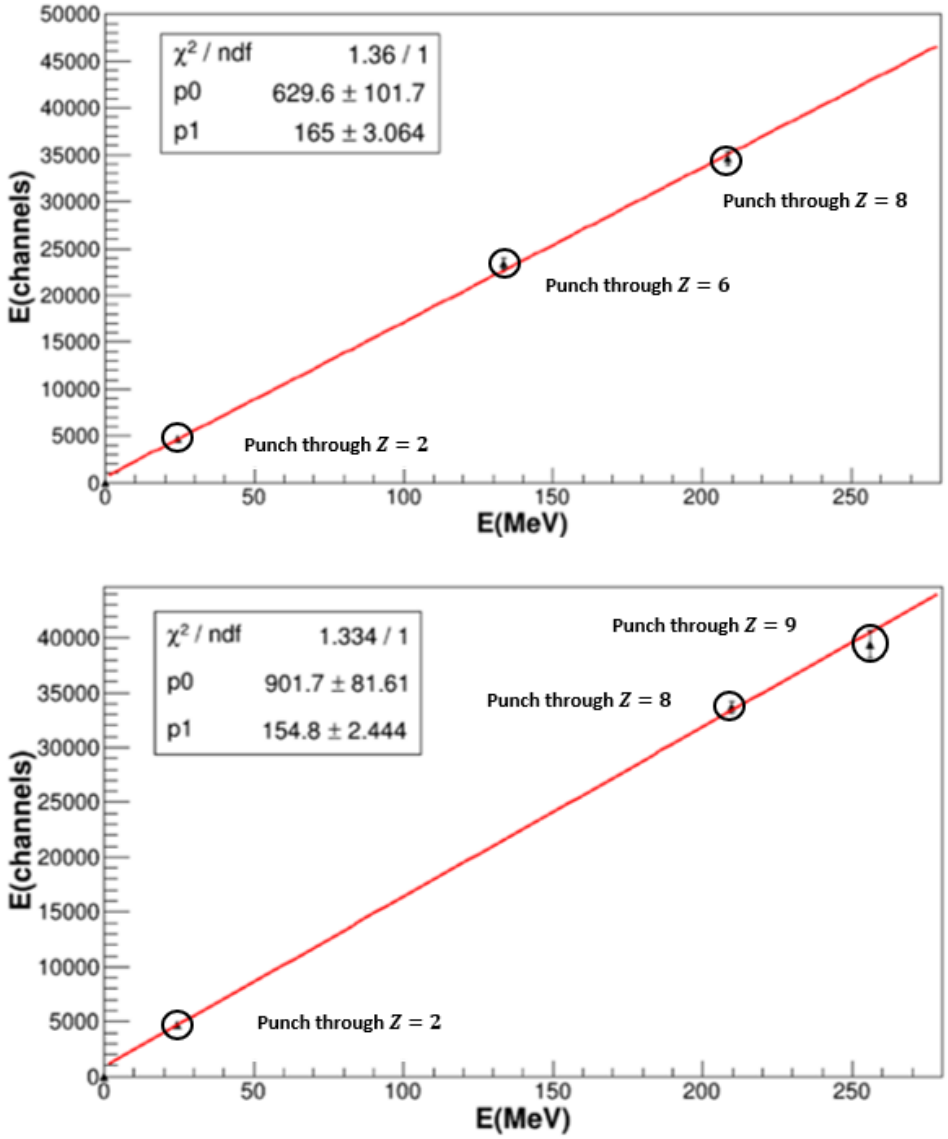

Figure 3.11: Calibration curves for Si strips of RCo for the reaction ^{18}O+^{12}C at 300 MeV. Upper panel: sector 1 Si strip 2. In this case the $Z = 6$ punch through has been considered. Lower panel: sector 2 Si strip 5 with the $Z = 9$ punch through.

and $Z = 8$ are selected for each strips. Moreover, for the third point either the punch through of $Z = 6$ or $Z = 9$ is selected depending on which was better distinguishable in the t_{rise} vs E_{Si} matrices. Fig. 3.11 shows two examples of such calibration, one for each case of third point respectively. Finally, In Fig. 3.12 the punch through selection

for $Z = 6$ and $Z = 9$ are presented in a specific case.

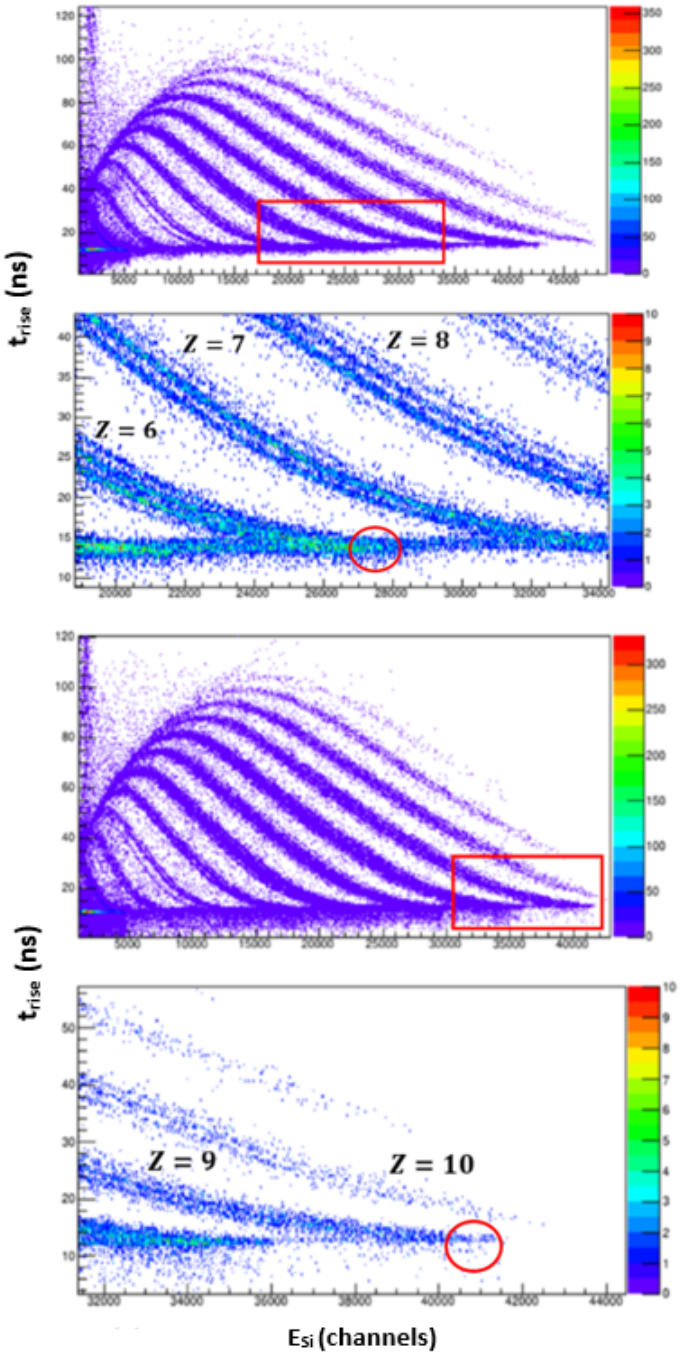

Figure 3.12: First and third panels: typical Si PSA correlation. Zoom on the $Z = 6$ (second panel) and $Z = 9$ (fourth panel) punches through.

3.5 Particle Identification

The GARFIELD+RCo array features a high geometric efficiency which enables the complete reconstruction of the events, when the total charge is detected. The collected data are arranged in a collection of "raw" events each of which features a list of acquisition data parameters characterized by the same event number. These acquired parameters are related to the reaction products and must be analysed in order to reconstruct the dynamics of the interaction and recreate the characteristics of the particles starting from the detectors signals. Therefore, it is evident that the identification of the particles produced in an interaction is one of the most crucial aspects in the study of nuclear reactions. Indeed, the properties of a reaction cannot be investigated without identifying the fragments produced in charge Z and, whenever possible, in mass A.

Several identification techniques are adopted in experimental heavy-ion physics. In the GARFIELD+RCo apparatus the $\Delta E - E$ and PSA are used.

3.5.1 $\Delta E - E$ technique

This identification technique is based on the energy deposited by a particle in two detectors placed sequentially assuming that the particle stops in the second one. This detectors configuration is also known as "counter telescope". The mechanism of energy loss of an ionized particle in a medium of a given density is expressed by the well-known Bethe-Bloch formula which can be approximated as:

$$\frac{dE}{dx} \simeq C\frac{Z^2}{v^2}, \tag{3.2}$$

where dE is the energy lost by the particle in the infinitesimal thickness dx, whereas Z and v are the atomic number and velocity of the particle, respectively. C is a constant depending on the material. In the non-relativistic limit, the kinetic energy E of a particle of mass M is given by:

$$E = \frac{1}{2}Mv^2. \tag{3.3}$$

By combining the two previous equations one obtains [24]:

$$\frac{dE}{dx} \propto \frac{Z^2 M}{E}. \tag{3.4}$$

Therefore, the energy loss inside a material is proportional to the square of the impinging particle charge and it increases linearly with the mass of the particle, while it decreases with energy. If one draws the correlation between the energy lost (ΔE) by the particle when crossing the first detector and the energy deposited (E_{res}) in the second, it is observed that particles are arranged along distinct curves for different values of the product Z^2M, being $\Delta E + E_{res}$ the incident energy E. It is worth noting that being

the atomic number the same, a separation depending on the mass still occurs. However, particles can be identified both in charge and in mass only if the detectors used in the first stage of the telescope (ΔE) have a good energy resolution. The $\Delta E - E$ correlation can be performed for: GARFIELD forward chamber vs CsI(Tl), in RCo IC vs Si telescope and in RCo Si vs CsI(Tl). Examples of both different $\Delta E - E$ correlations for the RCo are shown in Fig. 3.13. It should be noted that only light particles can reach the

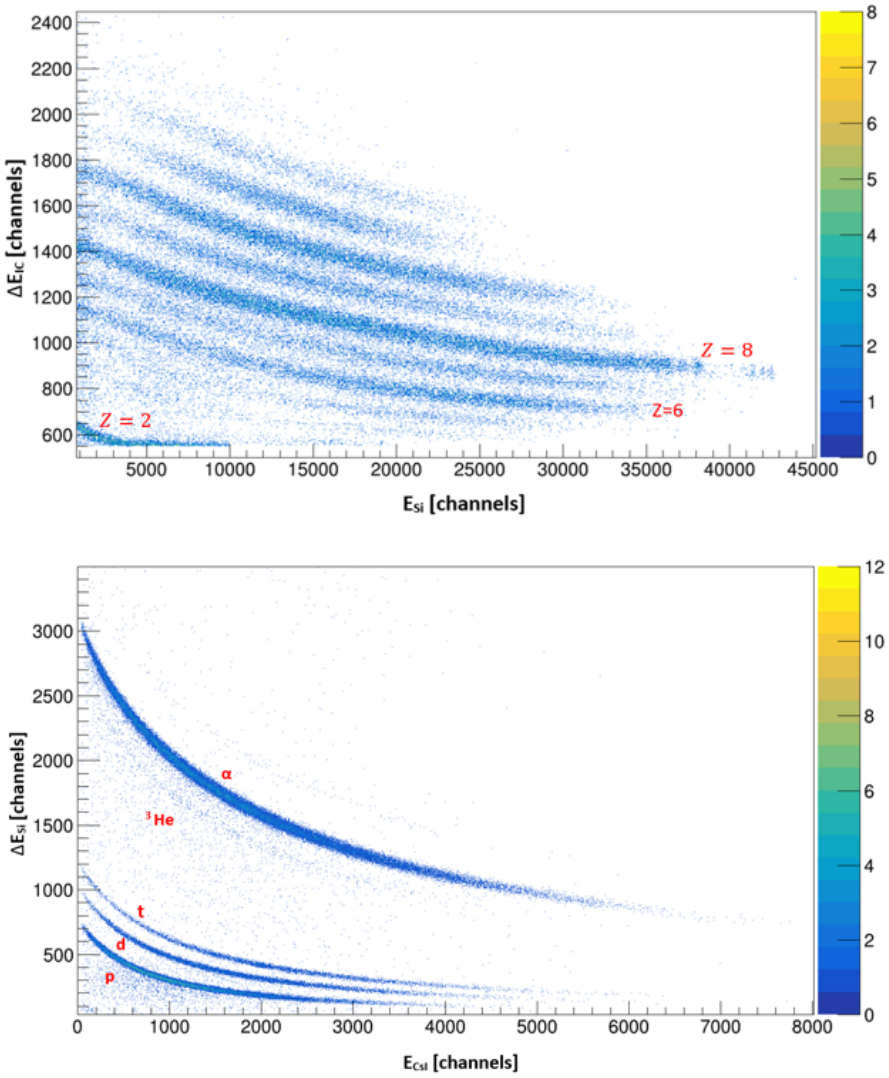

Figure 3.13: Possible $\Delta E - E$ correlation for the RCo for ^{18}O+^{nat}C at 122 MeV reaction. Upper panel: $\Delta E - E$ correlation of IC sector 1 and Si strip 1 of RCo. Here, Z values up to $Z = 12$ can be distinguished. Lower panel: $\Delta E - E$ correlation for sector 3 Si strip 1 and Cesium 2. Protons (p), deuterons (d), tritons (t), ^{3}He and α can be identified.

CsI(Tl) through the first two stages of detection in the studied reaction. Furthermore, from a comparison of the two plots it can be seen that the Si-CsI correlation allows an isotopic separation (of helium and hydrogen) unlike the IC−Si correlation. As far as the GARFIELD apparatus is concerned, the $\Delta E - E$ approach is used for the signals coming from the microstrip electrodes and the CsI(Tl) scintillators. i.e. MSGC−CsI(Tl) telescope (as shown in Fig. 3.14). Also in this case only the identification in terms of charge can be carried out.

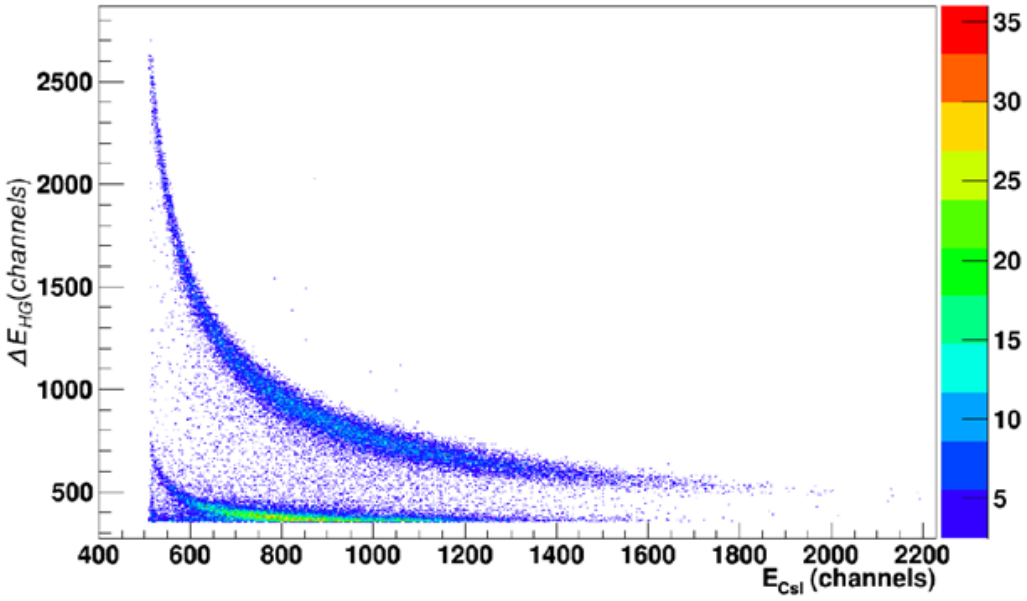

Figure 3.14: $\Delta E - E$ correlation of MSGC−CsI(Tl) telescope in GARFIELD apparatus. Correlation for sector 13 and cesium 8 [25].

3.5.2 Pulse Shape Analysis (PSA) technique

The $\Delta E - E$ identification technique cannot be applied, for instance if the ion stops in the first stage of the telescope configuration. However, Si strips and CsI(Tl) scintillators enable particle identification through an analysis of the shape of the signal induced by the particle in the detector.

Fast-Slow PSA in CsI(Tl)

In Chapter 2, it has been widely described how the scintillation phenomenon occurs in CsI(Tl) crystals and that the shape of light pulses emitted by the scintillators depends on the type of incident radiation, i.e. on the energy, as well as on the charge Z and mass A of the particles. Indeed, the emission spectrum is given by the sum of the *fast*

and *slow* components whose time constant values depend on Z and A of the ion and on its energy. Therefore, the fast and slow components of the CsI(Tl) signals provide a correlation for the particle identification in both GARFIELD and RCo. The two components are extracted by the DSP (*Digital Signal Processor*) by applying two filters with the two different constants to the pre-amplified CsI(Tl) signals. Fig. 3.15 shows the reproduction of the light response of a scintillator as a function of the time and of the deposited energy for several ions.

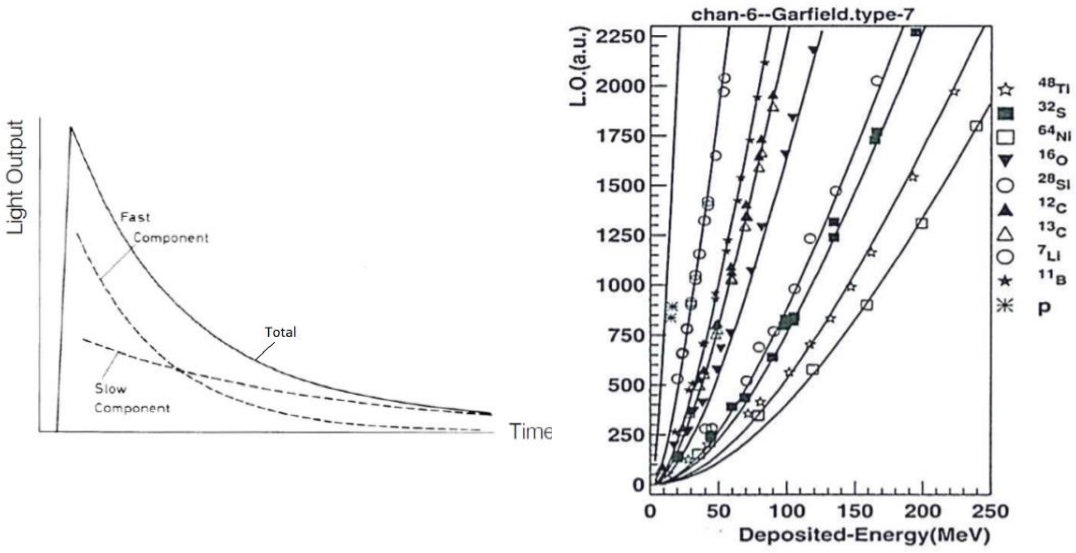

Figure 3.15: Left: light output of a scintillator as a function of time. The slow and fast components are shown separated in order to show the respective contribution to the total response. Right: light output of a GARFIELD-type CsI(Tl) crystal as a function of the deposited energy for several ions [26].

However, a better isotopic separation is achieved if a new parameter obtained from a linear mixing of the two components is used in place of the direct fast-slow correlation. Therefore, what is performed is a correlation between the fast component and the *SlowPSA* (spsa) defined as:

$$SlowPSA = 3.5 \cdot (slow - 4fast). \tag{3.5}$$

Some *"Fast vs SlowPSA"* correlation matrices for a GARFIELD and RCo CsI(Tl) detector are shown in Fig. 3.16.

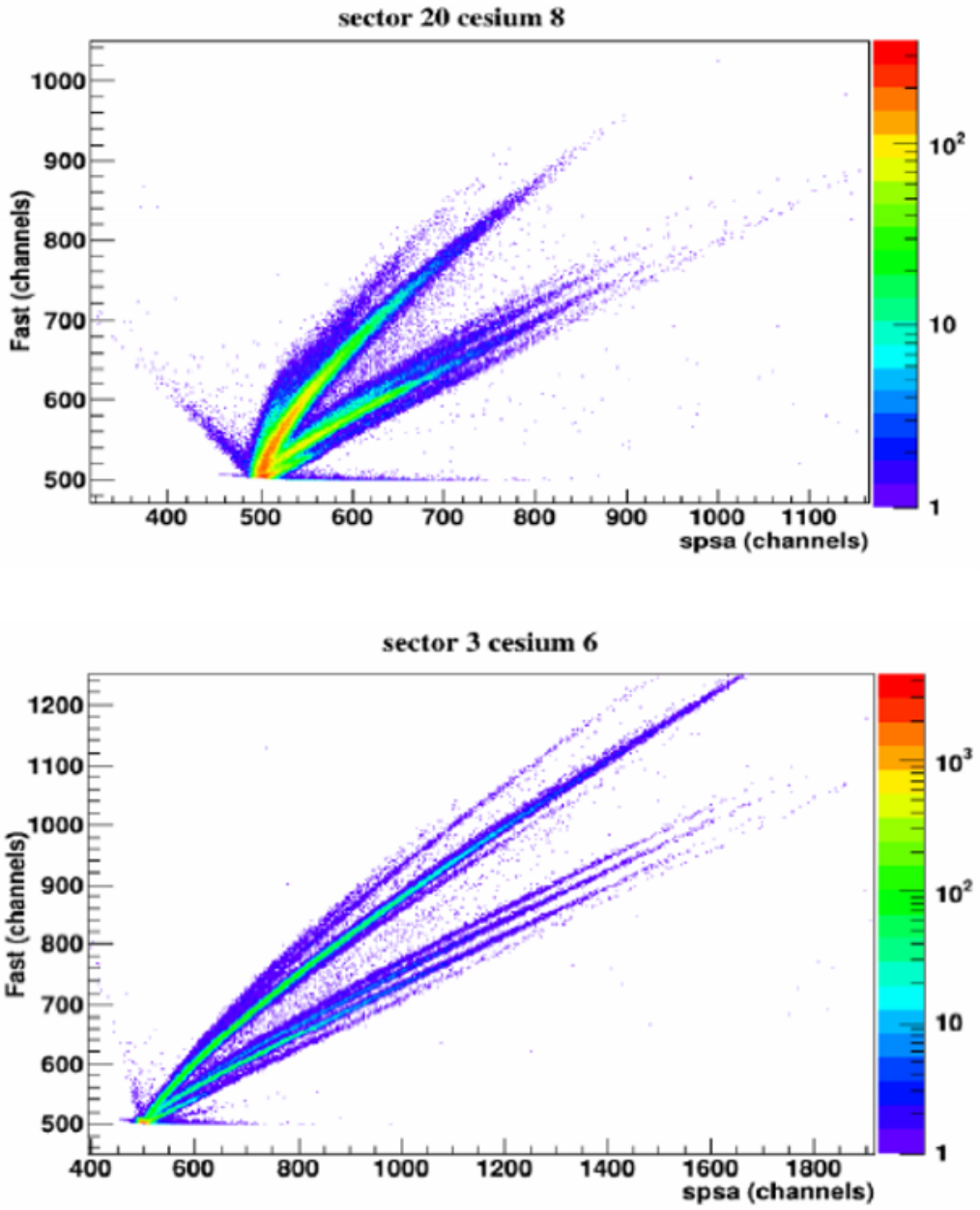

Figure 3.16: *"Fast vs spsa"* correlation for the sector 20 cesium 8 of GARFIELD (upper panel). From the bottom the ridges corresponding to γ, ,p, d, t and α particles can be recognized. The same correlation is shown for sector 3 cesium 6 of the RCo (lower panel). Here above the ridges corresponding to tritons, ^{3}He, α and Li are clearly visible [25].

PSA in Si strips

As previously mentioned, the PSA technique can be also used for Si strip in order to identify the reaction products in terms of both charge and mass.

When a particle passes through the sensitive volume of the silicon detector, it creates a linear density of electron-hole pairs. Being the energy of the impinging particles the same, heavier ions tend to create more pairs forming a plasma region weakening the electric field. A lower electric field implies a longer time needed for the produced charges to be collected by the electrodes. Therefore, the charge signal *rise time* will be also longer, accordingly. The *rise time* of a signal is defined as the time interval required for the signal to pass from 20% to 80% of its full amplitude. Applying correlation between the energy detected in the silicon strip and the rise time of the signal produced by the same detector a matrix of the kind shown in Fig. 3.17 is obtained.

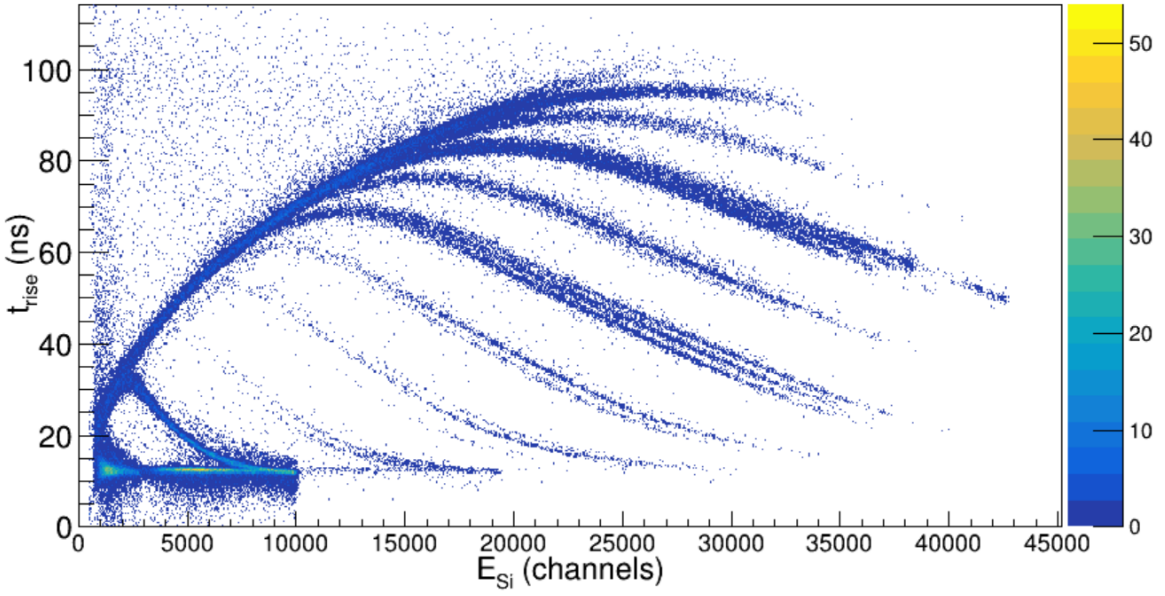

Figure 3.17: Silicon PSA "*rise-time* vs energy" correlations for the reaction $^{18}O+^{12}C$ at 122 MeV. The matrix refers to strip 1 of sector 1 of the RCo.

3.5.3 Identification procedure

In this paragraph the procedure for the charge and mass identification of the reaction products is described. As an example, the identification procedure is detailed for the fast-slow correlation of the GARFIELD CsI(Tl) for the reaction at 300 MeV. However, it can also be applied to correlations obtained by means of a $\Delta E - E$ telescope and to Si PSA correlations without loss of generality. Starting from the correlation matrix of interest, lines and contours are drawn through points directly identified on the ridges of well defined isotopes. Generally, these are easily recognized due to their abundance or their separation from other charges and/or masses. This is done using a ROOT code in C++ providing a graphical interface with which lines and contours can be manually inserted on the 2D histograms. In Figure 3.18, a typical case is shown, namely the fast-slow matrix of the CSI(Tl) 5 of sector 2 of the RCo. It can be noticed that each line

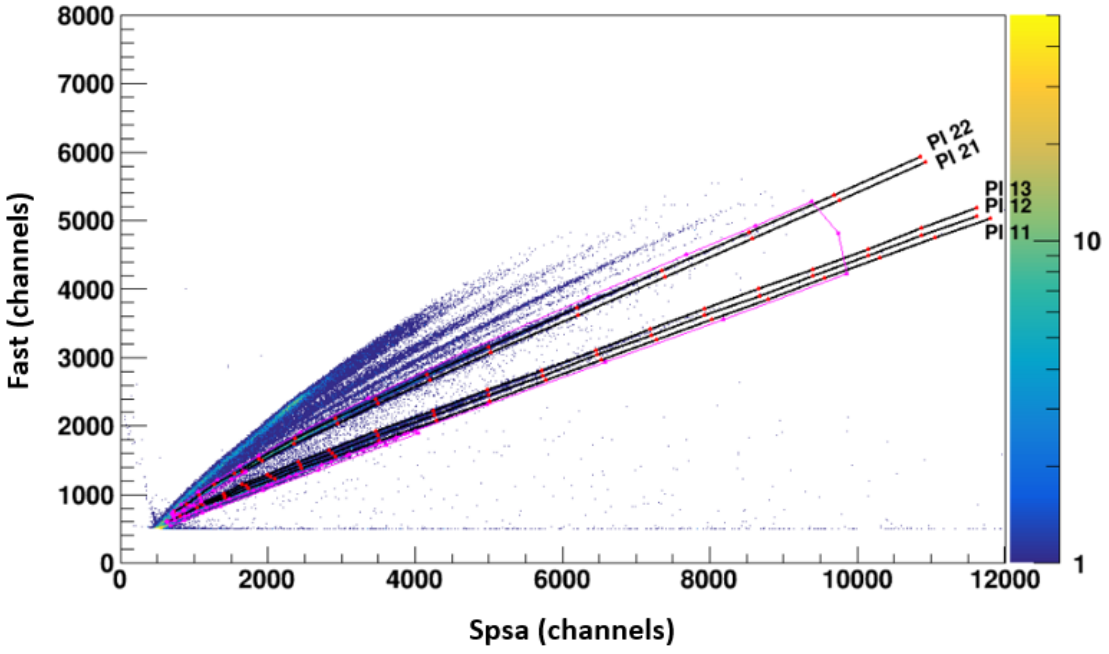

Figure 3.18: Lines for isotopic particle identification drawn for the RCo CsI(Tl) PSA correlation for ^{18}O+^{12}C at 300 MeV system. From top to bottom: ^{4}He, ^{3}He, tritons, deuterons and protons. The contours are drawn in pink.

identifies a particular isotope with a proper associated code according to the following legend:

PI 22 $\rightarrow$ ^{4}He

PI 21 $\rightarrow$ ^{3}He

PI 13 $\rightarrow$ t

PI 12 $\rightarrow$ d

PI 11 $\rightarrow$ p

Heavier elements than α are not identified from this correlation since they are better discernible in the correlation matrices of initial detection stages ($IC - Si$). Regarding the contours, they have a multiple function. For instance, a contour labelled id_cut = 11 is drawn where protons, deuterons and tritons cannot be distinguished, as in the region preceding the line bifurcation. In this way, everything that falls inside this contour is identified as $Z = 1$ and $A = 1$. The same is done for ^{3}He and α, but in this case the id_cut of the contour is 22 and everything is identified as $Z = 2$ and $A = 4$. On the other hand, below protons an id_cut = 10 contour is drawn in order to identify neutral particles or charged particles only partially detected which will then be rejected [27]. Finally, a contour with id_cut = 100 defines the area in which the isotopic particle identification is possible. The aforementioned contours are shown in Fig.3.18 as well. Moreover, Fig.3.19 shows a zoom of the previous one for a better view of the contours. Once lines and contours are drawn, the points coordinates and the PI labels are saved in

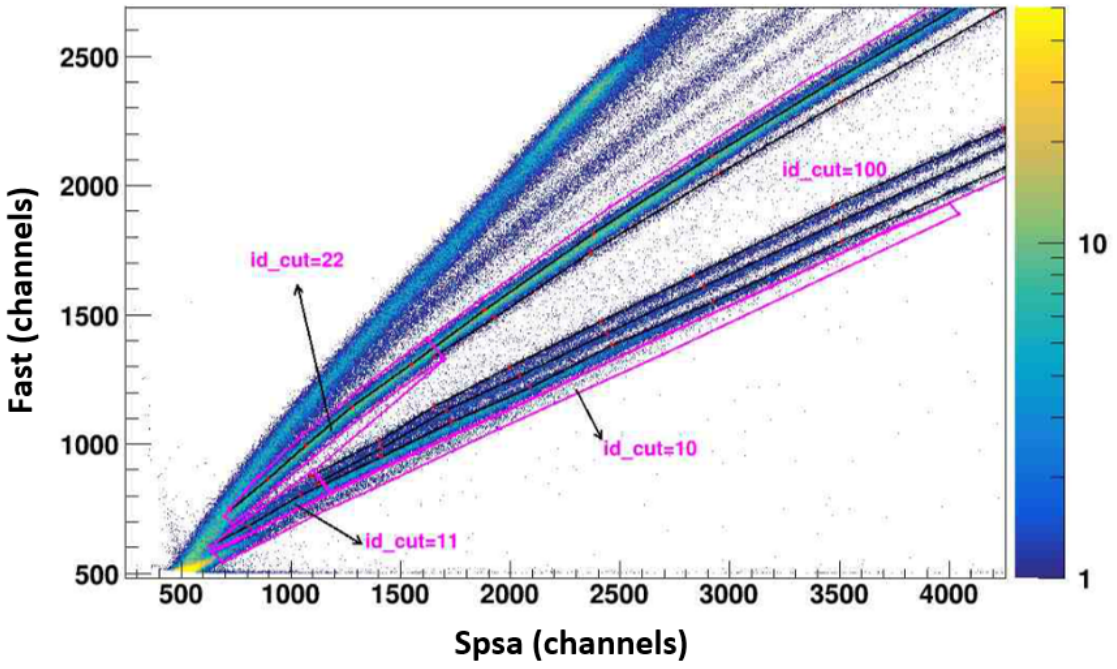

Figure 3.19: Zoom of Fig. 3.18. Identification cuts of each contour can be clearly seen.

the ODIE database. At this stage, to each fragments a point $(x_0,\ y_0)$ of the appropriate correlation is associated. A PI label is assigned to the fragment by interpolating between the values associated with the closest curves. Interpolation can be made either on the basis of the distance from the curve or on the basis of the ordinate value, being the latter the commonly applied method. Basically, given an experimental point $(x_0,\ y_0)$ its identification parameter is obtained as

$$PI_0 = PI_1 + \frac{(y_0 - y_1)(PI_2 - PI_1)}{y_2 - y_1} \tag{3.6}$$

where y_1 and y_2 are the ordinates of the intersection point between the $x = x_0$ line and the curves closest to the experimental point with labels PI_1 and PI_2. The described procedure is equivalent to a "linearization" of the curves by means of a transformation of the plan. In analogy with the identification procedure carried out in RCo CsI(Tl) for the 300 MeV reaction, similar lines and contours were drawn also for the fast-slow for the matrices of the reactions at 122 and 112.5 MeV (Fig. 3.20). As already mentioned,

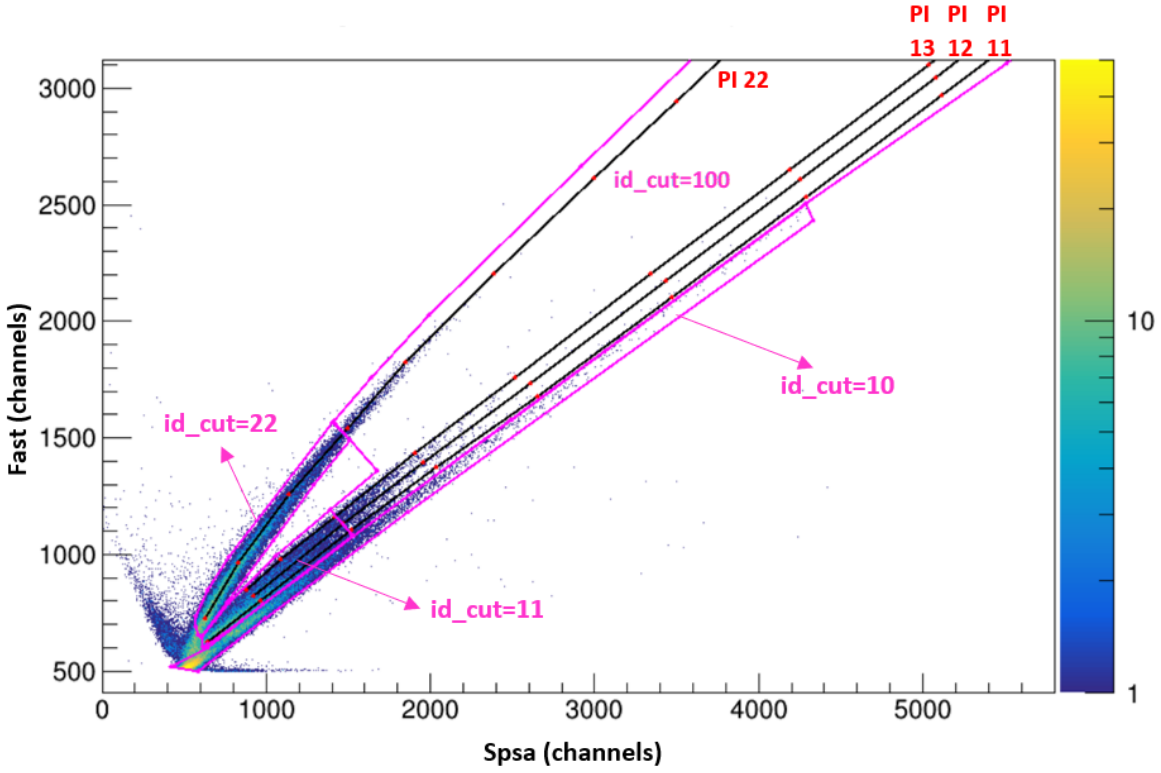

Figure 3.20: Lines for isotopic particle identification drawn for the RCo CsI(Tl) PSA correlation for ^{18}O+^{12}C at 122 MeV system. From top to bottom: ^{4}He, tritons, deuterons and protons. The contours are drawn in pink.

a similar procedure is also applied to the other types of correlations. Fig. 3.21 shows the

identification lines and contours for the $\Delta E - E$ correlation of Si-CsI(Tl) of the RCo. Here, a distinction can be made among

PI 33 $\rightarrow$ ^{8}Li

PI 32 $\rightarrow$ ^{7}Li

PI 31 $\rightarrow$ ^{6}Li

PI 24 $\rightarrow$ ^{6}He

PI 22 $\rightarrow$ ^{4}He

PI 21 $\rightarrow$ ^{3}He

PI 13 $\rightarrow$ t

PI 12 $\rightarrow$ d

PI 11 $\rightarrow$ p

In this case the contour, namely 999, is used to identify the noise.

3.6 Experimental events

In order to reconstruct the experimental events the framework ODIE is used. It consists in a software package for switching from the raw data acquired during measurement to calibrated data complete with particle identification and energy calibration. ODIE is based on object-oriented programming in CERN's ROOT environment, and was developed by the Florence section for the NUCL-EX collaboration. The data flow through the various parts of ODIE occurs by means of XML (*eXtensible Markup Language*) files generating a hierarchical-functional structure made up of objects called *workers*. These receive input data from the higher level workers and produce output data for the lower level ones. After determining all the identification and calibration parameters with the procedures described in Chapter 3, ODIE is launched in its entire structure. Each worker accesses a database containing the above mentioned parameters distinguishable for various run intervals. In the last workers an object of type TTree is filled. Each entry corresponds to an event containing particles characterized by atomic number Z, mass number A, kinetic energy E and polar θ and azimuth ϕ angles.

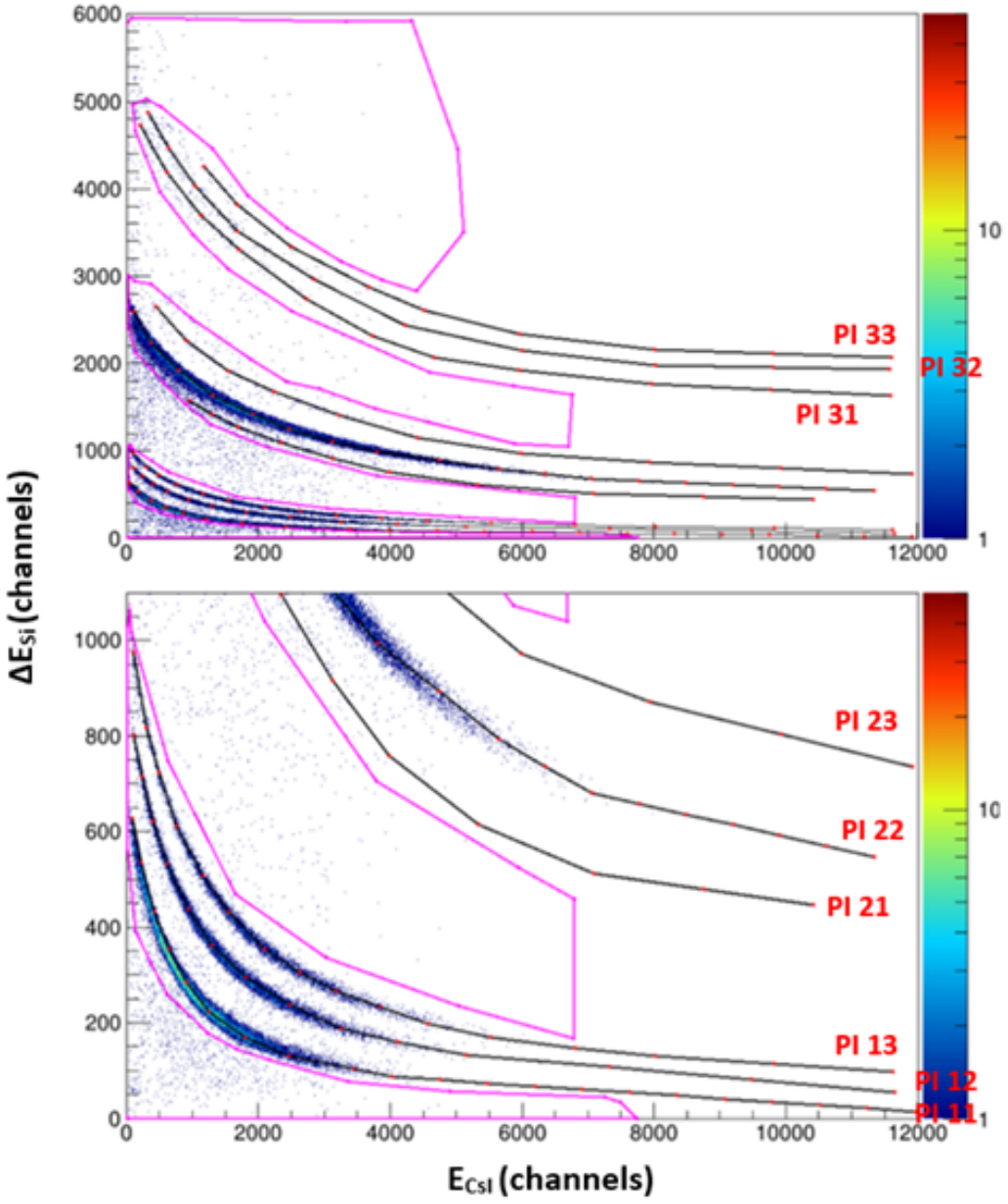

Figure 3.21: Upper panel: lines for isotopic particle identification and contours drawn for $\Delta E - E$ correlation of Si-CsI(Tl) of the RCo ^{18}O+^{12}C at 122 MeV reaction. Lower panel: zoom on the isotopic line identification for lighter elements. By inspeting both panels from top to bottom there are: ^{8}Li, ^{7}Li, ^{6}Li, ^{6}He, ^{4}He, ^{3}He, tritons, deuterons and protons.

Chapter 4

Data Analysis

Further insights on the fusion evaporation reactions can be gained from statistical model calculations. A preliminary study of simulated data allows to obtain a feedback of how this reaction mechanism is expected to be. In Sec. 4.1 a brief description of the Monte Carlo statistical decay codes GEMINI++ and HFℓ is reported. After a short description of the software simulating all the characteristics of the experimental array, the distributions of several variables for the single reaction ^{18}O+^{12}C at 122 MeV are compared for different data selections in order to evaluate the effects of the applied experimental filter (Sec. 4.2). Sec. 4.3 is focused on a comparison of the three studied reactions: ^{18}O+^{13}C at 112.5 MeV and ^{18}O+^{12}C at 122 and 300 MeV. Sec. 4.4, finally, deals with a direct comparison between simulated data provided by GEMINI++ and HFℓ codes for the system ^{18}O+^{12}C at 122 MeV.

4.1 Simulation codes

Monte Carlo simulation codes based on statistical models have proved to be a very effective tool in describing the evolution of fusion-evaporation reactions and the decay chain of the formed compound nucleus.
In this thesis, events simulated by the GEMINI ++ and HFℓ codes have been considered. The simulated data are filtered through a software replica of the experimental setup in order to be compared to the experimental ones when they will be available.

GEMINI++ is a code widely used in the field of heavy ion nuclear physics, while HFℓ was developed and optimized for lighter systems by the NUCL-EX collaboration. Both codes are based on the Hauser-Feshback formalism which explicitly considers and conserves angular momentum [28].

4.1.1 GEMINI++

GEMINI++ is a code based on the statistical decay model and describes complex-fragment emission from an hot source. It assumes the decay of the compound nucleus as a series of binary decays until these decays become impossible due to energy conservation or improbable due to the competition with γ-ray emission. Being this code conceived to analyze the CN decay following heavy ions fusion reactions, the effects of large angular momentum values on the decay chain are explicitly taken into account. For this reason, this statistical code does not cover only binary-decay modes to nucleon and light-nucleus evaporation (dominant channels), but also considers the fission channel which becomes relevant for high spin values. The Hauser-Fesbach formalism is adopted for the light particle evaporation from CN, whereas the Bohr-Wheeler one-dimensional transition state formalism is used to describe the fission channel. According to the Hauser-Feshbach formalism, the partial evaporation decay width of the $i^{th}-$particle from a CN with excitation energy E^* and total angular momentum J_{CN} is given by:

$$\Gamma_i(E^*, J_{CN}) = \frac{1}{2\pi\rho_{CN}(E^*, J_{CN})} \int d\varepsilon \sum_{J=0}^{\infty} \sum_{J=|J_{CN}-J_d|}^{J_{CN}+J_d} \sum_{l=|J-S_i|}^{J+S_i} T_l(\varepsilon)\rho_d(E^*-B_i-\varepsilon, J_d) \quad (4.1)$$

where

- J_d is the total angular momentum of the residue;
- ε and B_i represent the kinetic and separation energies of the evaporated particle, whereas S_i, J and l are its spin, total angular momentum and orbital angular momentum, respectively;
- T_l is the transmission coefficient;
- ρ_d and of ρ_{CN} are the level densities of the residue and CN, respectively.

The sum includes all possible angular momentum couplings between initial and final states. The ρ_d and ρ_{CN} nuclear level densities can be approximately calculated via the Fermi-gas formula:

$$\rho_{FG}(E^*, J) \sim exp(2\sqrt{a(U)U}), \quad (4.2)$$

where J is the spin and U the thermal excitation energy given by the difference between the excitation energy E^* and the rotational energy $E_{rot}(J)$:

$$U = E^* - E_{rot}(J), \quad (4.3)$$

and $a(U)$ is the level density parameter. GEMINI++ generalizes the Eq.4.3 by replacing $E_{rot}(J)$ with the Yrast line $E_{Yrast}(J)$ obtained with models considering the collective behaviour of nucleons inside the nucleus. Hence, the evaporation spectra from the CN over a large range of excitation energies depend on:

- the level density parameter,
- the nucleus excitation energy,
- the transmission coefficient,
- the angular momentum dependence of $E_{Yrast}(J)$.

The level density parameter affects the slope of the exponential tail of the evaporation spectrum the inverse of which is correlated to the nuclear temperature of the source.

By means of the detailed balance principle, the transmission coefficients for charged particle evaporation are obtained considering the inverse reaction. Even though the latter corresponds to the absorption of particles by a hot and rotating nucleus, data from particles absorption by "cold" nuclei are used in the calculation of the transmission coefficients in GEMINI++. Therefore, in order to consider possible thermal fluctuations of the nuclear surface the transmission coefficients in GEMINI++ are calculated as the average of the three transmission coefficients obtained via the *Incoming Wave Boundary Condition* (IWBC) method calculated with three radius parameters of the nuclear potential, R_0, $R_0 - \delta r$, $R_0 + \delta r$:

$$T_l(\epsilon) = \frac{T_l^{R_0-\delta r}(\epsilon) + T_l^{R_0}(\epsilon) + T_l^{R_0+\delta r}(\epsilon)}{3}, \tag{4.4}$$

where the δr parameter is directly proportional to the square root of temperature T of the residue and the original radius R_0 of the nuclear potential. The dependence on E_{Yrast} has a strong impact on the heaviest evaporated particles (i.e. α particles) which can carry away from the emitting nucleus a considerable fraction of the total angular momentum J. For these particles, the functional shape of $E_{Yrast}(J)$ can lead to significant changes in yields and shape of energy spectra. This applies to both the exponential tail of distribution and the Coulombian barrier region.

4.1.2 HFℓ

HFℓ is a statistical MC decay code used to describe the evaporation mechanism from the compound nucleus. It has been developed by the NUCL-EX collaboration and like GEMINI++ is based on the Hauser-Feshbach formalism. While GEMINI++ also deals with fission, HFℓ only covers evaporation and has been optimized for the description of lighter systems. The parametrization of the partial decay amplitude is similar to the one reported in eq.4.1 for GEMINI++. However, the transmission coefficients read as:

$$T_l(\epsilon) = \frac{1}{1 + exp(\frac{V_b-\epsilon}{\delta-V_b})}, \tag{4.5}$$

where V_b represents the sum of the Coulombian potential and the centrifugal term depending on l [29]. Its full expression is:

$$V_b = \frac{1.44}{r_Z}\frac{Z_p(Z-Z_p)}{(A-A_p)^{1/3}+A_p^{1/3}} + \frac{\hbar l(l+1)}{2r_Z^2}\frac{\frac{A}{A_p(A-A_p)}}{[(A-A_p)^{1/3}+A_p^{1/3}]^2}. \tag{4.6}$$

Here (Z, A) and (Z_p, A_p) are atomic number and mass of the CN and of the evaporated particle, respectively. δ and r_Z are free parameters optimized to reproduce the decay of discrete resonances. Unlike GEMINI++, thermal fluctuations of the nuclear surfaces are not taken into account due to the relatively low contribution for light nuclei of the Coulomb barrier.

Concerning the level density, the approach of the *Back-Shifted Fermi Gas* (BSFG) model has been adopted in which the shift of the energy levels of each nucleus due to the pairing interaction is considered. The analytical formula for the levels density:

$$\rho(E^*) = \frac{exp[2\sqrt{a(E^*-E_2)}]}{12\sqrt{2}\sigma a^{1/4}(E^*-E_2)^{5/4}}, \tag{4.7}$$

is adopted as a fit function for the known experimental levels of a given nucleus [30]. The levels density a and the shift E_2 parameters are regarded as free and their values are determined for each nuclide in order to best reproduce the experimental levels known by the above analytical formula.

4.2 Effects of the experimental filtering procedure

Within the NUCL-EX collaboration, a software has been developed in order to simulate the detection threshold and angular coverage of the GARFIELD apparatus. In order to illustrate the effects of the applied experimental filter on the MC data set, some global and single particle observable distributions are investigated for the ^{18}O+^{12}C reaction at 122 MeV. Moreover, different increasingly stringent selections are applied to the data set to show their effects. Firstly, the Monte Carlo generated samples (10^7 events) characterized by the formation of a compound nucleus ($Z_{tot} = 14$) and its subsequent decay are considered. Hereafter, these data are referred to as *G++ all events*. The CN can decay both with evaporation of particles or with fission. Secondly, in order to choose only the fusion-evaporation events, of fundamental importance within this work, a first selection was applied. GEMINI++ provides two subsets of data: one related to the evaporative decay and the other producing the fission fragments. The subset producing the evaporative particles and the residue has been selected by enabling the MC *isresidue* flag. In the following, we refer to such data as *G++ fus-evap events*. Thirdly, the experimental filter software is applied to this set of data. This software, developed within the NUCLEX collaboration, simulates the geometry (covered angles, dead spaces, etc.),

the energy thresholds and the detectors efficiency of the GARFIELD + RCo apparatus. The simulated filtered data through the apparatus are labeled, hereafter, as *G++ filtered fus-evap events*. Finally, an experimental-like selection is applied to choose the complete events, i.e. those completely reconstructed in terms of charge. These events are labeled in the following as *G++ complete events*.

While the pure generated samples (*G++ all events* and *G++ fus-evap events*) represent the unbiased physics behind the reaction, the two filtered data sets (*G++ filtered fus-evap events* and *G++ complete events*) correspond to the physics reconstructed by the experimental apparatus.

Considering the above mentioned selections, by means of a cross comparison between the different data sets the following information can be inferred:

- A comparison between the *G++ all events* set and the *G++ fus-evap events* provides information on how the reaction topology changes when selecting only the fusion-evaporation channel.
- The *G++ filtered fus-evap events* are affected by the apparatus limited efficiency. Therefore, whole events or only some particles of the events are lost. A comparison between these events and the *G++ fus-evap events* provides information on how many events are lost due to the efficiency and angular acceptance of the apparatus.
- Since the *G++ fus-evap events* and *G++ complete events* correspond to the same physical events, a difference between the two provides information on how many and which complete events are lost due to the reconstruction efficiency of the apparatus.

In all the plots shown in this section, the various selections are represented with a colour schema as follows:

- black line for the *G++ all events*;
- green line for the *G++ fus-evap events*;
- red line for the *G++ filtered fus-evap events*;
- blue line for the *G++ complete events*.

4.2.1 Global observable distributions

The event multiplicity and charge distributions of the GEMINI++ simulated events for the reaction at $^{18}O+^{12}C$ 122 MeV under the four different selections are reported in Fig. 4.1.

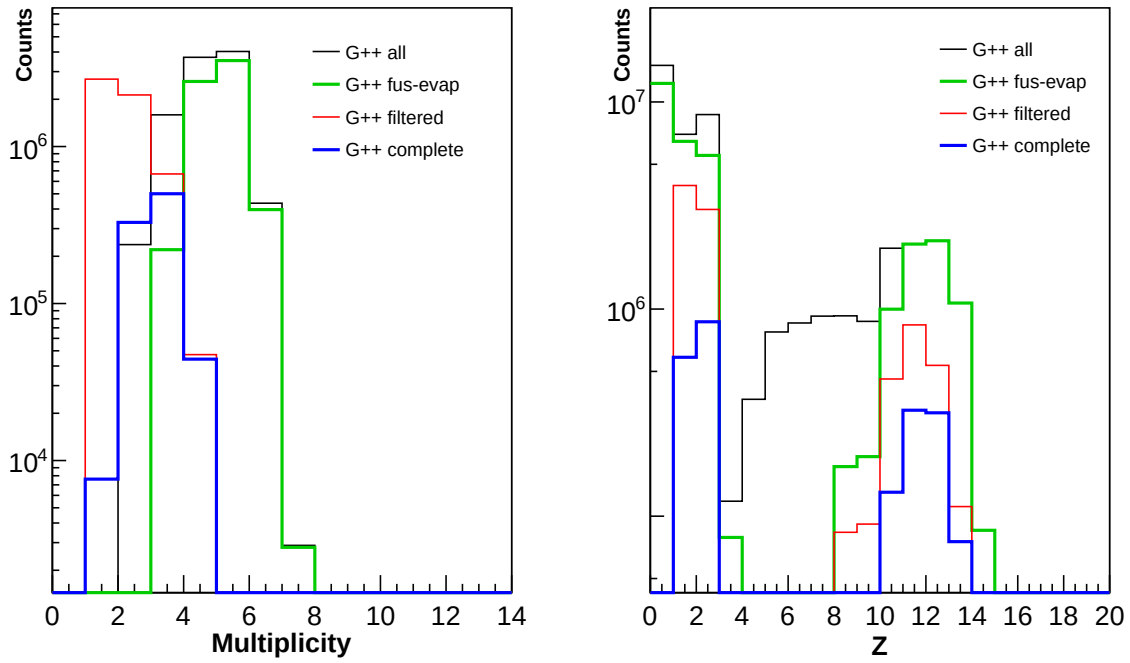

Figure 4.1: Multiplicity (left panel) and charge Z (right panel) comparison among the four different data sets of $^{18}O+^{12}C$ at 122 MeV. Labels in the legend, from top to bottom, correspond to: *G++ all events*, *G++ fus-evap events*, *G++ filtered fus-evap events* and *G++ complete events*.

Simulating GEMINI++ fusion-evaporation events characterized by the statistical decay of the excited CN, the awaited events multiplicity (left panel of Fig. 4.1) is at least 2 because there must be an evaporation residue (ER) in coincidence with an evaporated lighter particle. This is what we can observe in the *G++ all events* (black line) and *G++ fus-evap events* (green line) distributions. The multiplicity distributions show events emitting a residue in coincidences with one or more (max. 7) light particles. This is not the case with *G++ filtered fus-evap events* (red points) and *G++ complete events* (blue line). Here lower multiplicity values are observed. The reason for that shift can be found in the inefficiency in detecting particles when a GARFIELD+RCo-like geometrical filter is applied. In fact, neutral particles are not detected at all by the apparatus together with the particles that fall within the dead layers of the experimental array or

that do not exceed the detection thresholds. The inability to reveal neutrons reflects in the absence of $Z = 0$ in the charge distributions (as shown in right panel of Fig. 4.1). Furthermore, considering the *G++ complete events* (blue lines) where the total charge is reconstructed, multiplicity 1 corresponds to events where the only charged particle left is the Si ($Z = 14$). In coincidence with that residue, only neutrons can be emitted. Moreover, observing the multiplicity distribution of the *G++ fus-evap events* (green line), the minimum number of particles per events is 3; therefore, the presence of at least 2 neutrons can be inferred in the *G++ complete events* with a Si residue. As a consequence, since the number of neutrons per event cannot be inferred, a loss of information on event mass follows preventing a complete description of the reaction. Focusing on the charge distribution, the *G++ all events* (black line), providing both evaporative and fission-like events, shows a more populated shoulder of the residues bump ($Z = 3 - 7$) with respect to the other three data sets (green, red and blue lines). Such a region of charge is populated by fission-like events, where the two light fragments are produced. Those events can be found in the multiplicity distribution of the *G++ all events* (black line) with multiplicity = 2 instead of 3, as in the case of *G++ fus-evap events* (green line), where only events from evaporative decay are present. The charge distribution of the three data sets, where only the evaporative events are considered, have the same behavior, with an obvious decrease in yields when more selections are applied. A clear separation between the *Light Charged Particles*[6] ("LCP zone") and the ER bump is visible. The former corresponds to the evaporated hydrogen and helium nuclei, whereas the latter is associated with the residue remnant after the evaporation from the CN. It can be noticed that ER bump is coherent in shape whereas multiplicity is found at lower values due to the neutrons loss. In addition to this, the reduced statistics ($\sim 10\%$ of the total) due to all the applied selections does not allow a full reproduction of the whole Z spectrum.

In Fig. 4.2, the multiplicity and charge distributions normalized to the number of events are shown. Such a normalization allows us to highlight the difference in the relative yields of the simulated data under the different selections.

Further information can be obtained inspecting the 2D histogram which correlates charge Z and mass A of the fusion evaporation products. This plot is shown in Fig. 4.3. In the case of *G++ all events* (first panel from the top) the exotic hydrogen with $A = 4$ and $A = 5$ and the different isotopes of light fragments (Be, B) are visible. However, they disappear when the fusion-evaporation events are considered (other panels of Fig. 4.3). On the contrary, the isotopic distribution of the residue is conserved in the *G++ fus-evap events case* (second panel from the top), but it is not preserved after the filter (the two lower panels). However, the experimental filter does not affect the mass reconstruction of light charged particles. Comparing *G++ complete events* (last panel) with the *G++ fus-evap events* and *G++ filtered fus-evap events* (second and third panels from the top)

[6] In this thesis particles with $Z < 4$.

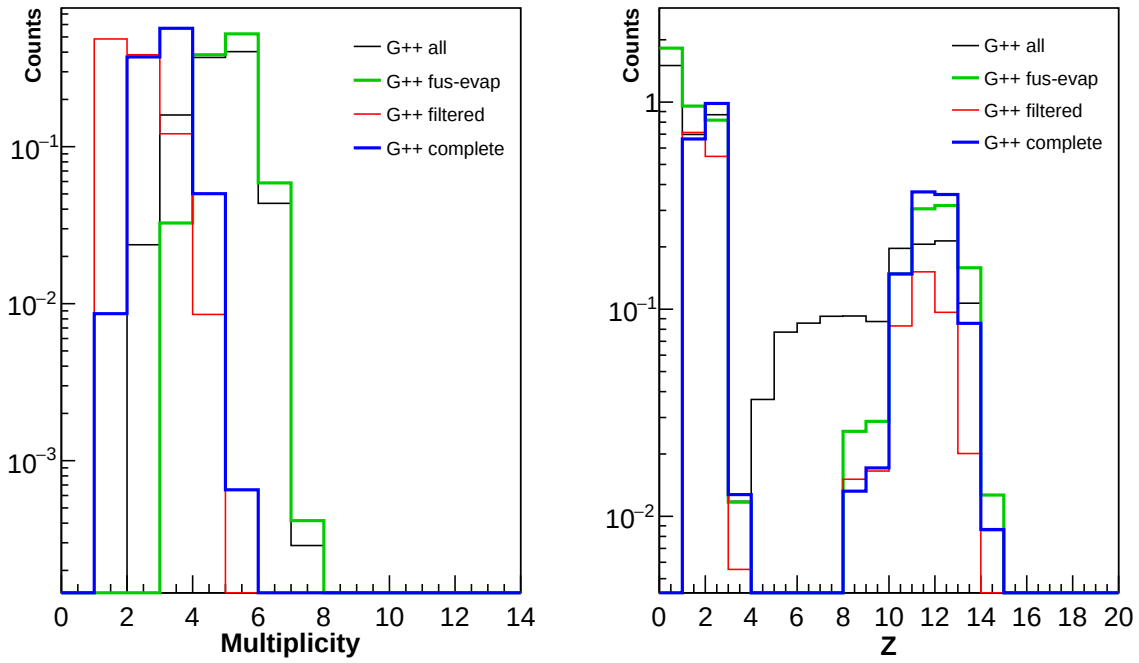

Figure 4.2: Same of Fig. 4.1, but the distributions are normalized to the number of events.

and focusing on the LCP yields, a clear increase in yields of the α particles is visible with respect to the proton yields.

Complementary information can be achieved looking at the correlation of charge vs. energy in the laboratory frame (E_{lab}) of the simulated particles for the 4 selection data sets shown in Fig. 4.4. Once again, the previous described effects on charge are obviously found. This correlation well highlights the influence of the energy threshold on the detection and reconstruction of the particles. Experimentally, this threshold corresponds to the fact that below a certain energy value (usually low channels) the particle identification cannot be performed. In the Z vs. E_{lab} plot, the effects of the energy threshold is reflected in a cut at low E_{lab}, which becomes more and more significant as Z increases.

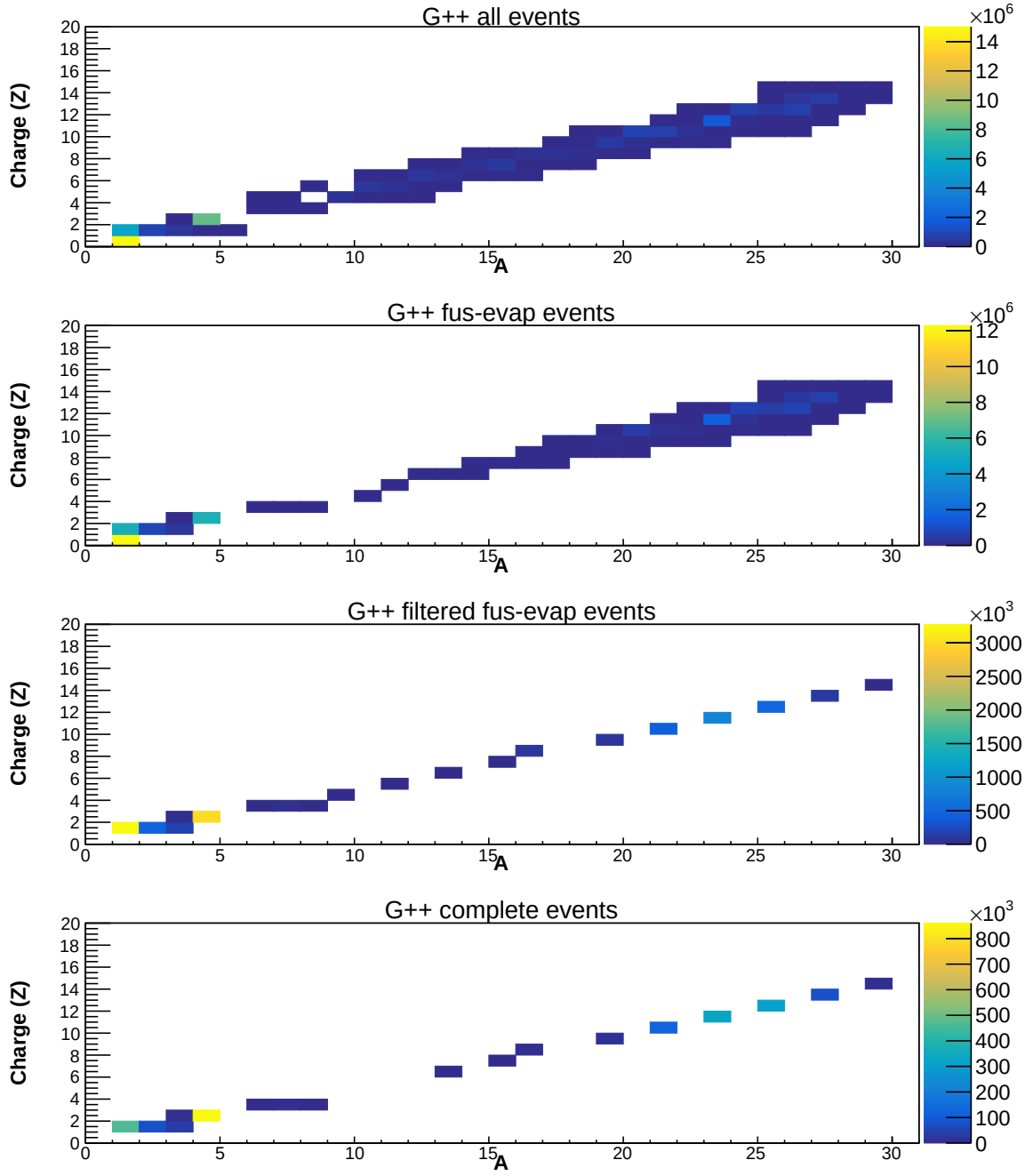

Figure 4.3: *Z vs A* correlations for the ^{18}O+^{12}C at 122 MeV simulated reaction. From upper to lower panel the four different data set selections are shown: *G++ all events*, *G++ fus-evap events*, *G++ filtered fus-evap events* and *G++ complete events*.

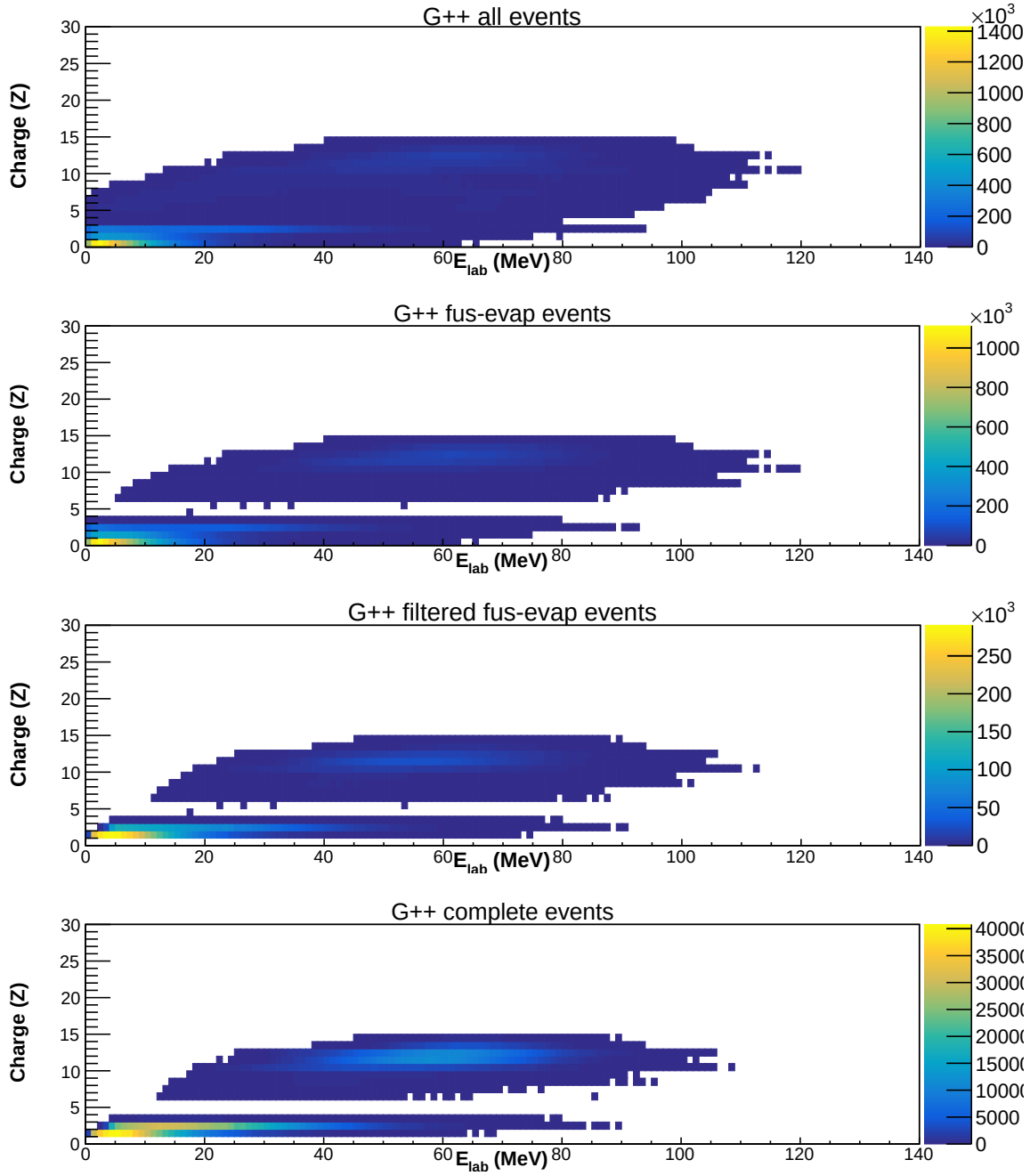

Figure 4.4: *Z vs* E_{lab} correlations for the $^{18}O+^{12}C$ at 122 MeV simulated reaction. From upper to lower panel the four different data set selections are shown: *G++ all events*, *G++ fus-evap events*, *G++ filtered fus-evap events* and *G++ complete events*.

Eventually, by exploiting the conservation law of the total charge and of the longitudinal momentum we can check the completeness of the events through the different selections observing the correlation between the total charge (Z/Z_{reac}) and the longitudinal momentum (q_z/q_{beam}). This correlation is shown in Fig. 4.5 for the four different data sets. The first two upper panels represent *G++ all events* (first from the top) and *G++ fus-evap events* (second). In both cases the conservation of total charge and of the longitudinal momentum is complete. Applying an experimental filter means losing particles. Clearly, each lost particle carries with it charge and momentum. Thus, the residual particles produce incomplete events having a lower total charge and a lower momentum. The third panel from the top shows this effects illustrating the Z/Z_{reac} vs. qz/q_{reac} plot for the case of the *G++ filtered fus-evap events*. Here a distribution in charge and momentum can be seen. Finally, imposing the charge conservation, the fourth selection is obtained: *G++ complete events*. Indeed, the lower panels of Fig. 4.5 show a single value of Z, as required by the imposed condition $Z_{tot} = 14$. On the other hand, the same plot shows the non conservation of the momentum. In fact, the distribution in the longitudinal momentum is mainly due to neutron escapes and to a lesser extent to uncertainty on the reconstruction of energy and thus of the momentum. Fig. 4.5 shows the "Z/Z_{reac} vs q_z/q_{beam}" correlation for the four different data sets.

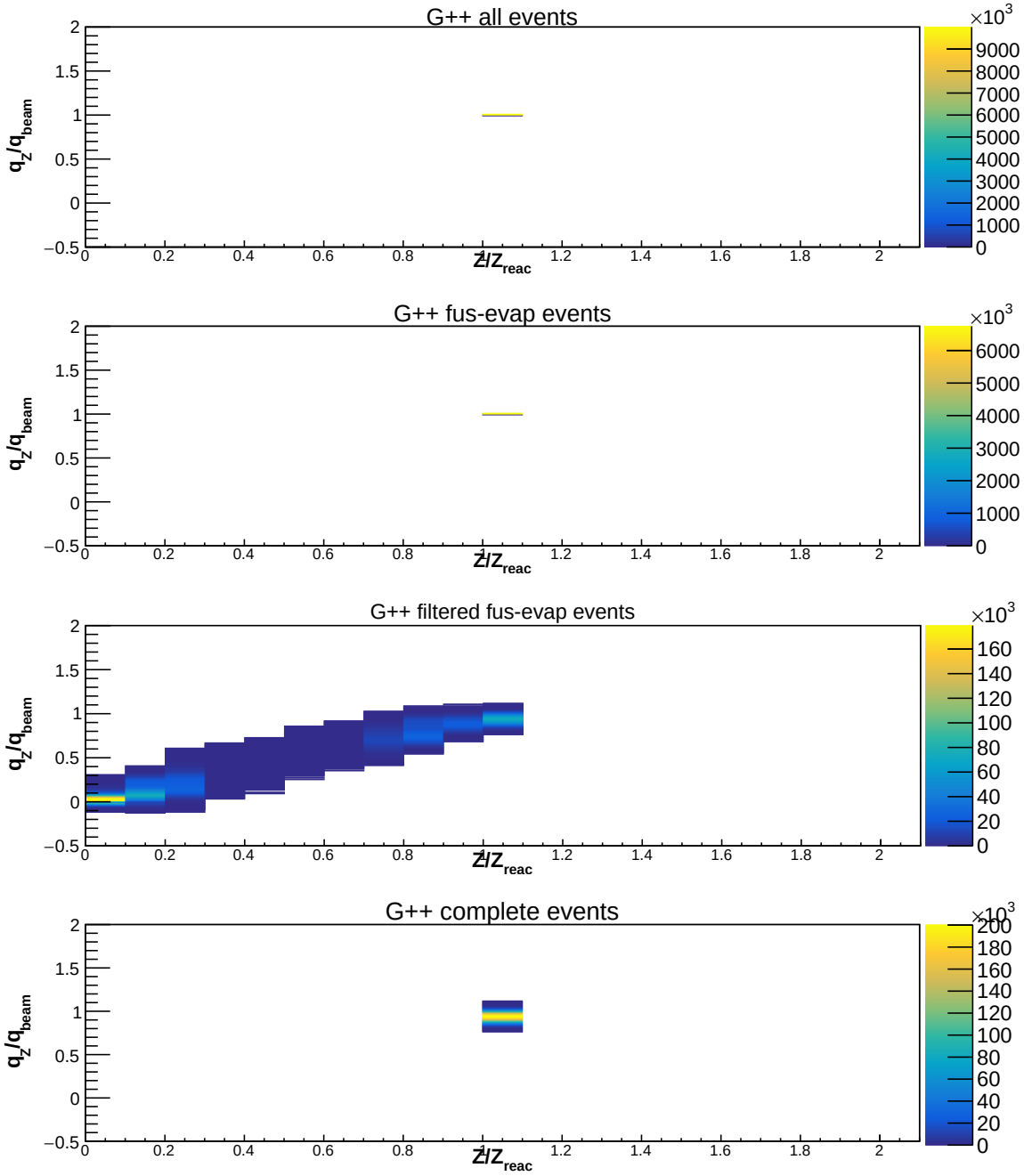

Figure 4.5: q_Z/q_{beam} *vs* Z/Z_{reac} correlations for the ^{18}O+^{12}C at 122 MeV simulated reaction. From upper to lower panel the four different data set selection are shown: *G++ all events*, *G++ fus-evap events*, *G++ filtered fus-evap events* and *G++ complete events*.

4.2.2 Single particle observables

In analogy with the previous section (Sec.4.2.1), only for the reaction $^{18}O+^{12}C$ at 122 MeV the single particle observables of interest are discussed here, with particular focus on proton and α-particle distributions. In Fig. 4.6, a comparison of the multiplicity is reported. As expected, the total yields of both α particles and protons decrease as more

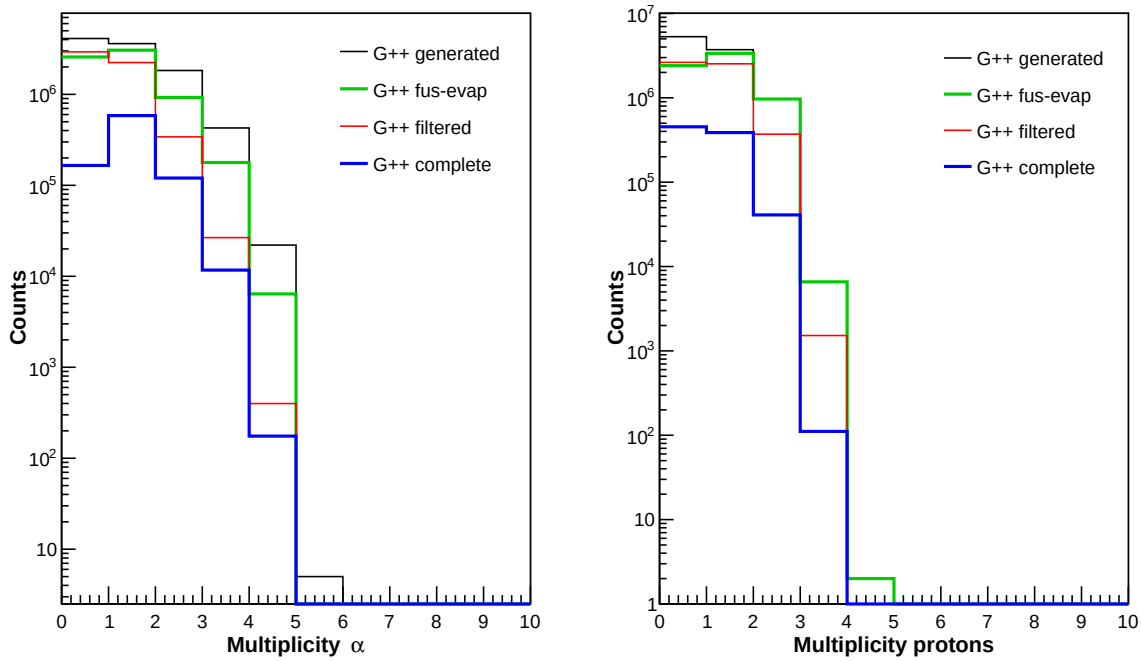

Figure 4.6: Comparison of α particles (left panel) and protons (right panel) multiplicity among the different data sets for the system $^{18}O+^{12}C$ at 122 MeV.

stringent selections are being considered reflecting the applied physical cut. The four data sets are again: the *G++ all events* (black line) including simulated events statistically produced via evaporation and fission-like decay; the *G++ fus-evap events* (green line) in which only the evaporative decay events are taken into account; the *G++ filtered fus-evap events* (red line) and *G++ complete events* (blue line) where the experimental filter, simulating the detecting apparatus conditiong, is imposed to the simulated data. The former includes all the incomplete events passing through the filter, while the latter includes only those events that conserve the total charge number. In particular, it is noteworthy to highlight the meaning of the multiplicity = 0: it is the number of events without the particle under study, therefore it gives an idea of how many α particles or protons are lost in a specific selection. Considering specifically the *G++ complete events* case, we can observe that the 0−multiplicity for α particles decreases more than in the

other multiplicity cases, while for protons the decrease of the 0−multiplicity is similar to those of other multiplicity. This means that more protons are lost with respect to the α-particles in the *G++ complete events*.

In Fig. 4.7 and Fig. 4.8 the energy spectra in the center of mass are reported for α particles and for protons, respectively. In the left panels of both figures the comparison

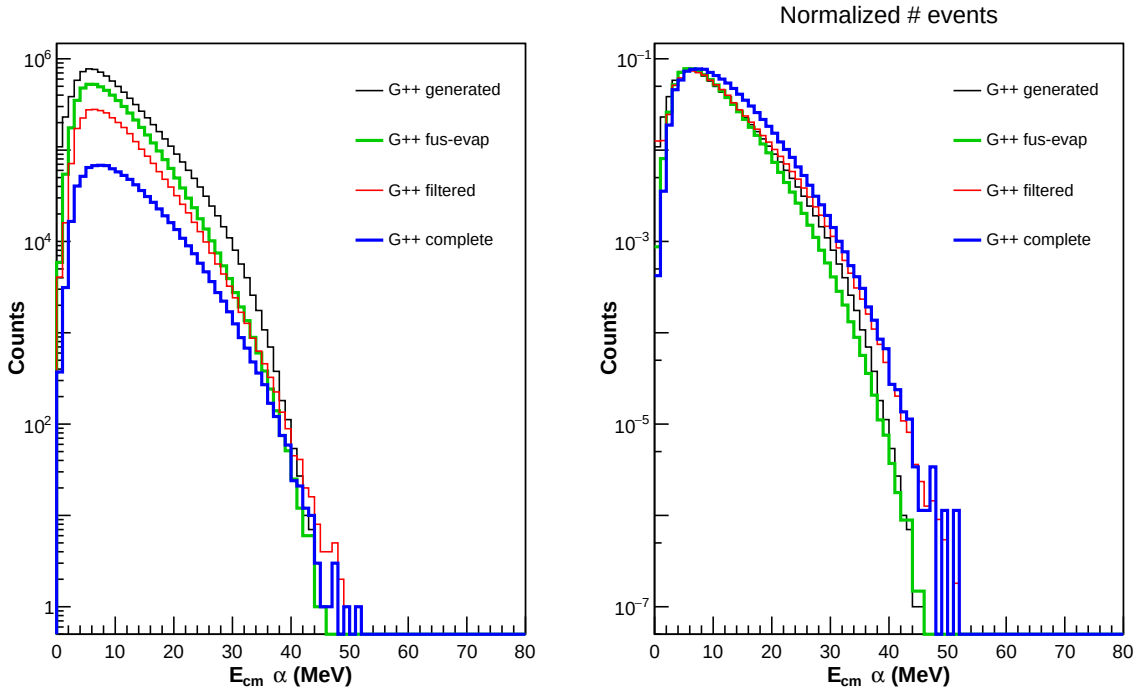

Figure 4.7: Left panel: α particles E_{cm} comparison among the different data sets for the $^{18}O+^{12}C$ at 122 MeV system. Right panel: same as in the left panel, but the energy spectra are normalized to the number of events.

among the four data sets are shown without any normalization to highlight the loss of particles in particular regions of the energy spectra. On the other hand, in the right panels of the same figures the spectra are normalized to number of events in order to compare the relative loss of particles as a function of the energy. In this latter case also a shape comparison of the spectra is visible.

Comparing the α-particles spectra of the *G++ all events* (black line) and of the *G++ fus-evap events* (green line) shown in Fig. 4.7, the differences beetween them are ascribable to particles emitted in the former case following a fission-like event. The result is a more accentuated rounded shape (around $20 - 30$ MeV) of the former with respect to the latter. On the other hand, comparing the *G++ fus-evap events* (green line) with the *G++ filtered fus-evap events* (red line) and with the *G++ complete events* (blu line),

we can assert that the experimental filter and also the complete event selections affect mainly the low energetic α particles. Indeed, a decrease in yields in the energy region of the peaks is visible as a more selecting condition is imposed. On the contrary, the energy tails do not vary among the three data sets. Consequently, the events left after all the selections (i.e. complete events) are characterized on average by more energetic α particles. Accordingly, this is not ascribable to an overproduction of more energetic events, but to the loss of lower energy channels due to the selections. Otherwise, the protons energy spectra feature a similar lowering of yields on the whole spectrum which is dependent on the specific selection applied to the data set, as shown in Fig. 4.8.

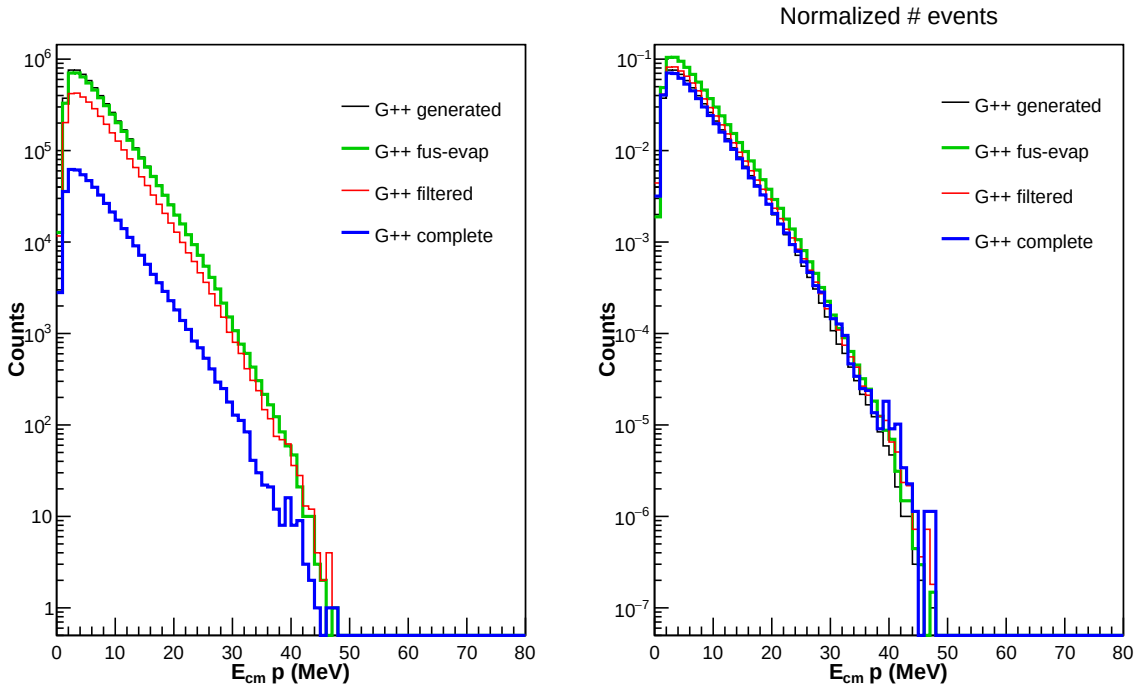

Figure 4.8: Left panel: protons E_{cm} comparison among the different data sets for the $^{18}O+^{12}C$ at 122 MeV system. Right panel: same as the left panel, but the energy spectra are normalized to the number of events.

In order to better understand where the selection mainly influences the proton and α-particle spectra, in Fig. 4.9 and in Fig. 4.10 the α-particle and the proton energy spectra are, respectively, shown in the three angular regions:

- Garfield Bckward (GB): $97.5° \div 150.4°$
- Garfield Forward (GF): $29.5° \div 82.5°$

- Ring Counter (RCo): $5° \div 17°$

for the four data sets. The first column represents the yields resulting from the subsequent selections, while in the second a unitary area normalization is applied to better compare the spectral shape. In the upper panels of Fig. 4.9, the energy spectra of α particles in GB are shown. A significant energy threshold is visible when the experimental filter is applied. This threshold is a consequence of the absence of reading electronics in the MSGC of GB. Hence, the α particles exceeding the filter cuts are the more energetic ones at backward angles. In the GF angular region, most part of the particle yields is collected; therefore, this is the angular region which mainly influence the total spectrum. Indeed, the behavior of the α particles spectra in GF is analogue to that of the total spectrum. In the RCo region the loss in α particle yields is homogeneous on the whole energy range; in fact the energy shape is the same for the different data sets. However, it is noteworthy to underline the presence of a peak at very low energies for the *G++ complete events* (black line). This peak is ascribable to quasi-fission mechanisms, therefore it is not visible after the selection of the heavy residue. Similar considerations can be done for the three angular region proton energy spectra reported in Fig. 4.10. In GB (upper panels), a threshold is present also for the protons, but it has a lower magnitude than for α-particles and it does not affect the proton energy shape (see upper right panel). In GF a slightly higher tail of protons spectra is observed. Otherwise a lower tail is shown for the RCo angular region.

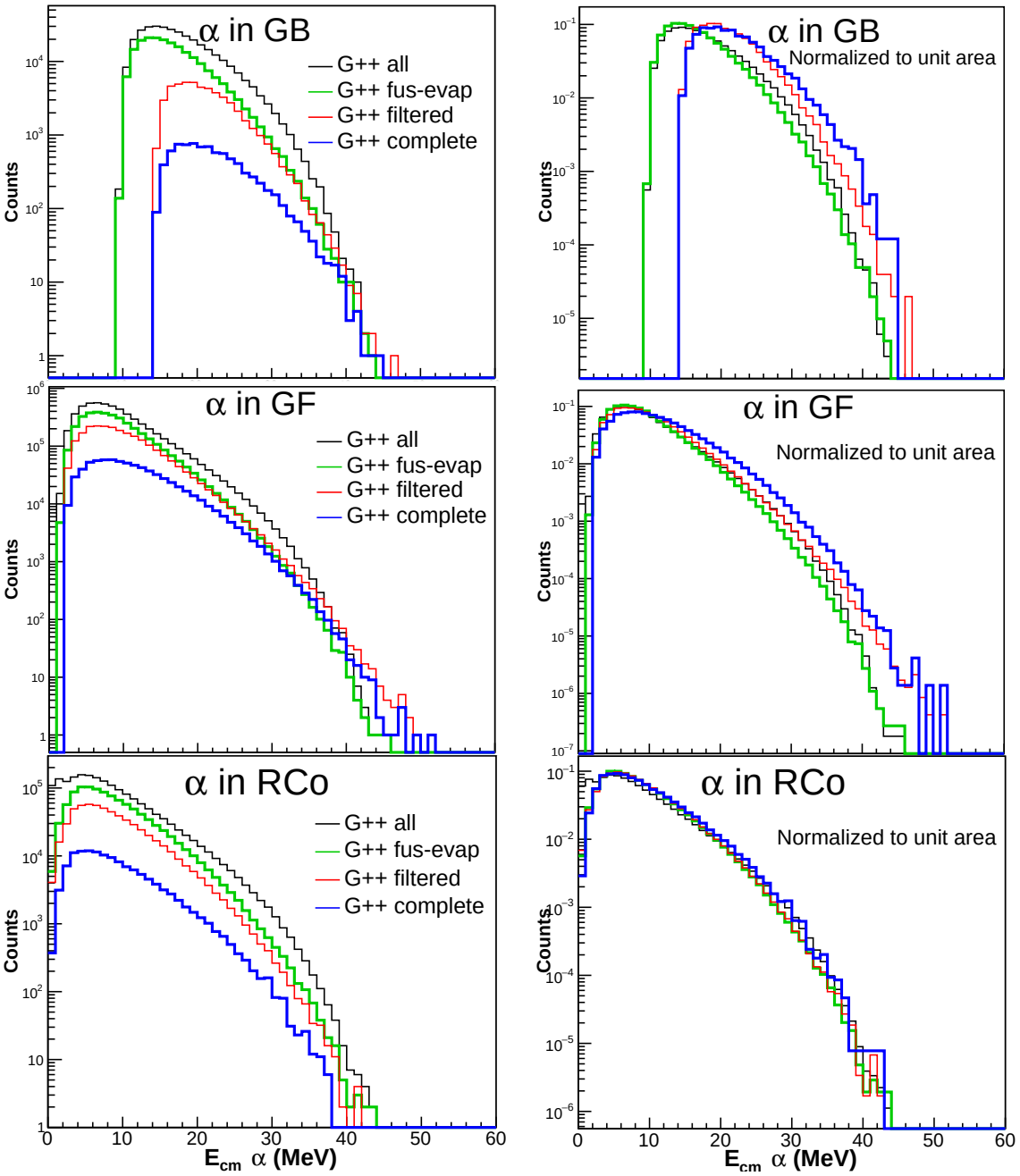

Figure 4.9: α-particle energy spectra in the three angular region: GARFIELD forward (upper panels), GARFIELD backward (central panels) and Ring Counter (lower panels) for the four data selections. The first column shows the yields reduction due to the subsequential selections, while in the second column the spectra are normalized to the unitary area.

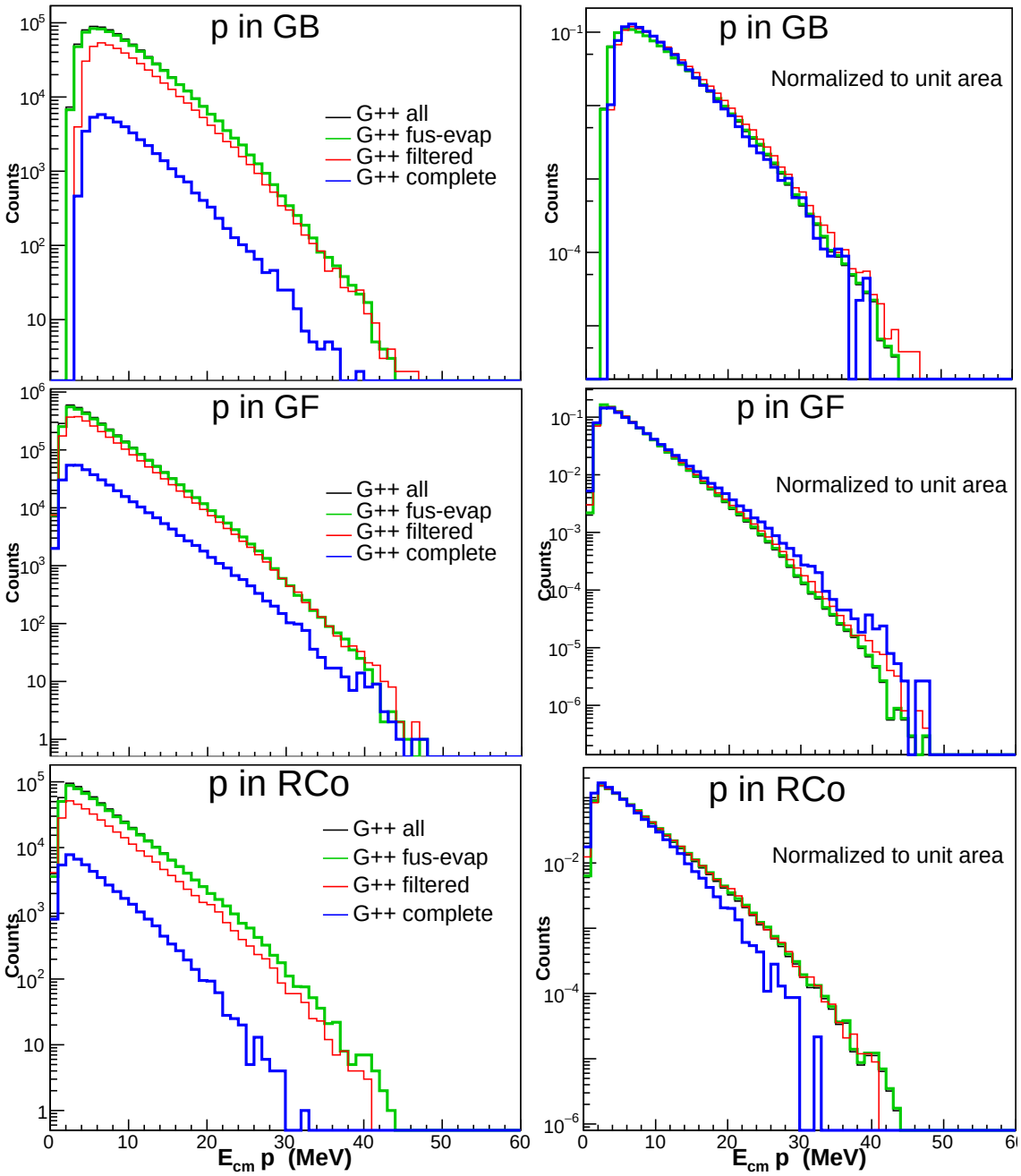

Figure 4.10: Same of Fig. 4.9, but for protons.

In Fig. 4.11 a comparison of the polar angle distributions of the α particles among the four data sets is reported. The distribution in the plot are normalized to the solid

angle and to the number of events in order to understand how the different selections affect the kinematics of the reaction.

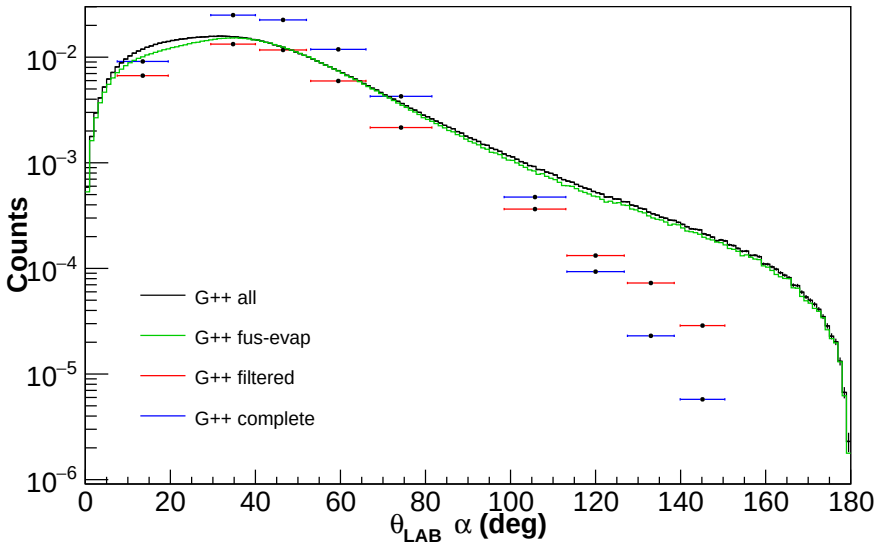

Figure 4.11: Comparison of α-particles polar angular distribution θ_{Lab} in laboratory reference system among the four different data sets for the $^{18}O+^{12}C$ reaction at 122 MeV normalized to the number of events and to the solid angles. The error bars stands for the semi range between θ_{min} and θ_{max} of each Cs # and RCo.

The rounded shape of the *G++ all events* suggests that when also fission-like events are included, the reaction mechanism is more projected at forward angles with respect to only fusion-evaporation processes (green curve, blue and red points). *G++ filtered fus-evap events* (red line) conserve the shape of the *G++ fus-evap events* (green line) data set approximately in the GARFIELD forward angular region ($29.5° \div 82.5°$). At lower and higher angles, the agreement is lost. Considering the *G++ complete events* after all the selections, in the RCo angular region (the point at angle lower than 20°) it seems to be in agreement with the *G++ fus-evap events* (green line). Otherwise, this agreement disappear in the GARFIELD regions. It is important to notice: firstly that in the RCo three detection stage are present IC, Si and CsI (all sensible to α particles), in the forward chamber of GARFIELD two detection stages are present, namely the MSGC and CsI(Tl) crystals, whereas in the backward chamber only CsI(Tl) are operational. This means that the apparatus is more efficient in detecting these kind of events at lower angles. Secondly, it is important to point out that the *G++ filtered fus-evap events* (red line) distributions are obtained from averaged points on the angular coverage of the single number j (5, 6, 7, 8) of CsI(Tl) crystal.

Fig. 4.12 shows the same distributions for the protons. One of the most noticeable

peculiarities of this plot is the gap between the *G++ all events* and the *G++ fus-evap events* distribution. Selecting only the fusion-evaporation events, the channels with a higher probability of protons emission are selected. This can be inferred recalling right panel in Fig. 4.6, showing a higher relative yield of 0 proton multiplicity for *G++ all events* with respect to the *G++ fus-evap events* being the number of events the same.

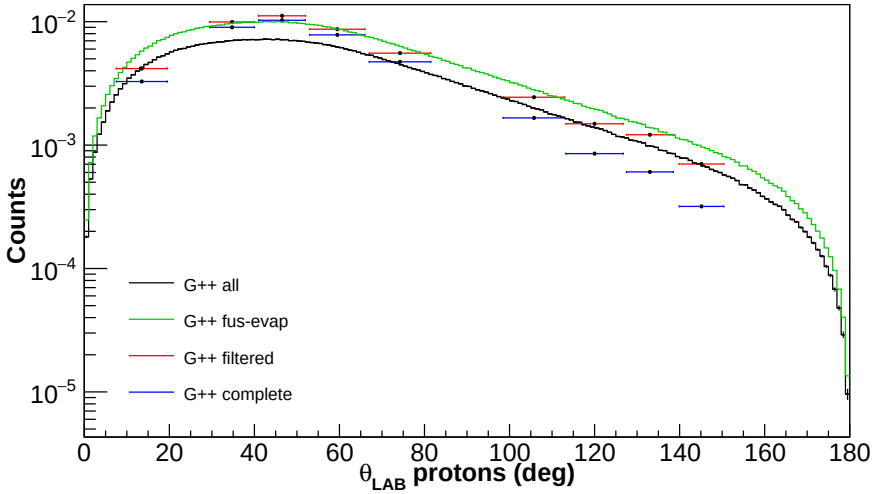

Figure 4.12: Same as Fig. 4.11, but for protons.

4.3 Comparison of the 3 reactions at 112.5, 122 and 300 MeV

To evaluate how the fusion-evaporation mechanism changes according to the compound nucleus formed in the reaction and to its excitation energy, the same distributions described in Sec.4.2 for the single 122 MeV reaction are presented for the three studied reactions: ^{18}O+^{13}C at 112.5 MeV and ^{18}O+^{12}C at 122 and 300 MeV. The GEMINI++ statistical-decay code was used to generate the MC data samples (10^7 events) for each system. In particular, in order to compare the evaporation products from the three reactions, only *G++ fus-evap events* and *G++ complete events* data sets are considered. Within this analysis it is worth underlying that:

- ^{18}O+^{13}C at 112.5 MeV and ^{18}O+^{12}C at 122 MeV reactions share the same excitation energy of the CN: ^{30}Si* and ^{31}Si*, respectively. The only difference lies in the different number of neutrons;
- ^{18}O+^{12}C at 122 and 300 MeV reactions produce the same CN (^{30}Si*) differing in excitation energy.

In the following, the different reactions are represented with the following color legend:

- fuchsia line for ^{18}O+^{13}C at 112.5 MeV;
- cyan line for ^{18}O+^{12}C at 122 MeV;
- orange line for ^{18}O+^{12}C at 300 MeV.

In the left panel of Fig. 4.13, the total multiplicity distributions for the *G++ fus-evap events* data sets are shown. As the CN excitation energy increases, the multiplicity of particles per event becomes higher. This feature becomes more evident when comparing reactions with considerably different energies, like for example 300 MeV (orange line) and 112.5 MeV (fuchsia line) reactions. The emission of more particles per event is reflected in charge distribution where the residue bump is shifted to lower values of Z, as visible in the right panel of Fig. 4.13. The larger is the number of evaporated particles, the lower is the residual charge. In the cases of the 112.5 MeV (fuchsia line) and 122 MeV (cyan line) reactions, events with $Z = 14$ are present in the distributions. This means that the CN de-excites by emitting only neutrons. For the other system, instead, this residue is not visible: the excitation energy of CN is much higher and de-excitation occurs through the emission of more massive particles. While the three reactions show a similar fraction of neutron production ($Z = 0$), they differ in protons ($Z = 1$) and α-particles ($Z = 2$) relative yields. For instance, the 112.5 MeV reaction (fuchsia) is characterized by a lower production of protons than α-particles, whereas for the other two reactions these are similar.

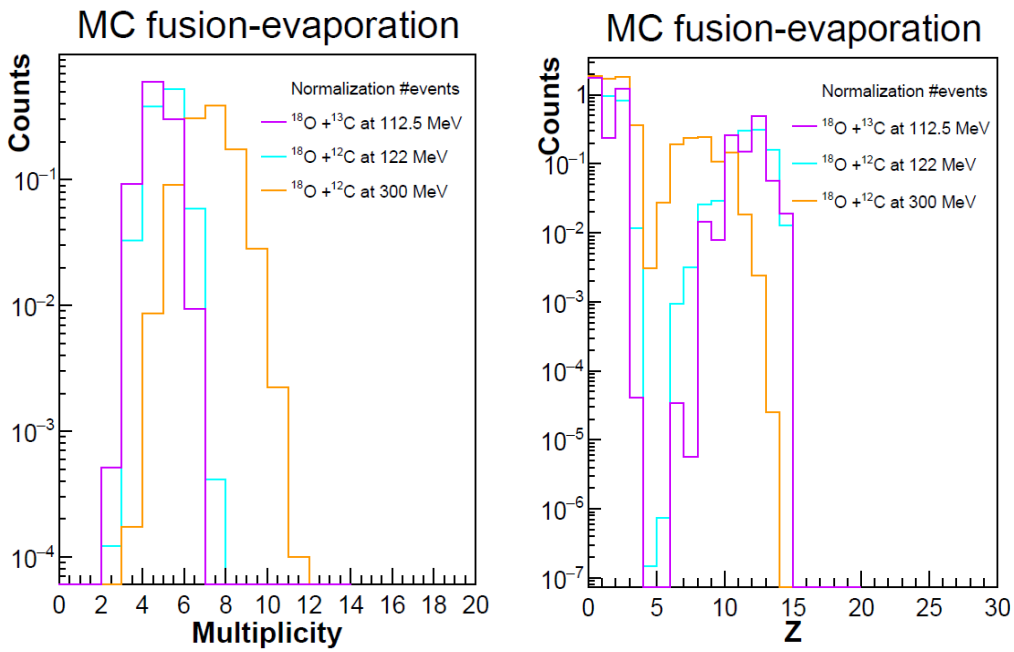

Figure 4.13: Multiplicity (left panel) and charge Z (right panel) distributions of MC fusion-evaporation among the three different reactions: ^{18}O+^{13}C at 112.5 MeV (fuchsia) and ^{18}O+^{12}C at 122 (cyan) and 300 MeV (orange). The distributions are normalized to the number of events.

At 112.5 MeV, fewer protons are produced with respect to the α particles, whereas for the other two reactions these are similar. Therefore, the different production of protons can be related to the mass of the CN. The *G++ complete events* show the same behaviour in terms of multiplicity and charge of the three reactions described for the *G++ fus-evap events*. This means that, regardless of the applied conditions, the general trends of variables are conserved even though heavier Z values (for instance $Z = 13$) show a more relevant reduction than lower values.

In the right panel of Fig. 4.13 with the $Z = 1$ and $Z = 2$ labels we refer only to protons and α-particles, respectively. This can be explained by inspecting the charge vs mass correlation of the three reactions, shown in Fig. 4.14. Indeed, protons and α-particles are the most produced particles in the reaction at 112.5 MeV (upper panels) and this peculiarity is also found when increasing the energy of the reaction. In addition to this, a striking increase in the deuterons production is observed in the ^{18}O+^{12}C at 300 MeV system. The same is awaited also after applying the experimental filter to the data samples (second column).

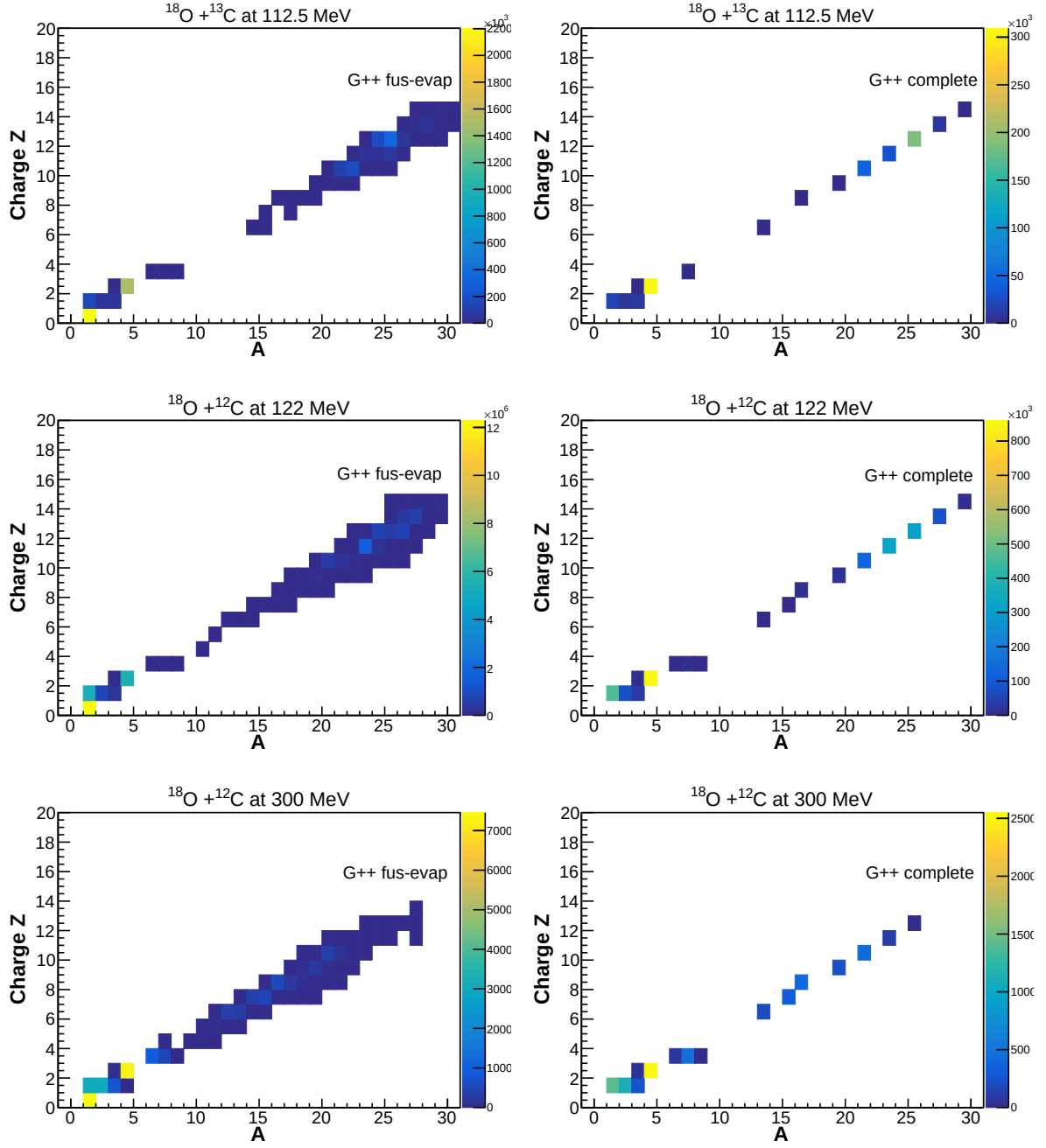

Figure 4.14: Charge and mass correlation for the three different reactions: ^{18}O+^{13}C at 112.5 MeV (first row) and ^{18}O+^{12}C at 122 (second row) and 300 MeV (third row). Left panels: *G++ fus-evap events*. Right panels: *G++ complete events*.

In Fig. 4.15, the α-particle multiplicity distributions for the two data sets in the three reactions cases are represented. Here again, an increase in multiplicity is found at higher

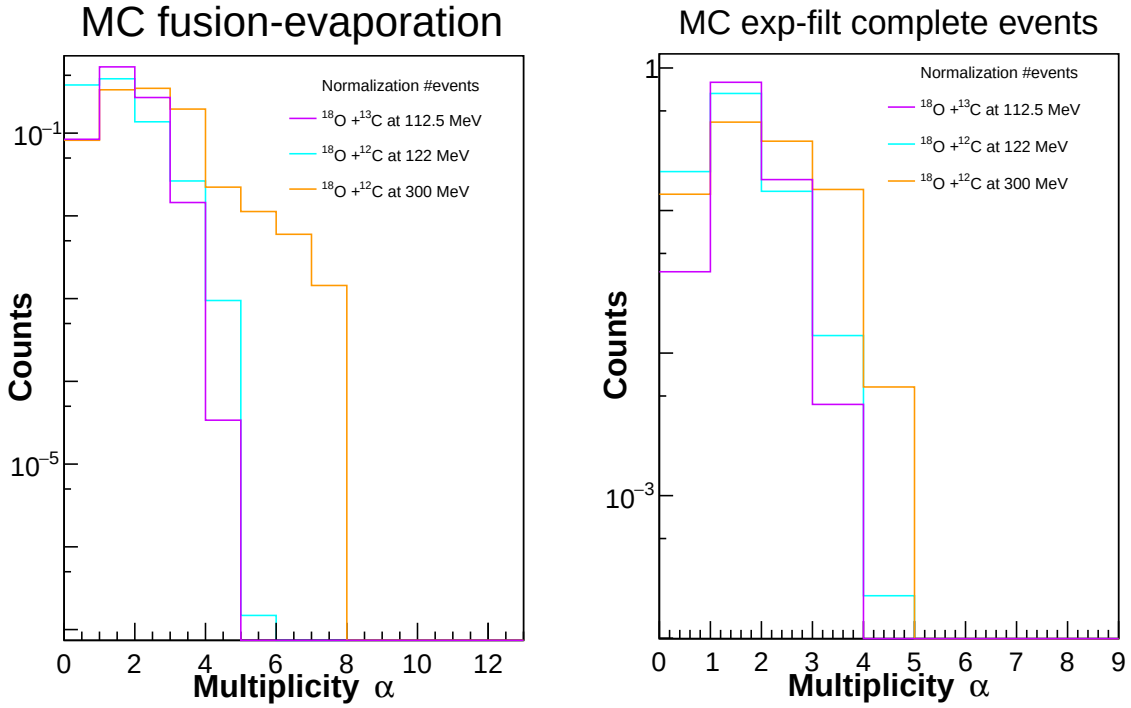

Figure 4.15: Comparison of α particles multiplicity among the three different reactions: ^{18}O+^{13}C at 112.5 MeV (fuchsia) and ^{18}O+^{12}C at 122 (cyan) and 300 MeV (orange). Left panel: MC fusion-evaporation events. Right panel: MC experimentally filtered complete events.

excitation energies especially in the case of the *G++ fus-evap events*. This distribution is important because in the case future analyses highlight discrepancies between the MC simulations and the experimental data, this might hint at the presence of α-cluster structure effects. Obviously this effect is only one of the many to be analyzed before asserting that a signature of the clusterization is seen.

It is noteworthy to underline that when comparing the *G++ complete events* with the *G++ fus-evap events*, the most energetic reaction does not feature an increase in multiplicity $= 4 \div 8$ any longer. In other words, in *G++ complete events* the difference among the three reactions is not so striking. However, the orange distribution shows an increment in channels with no α particles compared to *G++ fus-evap events*.

Fig. 4.16 illustrates the energy spectra of α particles referred to the three different cases for the *G++ complete events* and for the *G++ fus-evap events*. The energy value on which the peak of the distribution falls depends on the formed CN. Therefore, a difference in the neutron content of the system causes a rise of the Coulomb barrier

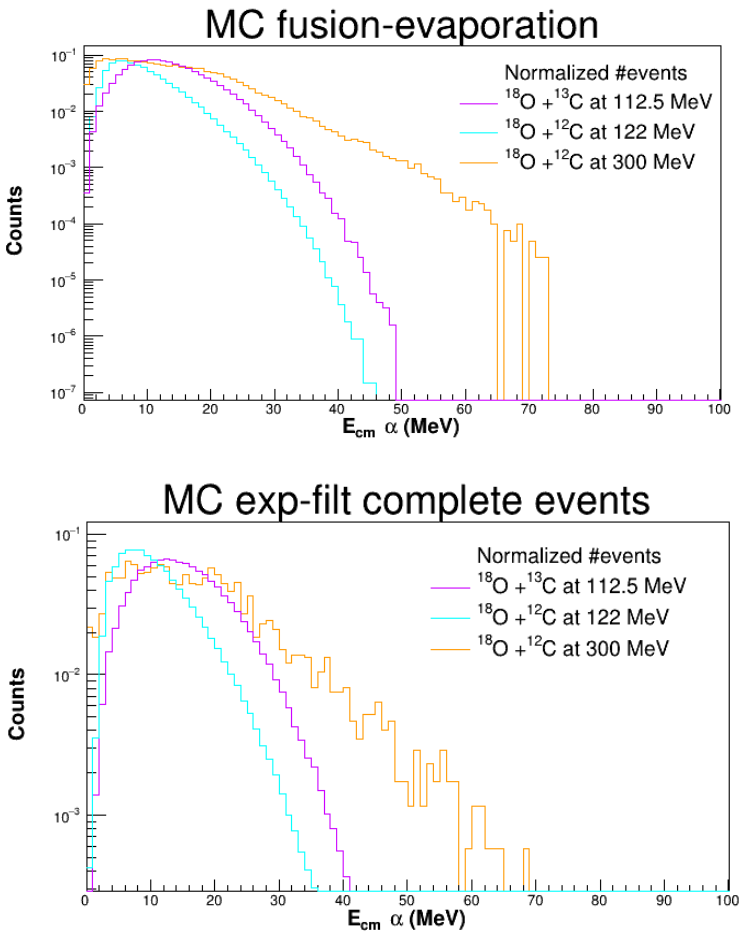

Figure 4.16: Comparison of α-particle energy spectra in the center of mass reference frame among the three different reactions: ^{18}O+^{13}C at 112.5 MeV (fuchsia) and ^{18}O+^{12}C at 122 (cyan) and 300 MeV (orange). Upper panel: MC fusion-evaporation events. Lower panel: MC experimentally filtered complete events.

resulting in a shift of the distribution peak. This is what is observed in the reaction ^{18}O+^{13}C at 112.5 MeV (fuchsia line). On the other hand, the tails slope is an index of the excitation energy. Having ^{18}O+^{13}C at 112.5 MeV (fuchsia) and ^{18}O+^{12}C at 122 (cyan) the same excitation energy, their slope in the α-particle energy spectra is the same ($25 \div 30$ MeV). On the contrary, the reaction at 300 MeV (orange line) shows a less accentuated slope suggesting that the emitted particles are more energetic. The

compound nucleus is the same, but more excited than the one of the reaction $^{18}O+^{12}C$ at 122 MeV.

As far as protons are concerned, reactions with the same CN, $^{18}O+^{12}C$ at 122 and 300 MeV, show a similar distribution in proton multiplicity in Fig. 4.17. Thus, the proton emission depends more on the CN than on the excitation energy. Indeed, the $^{18}O+^{13}C$ at 112.5 MeV features a difference in the relative yield for multiplicity 0.

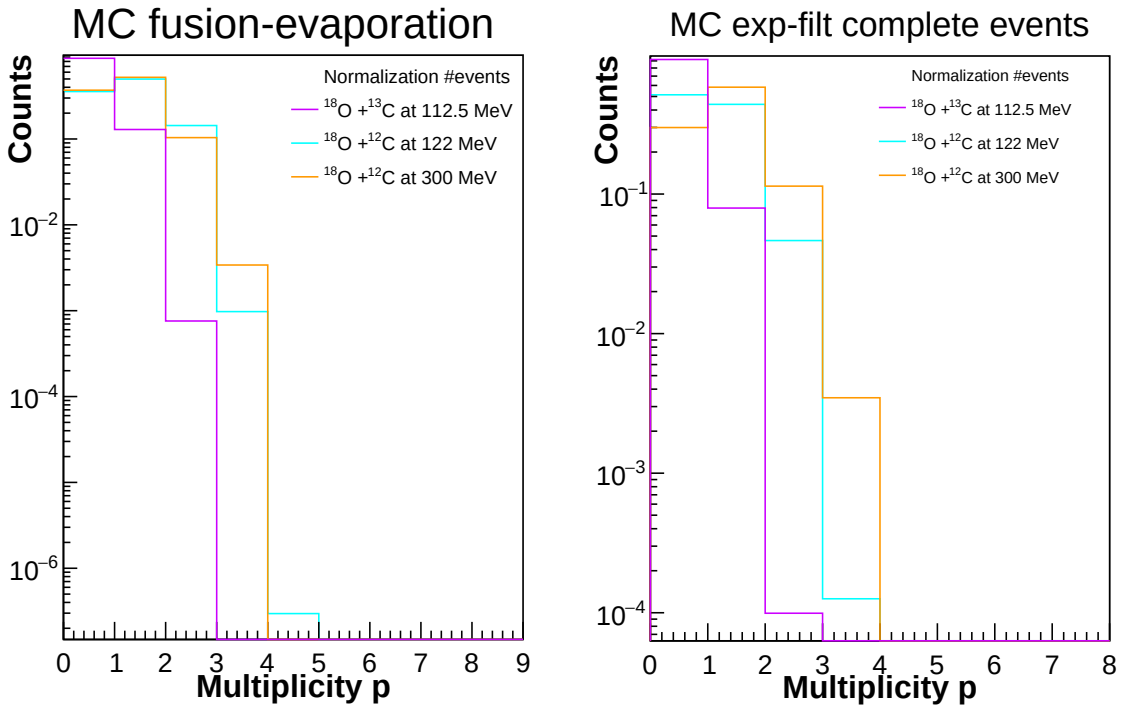

Figure 4.17: Comparison of protons multiplicity among the three different reactions: $^{18}O+^{13}C$ at 112.5 MeV (fuchsia) and $^{18}O+^{12}C$ at 122 (cyan) and 300 MeV (orange). Left panel: *G++ fus-evap events*. Right panel: *G++ complete events*.

The same consideration-particle done before for the α distributions are valid for the proton energy spectra in Fig. 4.18. In this case, the normalization to the unit area of the distribution is also reported (second column) since, unlike with α particles, a comparison in terms of shape is not possible. In the upper panels the distributions are normalized to the number of events, while a normalization to the unit area is shown in lower panels. By applying the complete event data selection, the global features of the energy spectra characterizing the three reactions are conserved.

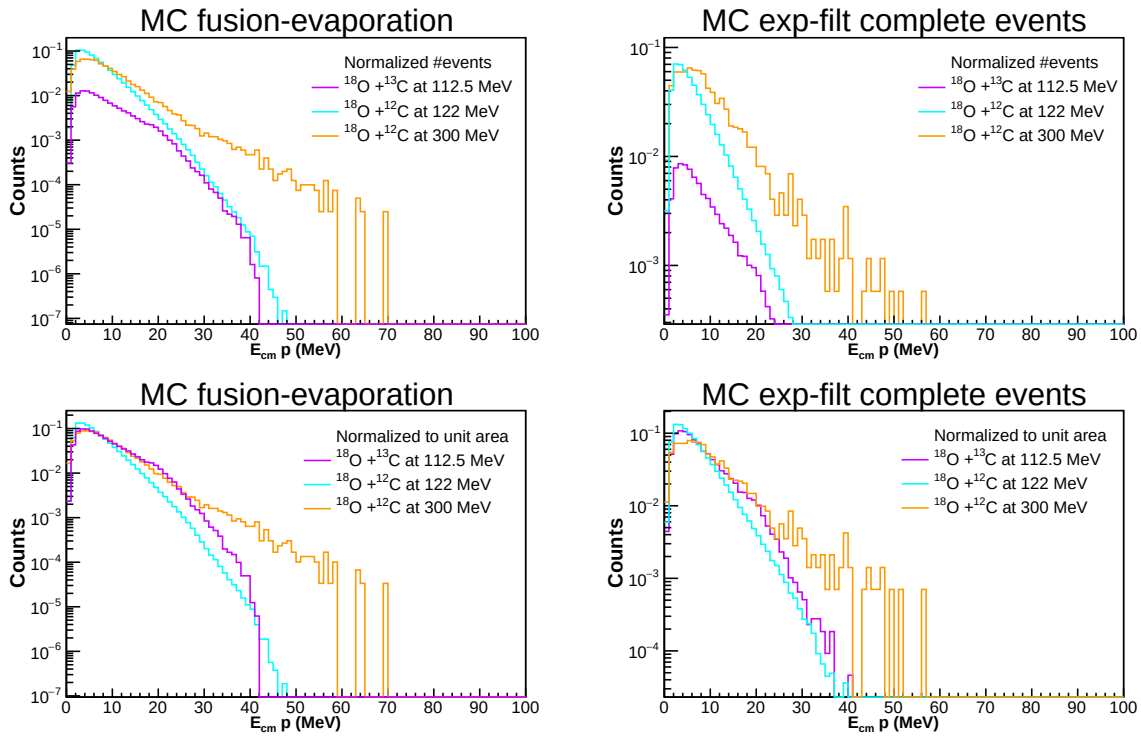

Figure 4.18: Comparison of protons multiplicity among the three different reactions: ^{18}O+^{13}C at 112.5 MeV (fuchsia) and ^{18}O+^{12}C at 122 (cyan) and 300 MeV (orange). Left panel: *G++ fus-evap events*. Right panel: *G++ complete events*.

Finally, Fig. 4.19 reports the comparison of the α-particle angular distributions of the three reactions: ^{18}O+^{13}C at 112.5 MeV (fuchsia) and ^{18}O+^{12}C at 122 (cyan) and 300 MeV (orange) in the case of the *G++ fus-evap events* (upper panel) and in the case of the *G++ complete events* (lower panel).

The three distributions are normalized to the number of events and to the solid angle and are presented in the laboratory reference frame in order to highlight the possible detection yields in the different regions of the experimental array. For the case of *G++ fus-evap events* (upper panel) the three reactions show three different behaviors due to the different opened decay channels. Notice that at forward angles (lower than 25°) the emission of α particles increase in both ^{18}O+^{12}C at 300 MeV (orange line) and ^{18}O+^{13}C at 112.5 MeV (fuchsia line) compared to the ^{18}O+^{12}C at 122 MeV (cyan line). This means that the increase in forwarded α particles can be related both to the higher energy and to the isotopical difference between the hot sources. A similar trend is also found for backward angles. Concerning the *G++ complete events* (lower panel), the three distributions reflect the same behavior in the forward angular region which is not the case in the backward.

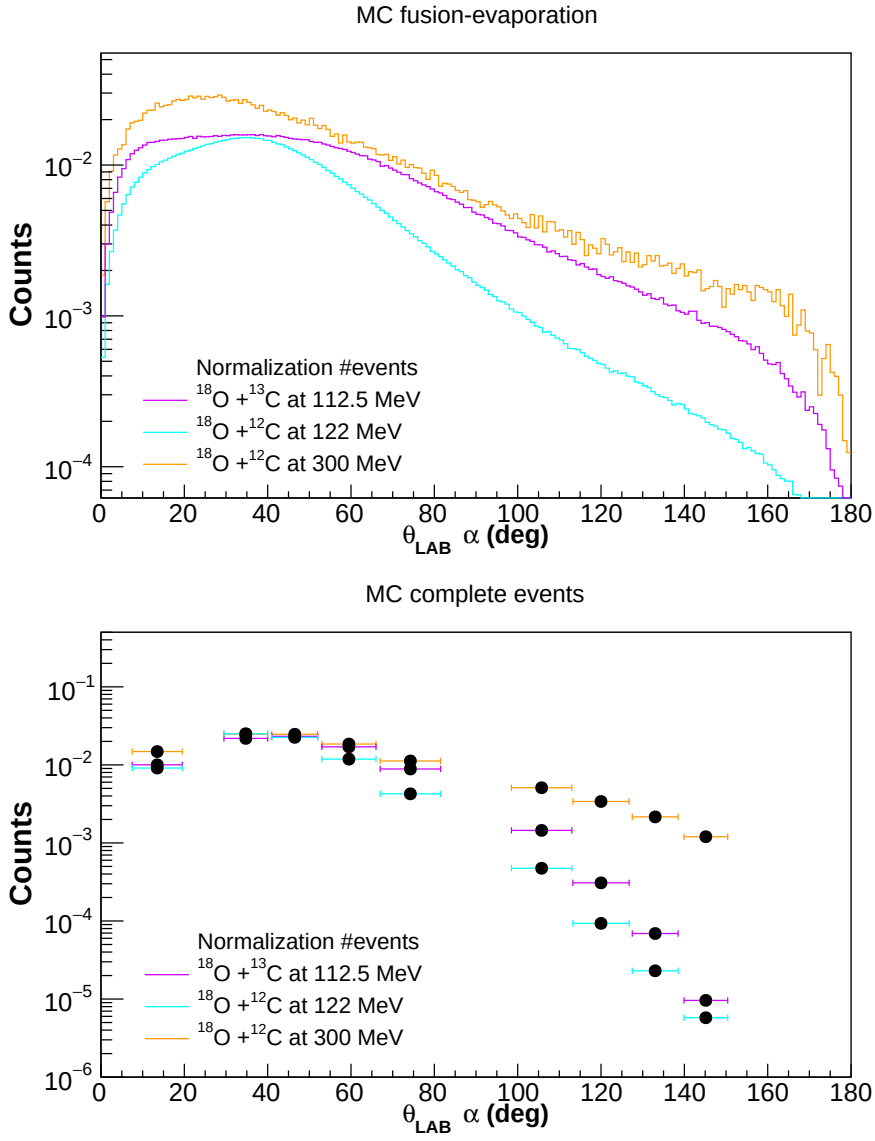

Figure 4.19: Comparison of α-particle polar angle distribution in the laboratory frame among the three different reactions: ^{18}O+^{13}C at 112.5 MeV (fuchsia) and ^{18}O+^{12}C at 122 (cyan) and 300 MeV (orange). Upper panel: *G++ fus-evap events*. Lower panel: *G++ complete events*.

Regarding the proton angular distributions (Fig. 4.20), the same shape is found for the reactions referring to the same CN (cyan and orange lines). The complete events selection causes a larger loss in the yields for the reaction at 122 MeV compared to the one at 300 MeV. This explains the gap between the ^{18}O+^{12}C at 122 (cyan) and 300 MeV (orange) reactions in the lower panel of Fig. 4.20.

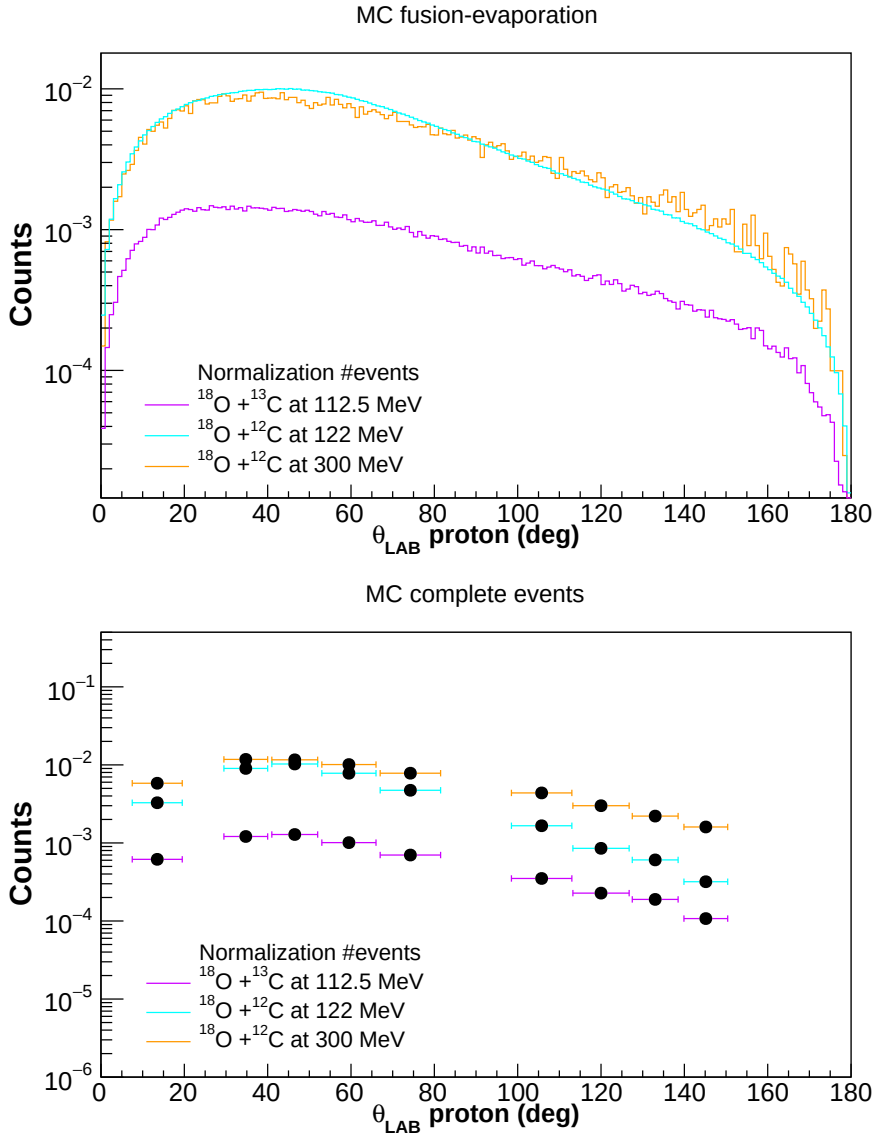

Figure 4.20: Comparison of protons polar angle distribution in the laboratory frame among the three different reactions: ^{18}O+^{13}C at 112.5 MeV (fuchsia) and ^{18}O+^{12}C at 122 (cyan) and 300 MeV (orange). Upper panel: *G++ fus-evap events*. Lower panel: *G++ complete events*.

4.4 Comparison between GEMINI++ and HFℓ

Both the GEMINI++ and HFℓ codes describe the evaporation decay from a CN. In addition to this, HFℓ provides a more accurate description of the known discrete levels for lighter nuclei being the pairing interaction considered. Hereafter, the comparison of those simulation codes is presented for the ^{18}O+^{12}C reaction at 122 MeV. Special attention is paid to *fusion-evaporation events* and *complete events* data sets. The first ones represent the data set of fusion evaporation events generated by the two Monte Carlo simulation codes. The second ones, instead, represent the same physical events, completely reconstructed in terms of charge, but filtered via the apparatus geometry. The comparison of the same physical events before and after filtering through the apparatus is of fundamental importance in order to understand the sensitivity of the detection apparatus to the various statistical models. The expected result is a minimal difference between GEMINI++ and HFℓ attributable to their different processing of excited discrete levels of nuclei and to a different parametrization of transmission coefficients.

In Fig. 4.21, multiplicity and charge distributions for *fusion-evaporation events* and *complete events* generated by the two simulation codes are reported. Both codes generate similar trends in the distributions even if GEMINI++ shows a larger yield in lower multiplicity channels. If *fusion evaporation events* are considered, the more accurate nuclear levels description obtained with HFℓ provides a further insight into other decay channels explaining the higher average multiplicity per event and the gap between the two charge distributions in channels with $Z = 14$. The data set obtained after applying the filter (lower panels in Fig. 4.21) shows the same global peculiarities. Therefore, one can infer that GEMINI++ and HFℓ provide the same statistical description further proving that both can be successfully used for the study of the CN evaporation chain even though HFℓ is more accurate in describing nuclear levels. Considering the single particles multiplicity, shown in Fig. 4.22, it can be noticed that a longer decay chain is favoured by HFℓ. No large variations can be seen in relative differences in *complete events* clearly proving that both data sets are affected by the filter in the same way. These conclusions can be drawn indistinctly for α particles (upper panels) and protons (lower panels).

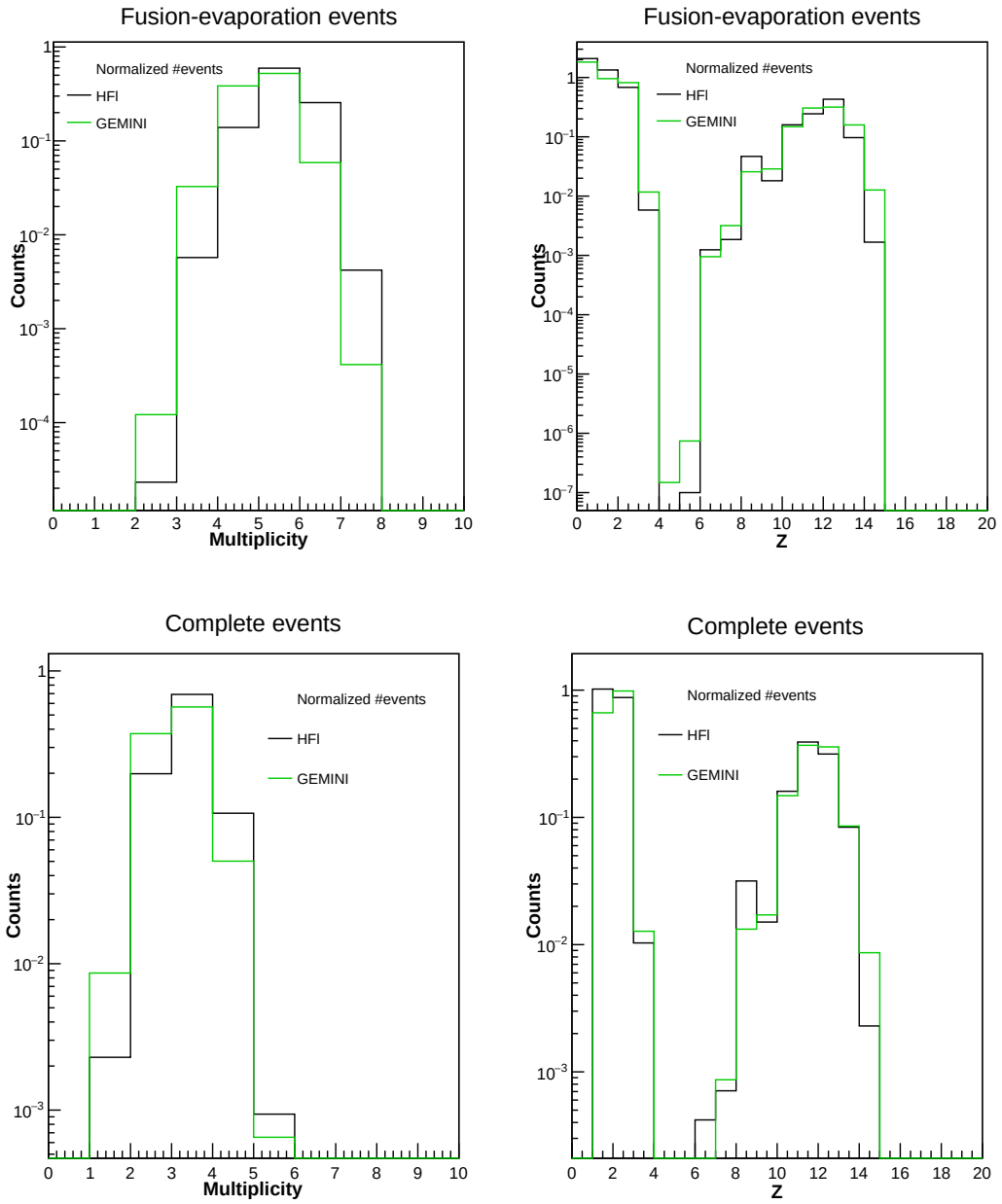

Figure 4.21: Multiplicity (first column) and charge (second column) distributions comparison for GEMINI++ (green) and HFℓ (black) Monte Carlo simulation codes for the ^{18}O+^{12}C reaction at 122 MeV. Upper panels: *fusion-evaporation events*. Lower panels:*complete events*. The distributions are normalized to the number of events.

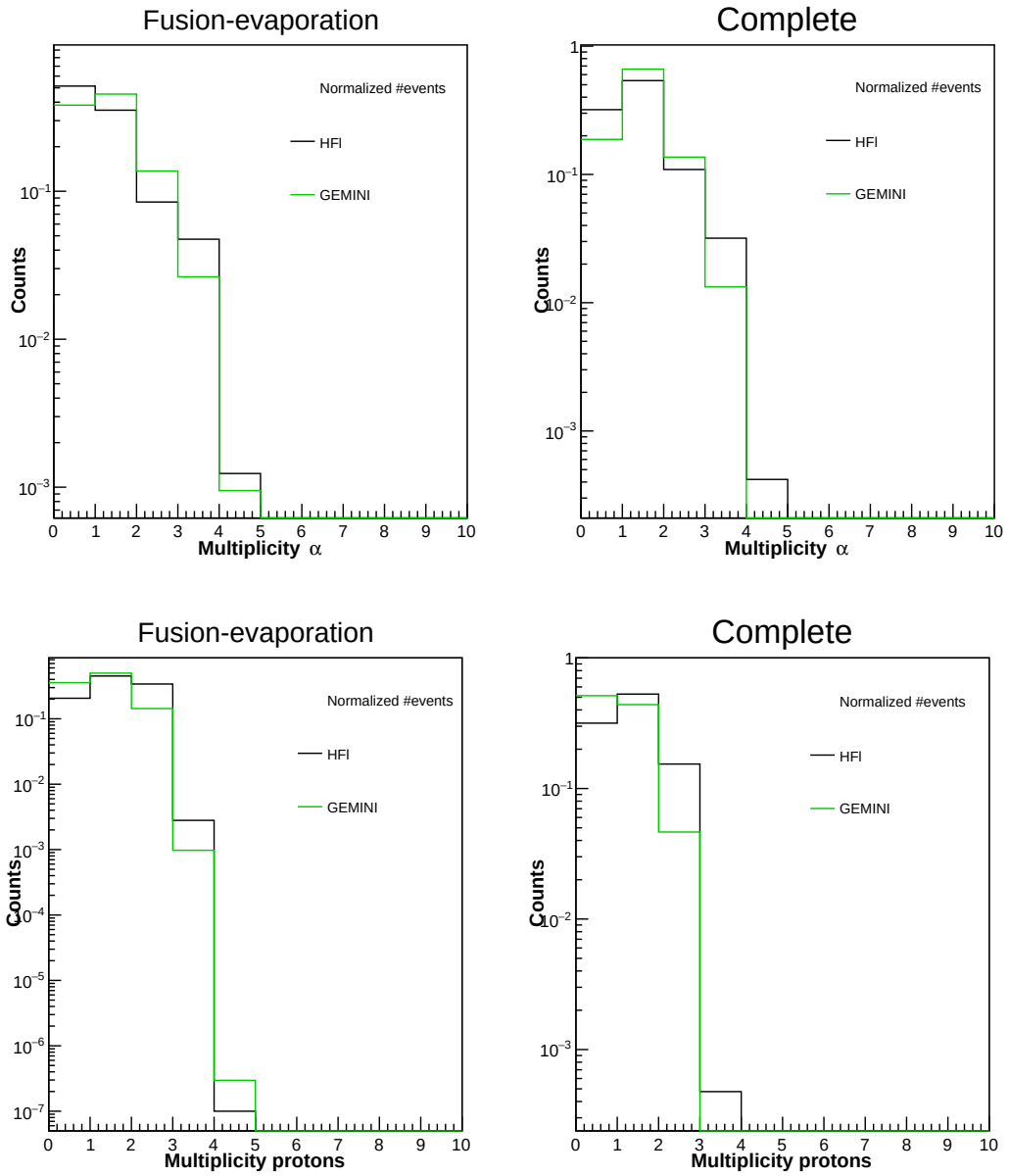

Figure 4.22: Upper panels: α multiplicity distributions comparison for GEMINI++ (green) and HFℓ (black) Monte Carlo simulation codes for the ^{18}O+^{12}C reaction at 122 MeV. Left: *fusion-evaporation events*. Right: *complete events*. Lower panels: proton multiplicity distributions comparison for GEMINI++ (green) and HFℓ (black) Monte Carlo simulation codes for the ^{18}O+^{12}C reaction at 122 MeV. Left: *fusion-evaporation events*. Right: *complete events*. The distributions are normalized to the number of events.

Fig. 4.23 shows the energy spectra of α particles in the center of mass reference frame. The energy peaks from both codes fall on the same values, simulating the two codes the same CN decay. Since in the HFℓ thermal fluctuations of the nuclear surfaces are neglected, its peak is more narrow than the other.

On the other hand, the differing tail slopes indicate that α are emitted by "hotter" sources along the evaporation chain when HFℓ is taken into consideration.

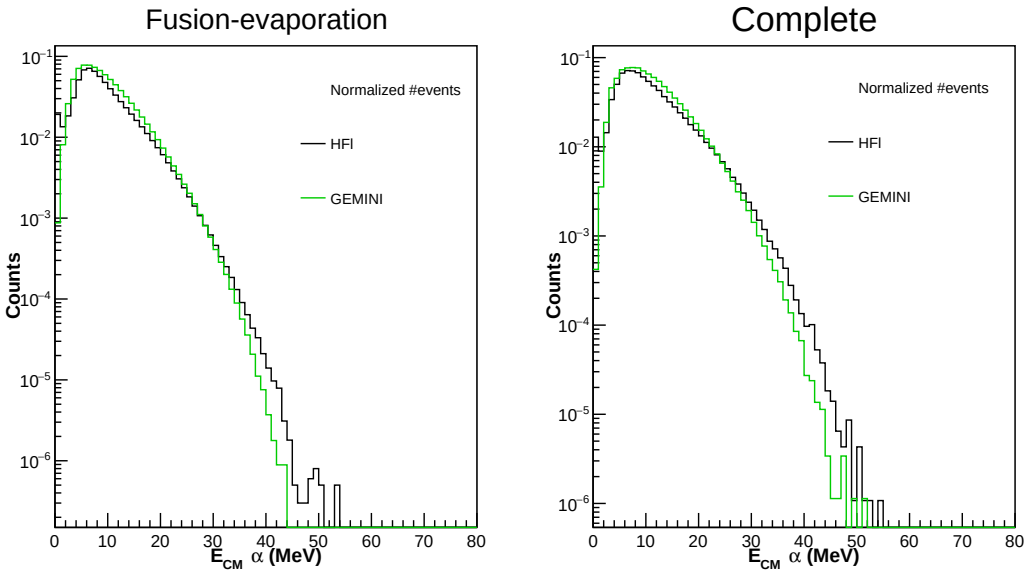

Figure 4.23: α energy spectra in center of mass reference frame comparison for GEMINI++ (green) and HFℓ (black) Monte Carlo simulation codes for the ^{18}O+^{12}C reaction at 122 MeV. Left panel: *fusion-evaporation events*. Right panel:*complete events*. The distributions are normalized to the number of events.

The different parametrization of transmission coefficients in the two codes (Eq. 4.4 and Eq. 4.5) has an evident impact on the energy spectra peaks of protons, as shown in Fig. 4.24. The HFℓ peak undergoes a shift toward higher energy values. Besides, the protons are emitted by "cooler" sources as the shorter tails show. The same conclusions can be drawn when also *complete events* are considered.

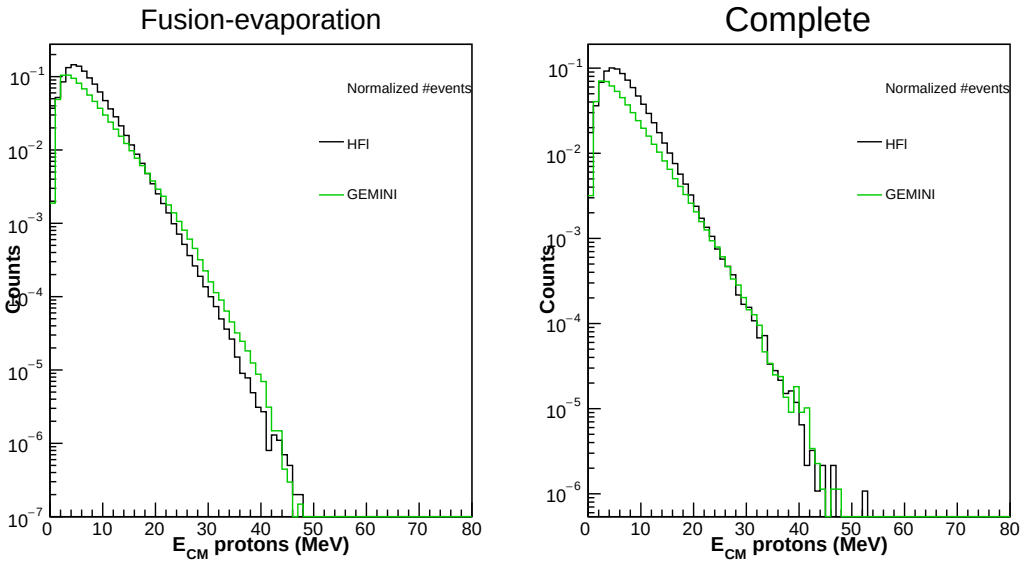

Figure 4.24: Protons energy spectra in center of mass reference frame comparison for GEMINI++ (green) and HFℓ (black) Monte Carlo simulation codes for the ^{18}O+^{12}C reaction at 122 MeV. Left panel: *fusion-evaporation events*. Right panel:*complete events*. The distributions are normalized to the number of events.

Finally, GEMINI++ and HFℓ are expected to generate similar particle polar angle distributions in the laboratory reference frame. Though, especially for α-particle, a discrepancy between the two curves can be observed at smaller angles in the upper left panel of Fig. 4.25.

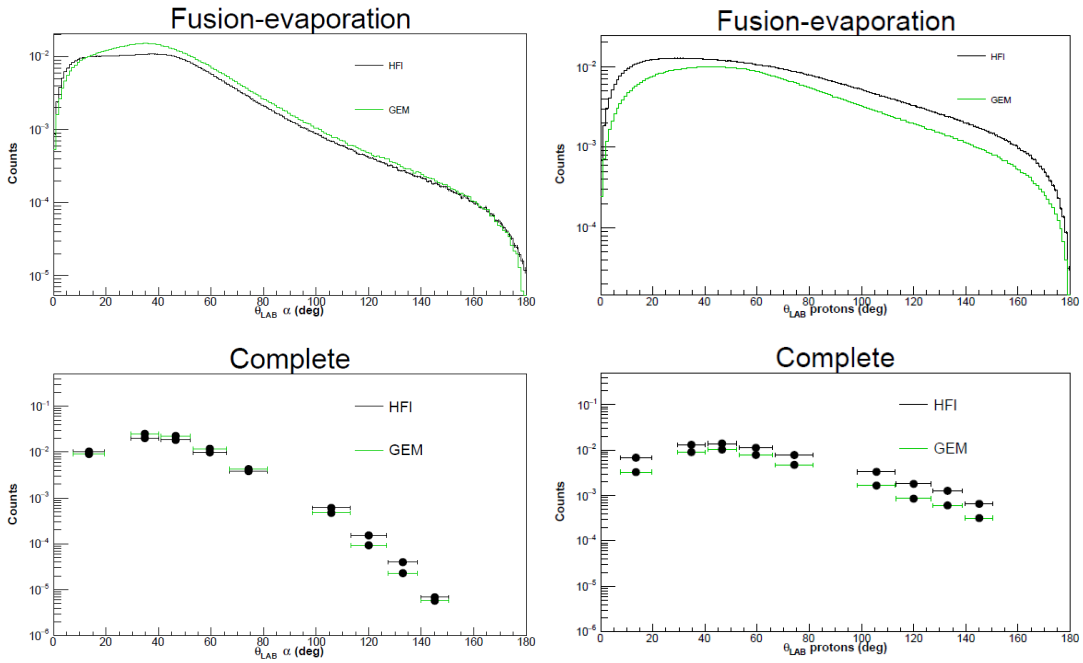

Figure 4.25: Comparison of GEMINI++(green) and HFl (black) angular distributions of α particles (left panels) and of protons (right panels) for the $^{18}O+^{12}C$ reaction at 122 MeV. Upper panels: fusion-evaporation events simulated by the two codes; lower panels: complete ($Z_tot = 14$) filtered fusion-evaporation events. The distributions are normalized to the number of events and to the solid angles.

Being this discrepancy evident in a limited angular region, a possible explanation for this could be a different coverage of neutron emission competition within the two statistical codes. Protons, on the contrary, feature a more uniform trend. After applying the filter, in the various regions the expected behavior is observed for GEMINI++ and HFℓ meaning that the two codes respond to the filter in the same way.

Conclusions and perspectives

Over the years, the INFN NUCL-EX collaboration has studied the light nuclei decay, mainly focusing on possible structure effects. In particular, the comparison of experimental data to statistical-model calculations shows discrepancies that stress non-purely statistical effects in decay channels with even residues, like those due to clusterized structures. In order to investigate the effect of entrance channel structures (like α-clustering) on the decay modes of excited compound nuclei formed in fusion reactions, the ISOLIGHT experiment was proposed. Three different reactions were studied: ^{18}O+^{13}C at 112.5 MeV and ^{18}O+^{12}C at 122 and 300 MeV. The first two produce excited compound nuclei at the same excitation energy (72 MeV), whereas the third indicates whether the cluster structures are present or not at higher excitation energies. The measurements were performed at the Legnaro National Laboratories (LNL) with the GARFIELD+RCo detection array featuring a high geometrical efficiency enabling a reconstruction of complete events.

Within this thesis work all steps into which a nuclear physics experiment with the GARFIELD apparatus is structured were covered. The first part was mainly focused on preliminary operations such as energy calibration of the experimental apparatus and identification of the reaction products. The energy calibration has only been performed for the silicon strip and ionization chamber of the RCo by associating the peak position of the energy spectrum with the expected deposited energy for given particles in specific events, namely elastic scattering reactions. This is the reason why during the experiment some calibration runs with a ^{197}Au target were acquired. This procedure was implemented separately for the ^{18}O+^{12}C at 300 MeV reaction on one side and for the two ^{18}O+^{13}C at 112.5 MeV and ^{18}O+^{12}C at 122 MeV reactions on the other side, being the latter carried out under the same experimental conditions during the same shift of the experiment (February 2021). However, for the first reaction no useful elastic runs have been acquired after the change in the electronic gains in the first part of the experiment. For this reason, the calibration procedure was carried out considering punch troughs in the Si strips of different particles. Concerning the particle identification, $\Delta E - E$ correlations obtained for "telescope" detectors configurations (IC$-$Si and Si$-$CsI(Tl)) and Pulse Shape Analysis (PSA) were used. The impossibility of accomplishing these laborious and time-consuming preliminary operations on the whole experimental set-up

due to the high number of detectors, results in the lack of experimental data for this thesis.

Nonetheless, on the data analysis side, simulated data by Monte Carlo statistical decay code have been analyzed in order to investigate the evolution of fusion-evaporation processes from a statistical point of view. This provides an overview of what is expected from the experimental data once they are completely reconstructed. To this end, firstly GEMINI++ statistical decay code simulating the complex-fragment emission from a hot source was considered in the study of the $^{18}O+^{12}C$ at 122 MeV reaction. In particular, the multiplicity, charge, energy and angular distributions have been investigated in order to determine how the topology of the reaction changes under increasingly stringent data selections, and with the application of the experimental filter simulating the geometry and reconstruction efficiency of the apparatus. Particular attention has been paid to the selection of complete events, made in the same way as in experimental data selections, in order to be compared with experimental data once available. The same variables have been studied within a direct comparison of the three reactions, in the case of fusion-evaporation events and in the case of complete filtered fusion-evaporation events both simulated by GEMINI++.

It has been pointed out that when the CN excitation energy increases, the multiplicity of particles per event becomes higher, whereas the production of protons is mainly affected by the mass of the CN. The energy spectra of α particles reveal a similarity in reactions with different compound nuclei at the same excitation energy. On the contrary, proton energy spectra behave in the same way in reactions producing the same compound nucleus suggesting that the proton emission depends more on the CN than on the excitation energy. These general trends of variables are found to be conserved regardless of the applied conditions.

Eventually, the HFℓ statistical code conceived by the collaboration for the light nuclei decay and containing the details of the known excited levels has been compared with GEMINI++. This was done for the single $^{18}O+^{12}C$ reaction at 122 MeV in order to observe any differences in the description of the fusion-evaporation evolution. The two simulation codes are very well in agreement with some little discrepancies mainly due to the different description of the transmission coefficients and of the pairing coupling.

This thesis work paves the way for further investigations and studies on the reconstructed data in order to highlight possible agreements with the picture described by the theoretical models. In further analyses, the appearance of possible non statistical-effects not reproduced by models can be treated with other methods to confute or confirm the presence of cluster structures.

Appendix A

Commissioning analysis: study of the Rutherford scattering with GARFIELD CsI(Tl)

The GARFIELD array was refurbished in 2019 with newly developed digital electronics and an updated trigger system. The new setup comprises the use of newly developed digitizing boards with better amplitude resolution (14 bits instead of 12 bits) and larger on-board computing power. The FPGAs that replaced the older Digital Signal Processors (DSP) allow us to compute in real time a larger amount of pulse shape analysis parameters, in particular, the current signal obtained by integration from the sampled charge signal. This is particularly important for the silicon detectors for which the upgrade was completed. All the other detectors (gas chambers, CsI scintillators) are now read out by the older DSP electronics and the analog channels have been completely removed. In order to check the functionality of this new electronics, in January 2020 a commissioning experiment was carried out. An ^{16}O-beam at 95 MeV, provided by the TANDEM XTU, impinged on a ^{197}Au-target (100 μg/cm^2) and on a ^{13}C-target (200 μg/cm^2) placed inside the GARFIELD apparatus.

A.1 Preliminary data check

The starting point of any analysis procedure is the good quality of data. For this reason, a preliminary check of the experimental data collected is carried out. Firstly, starting from the raw data, the 2D histogram of the number of hits in each GARFIELD CsI(Tl) is checked by plotting the number of events in each sector vs the number of events in each CsI(Tl) as shown in (Fig. A.1). It highlights that inversions due to wiring are present: in sector 1 the CsI(Tl) 5 (for sake of simplicity named Cs5) and the Cs8 are switched and so are the Cs6 and the Cs7, in sector 8 the Cs5 and the Cs7 and lastly in sector 21 the

Cs6 and the Cs8. Thus, the first phase of analysis is the correction of these inversions

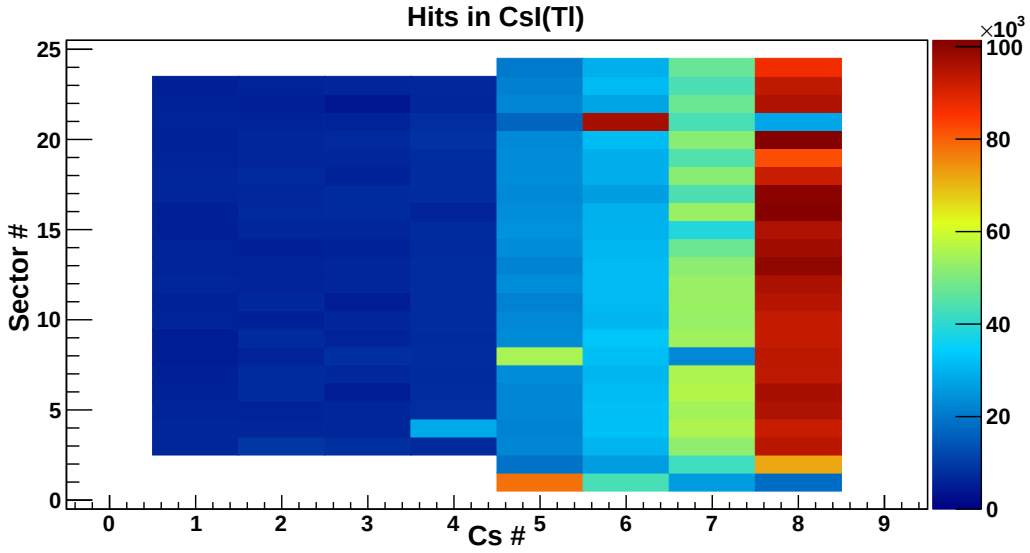

Figure A.1: Number of hits (counts) in each GARFIELD CsI(Tl): 8 CsI(Tl) per each sector; 24 sector in GARFIELD forward, 21 in GARFIELD backward.

(Fig. A.2). At this stage, the general trend of baseline bl and time constant fraction

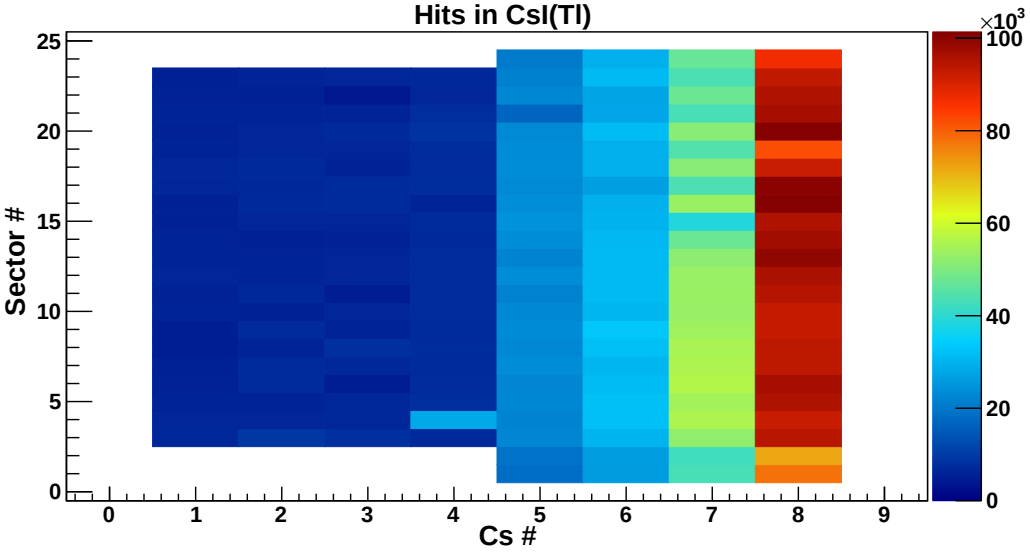

Figure A.2: Same as Fig. A.1, but the inversions are rectified.

discriminator t_{cfd} of signals is studied in order to understand if the application of some

limit conditions or rejection of detectors with evident anomalies are needed. Here follow some of the typical bl and t_{cfd} spectra of both GARFIELD's CsI(Tl) and MSGC. While

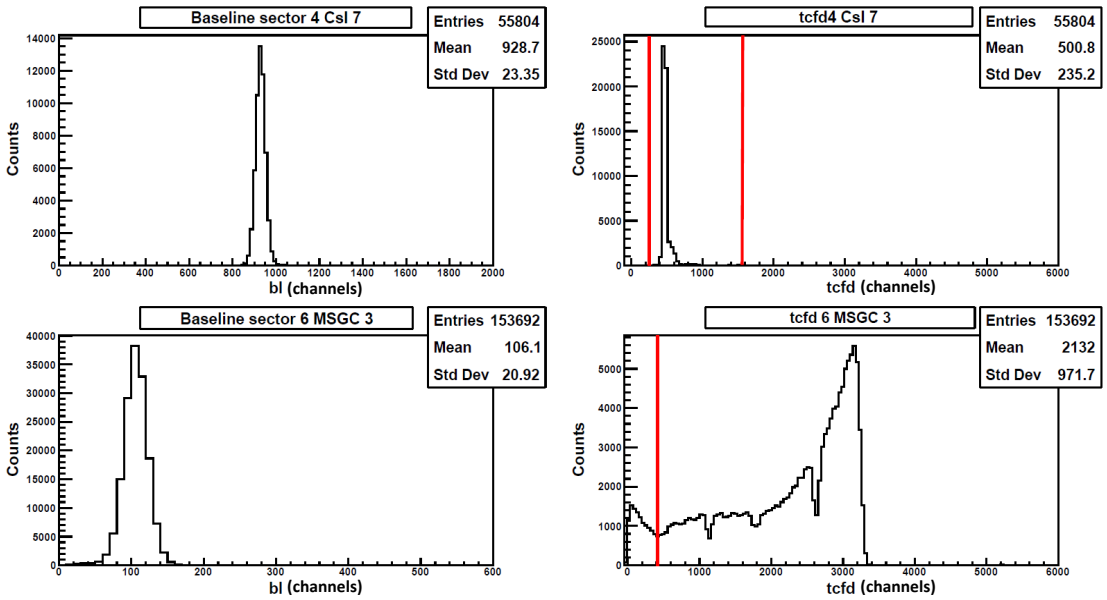

Figure A.3: Typical bl and t_{cfd} of GARFIELD's CsI (as an example, sector 4 CsI 7) and MSGC (as an example, sector 6 MSGC 3). The red line represents the thresholds applied.

the baseline features the expected narrow Gaussian shape around the reference point, CsI and MSGC t_{cfd} require some cuts. For the first ones the criterion applied to set the thresholds is to inspect the spectra on a semi-logarithmic scale in order to exclude tails towards lower and/or higher values, whereas for the latter the noise at lower values is cut away.

A.2 Elastic scattering

Once all the needed thresholds have been applied, the elastic scattering (Section 1.2) is studied on the basis of the signal released by the CsI(Tl) scintillators. Indeed, it is well known that the two components, referred to as *fast* and *slow*, of the output signal of scintillators enable the so-called *Pulse Shape Discrimination*: an isotopic identification in charge and mass of the particles that cross the detector. It follows that, if one plots the *fast vs slow* correlations for the CsI(Tl), the elastic diffusion region is well distinguishable. Indeed, it appears as a halo characterized by a high number of counts in a well defined energy range. This region corresponds to a single type of particle (^{16}O) which maintains its energy (beam energy) thanks to the momentum and kinetic energy conservation in elastic scattering. A trajectory deviation however occurs. In Figs.A.4, the fast-slow correlations for the CsI5-CsI8 of the sector 7 are reported as an example of the elastic diffusion in the CsI(Tl) of GARFIELD forward. Being the elastic diffusion in backward angles very low and comparable with the noise, it has been decided to exclude the CsI 1, 2, 3 and 4 from this analysis.

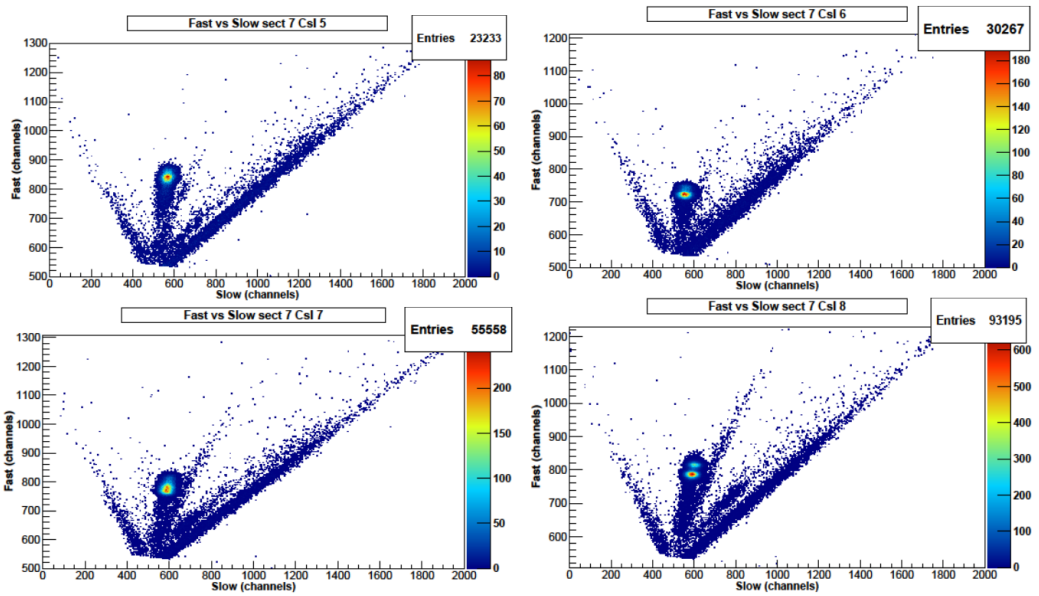

Figure A.4: Upper left panel: *Fast-slow* correlations for the Cs5 of sector 7. Upper right panel: *Fast-slow* correlations for the Cs6 of sector 7. The region of elastic diffusion is clearly recognisable as the one around the more populated bump in red. Moreover, LCP and heavier particles from different reaction mechanisms are also visible in these plots. Lower left panel: *Fast-slow* correlations for the Cs7 of sector 7. Lower right panel: *Fast-slow* correlations for the Cs8 of sector 7.

Primarily, the elastic region is selected by means of a rectangular cut applied to all

the *fast-slow* correlations, as shown in Fig. A.5. Subsequently, a more precise selection

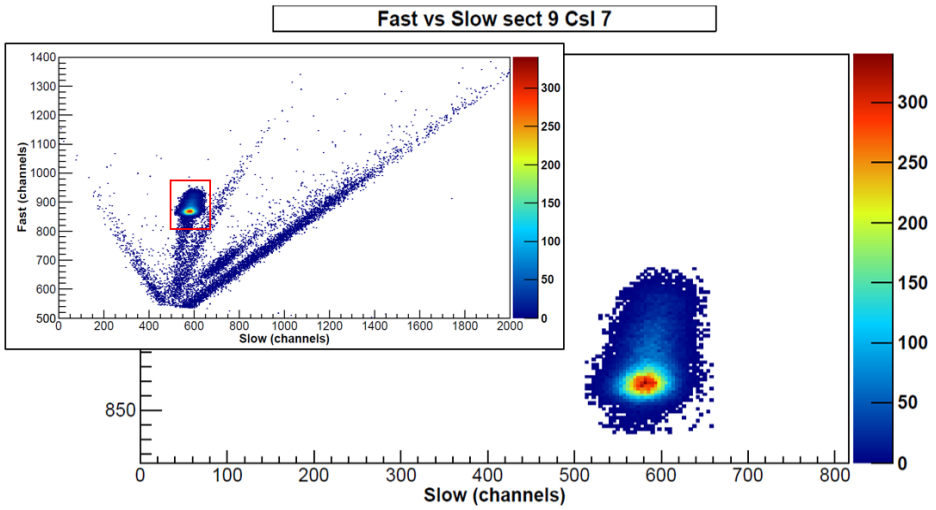

Figure A.5: Fast-slow correlation for CsI 7 of sector 9. The insert shows the full correlation while the underneath panel shows the elastic peak region selected with the red square cut.

of the elastic peak is made considering an elliptical cut (Fig. A.6).

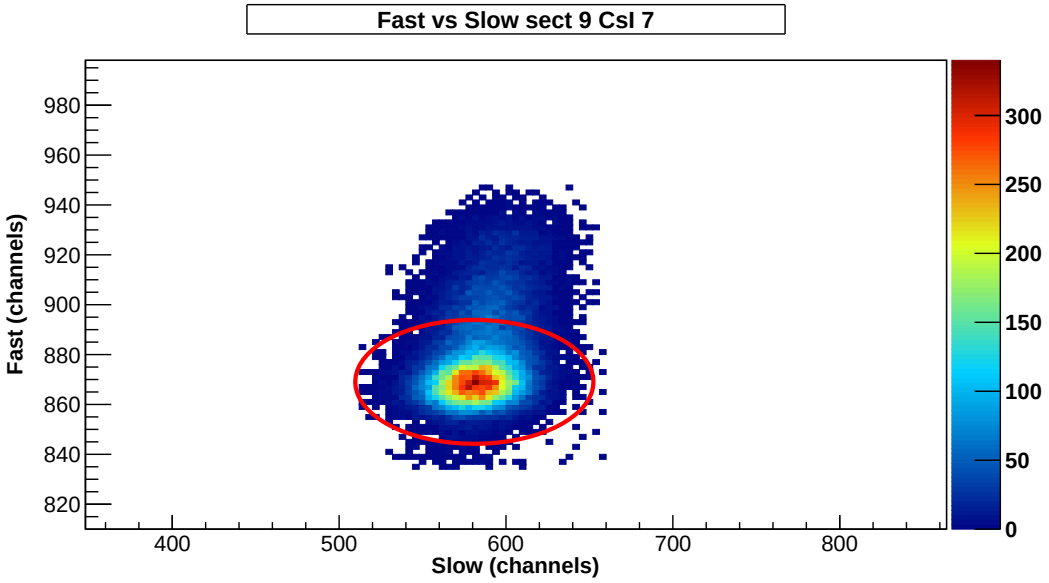

Figure A.6: Elliptical cut to select only the elastic peak.

A.3 Rutherford scattering in GARFIELD CsI(Tl)s

Once the elastic peaks are selected, one can proceed to study the behaviour of such a component as a function of the polar angle (number of CsI). However, in order to compare the yields of the different scintillators, these must be normalized. First of all, all the counts n_{ij} that falls withing the elastic peak selection relating to the same number j (5, 6, 7, 8) of CsI for different sectors i are added up. Afterwards, the sum of the counts N_j is normalized to the number of sectors $\#_j$ in which that particular number of CsI is working. In this way the dependence on the number of functioning CsI(tl) is excluded. Finally, the result is normalized to the solid angle Ω_j subtended by that particular number of CsI. What previously described can be summarized in the following equation:

$$y_j = \frac{N_j}{\Omega_j \, \#_j} = \frac{\sum_{i=1}^{24} n_{ij}}{\Omega_j \, \#_j} \tag{A.1}$$

where y_i is the normalized yield of the ith-CsI. The obtained set of normalized yields referring to the polar angle θ_j of each CsI should follow the typical Rutherford pattern:

$$y_j = A \frac{1}{sin^4(\frac{\theta_j}{2})} \tag{A.2}$$

where θ_j is the mean of θ_{min} and θ_{max} polar angles subtended by each CsI. In Tab. A.1 the mean polar angle, the solid angle and the number of sectors in which each kind of CsI is functioning are reported.

	CsI 5	**CsI 6**	**CsI 7**	**CsI 8**
θ_j [°]	74.25	59.50	46.50	34.75
Ω_j $[sr]$	0.0683	0.0474	0.040	0.0269
$\#_j$	22	21	22	23

Table A.1: Values of mean polar angle, solid angle and number of functioning sectors for each type of CsI.

Eventually, Fig. 1.6 shows the trend of the normalized yields of CsI 5-8 as a function of the polar angle. The interpolation is performed through a 1-parameter function of the kind of equation (A.2) the parameter and error of which are estimated by using the χ^2 minimization.

As far as errors are concerned, a statistic error $\sigma_{n_{ij}} = \sqrt{n_{ij}}$ is associated to each count n_{ij}. It can be noticed that the error on counts is smaller than the size of the point. The

error considered for the polar angle is $\sigma_j = \Delta\theta_j/\sqrt{18}$ since a triangular distribution has been assumed in the angular region covered by the CsI(Tl) crystals.

Moreover, the trend of the normalized yields of CsI belonging to the same sector as a function of the azimuthal angle ϕ was studied. This procedure provides some information about the homogeneity of the particle diffusion. However, in case of inhomogeneous distributions, a misalignment of the beam with respect to the detector could be inferred. Fig. A.7 reports the yields distribution as a function of ϕ of the sectors with the total of four CsI functioning.

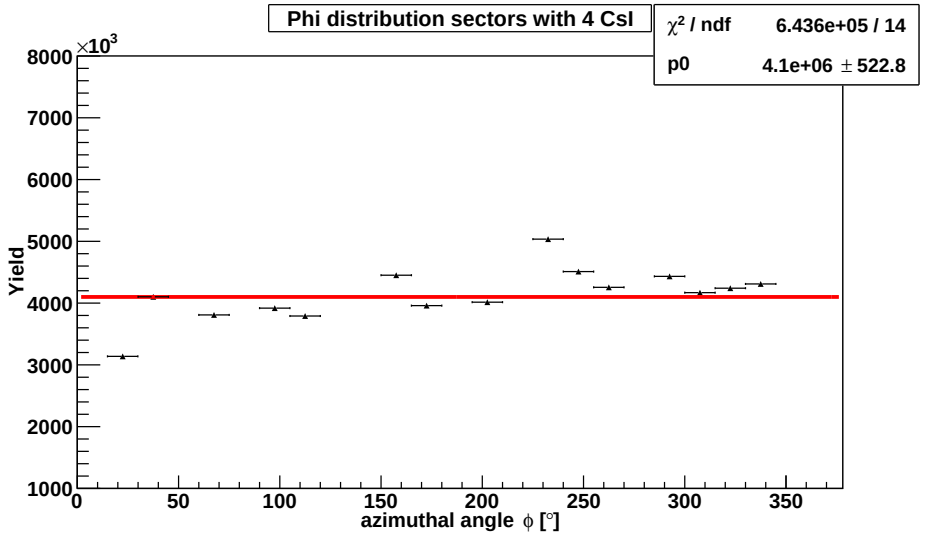

Figure A.7: Azimuthal angle (ϕ) distribution of yields of sectors with 4 working CsI(Tl)s. The black dots represent the experimental yields. The red line is the one-parameter fit function applied.

The plots reported in Fig. A.8 show the azimuthal yields distributions of sectors with CsI 5, CsI6, CsI 7 and CsI 8, respectively. The red lines in the graph represent the linear interpolation with constant ordinate used to fit the distributions. It can be noticed that, the normalized yields overall do not follow an uniform distribution as shown by the high χ/ndf value.

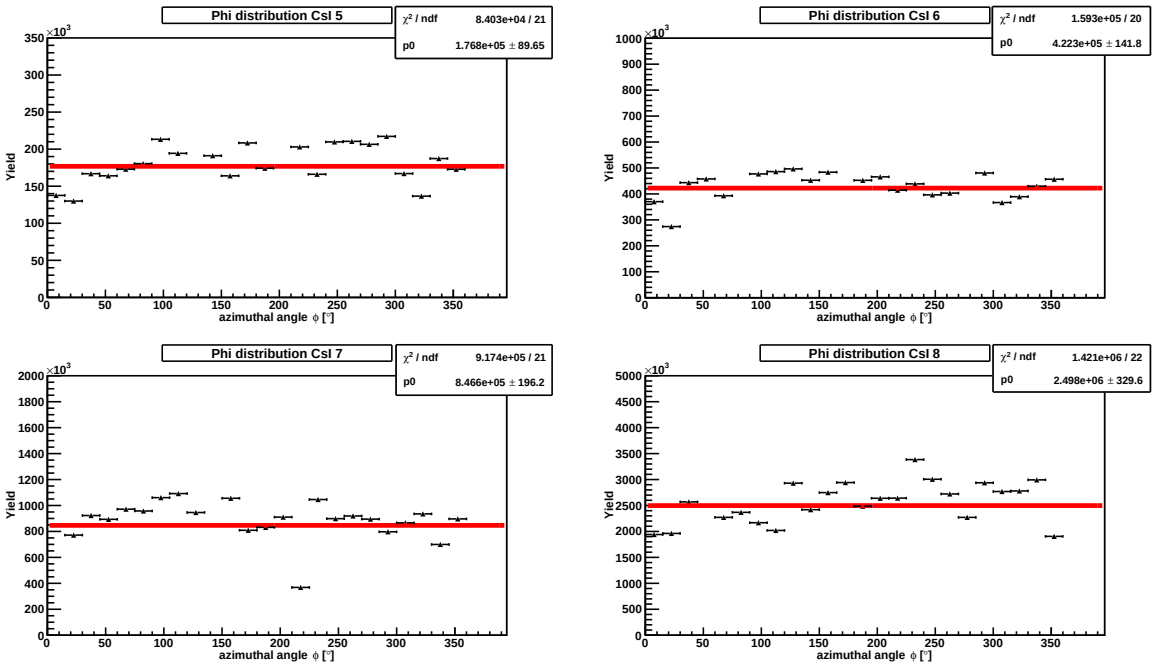

Figure A.8: Same of Fig. A.7, but for the Cs5, Cs6, Cs7 and Cs8 in upper left, upper right, lower left and lower right panels, respectively.

A.4 Conclusions

This commissioning analysis of the elastic diffusion points out that all in all the GARFIELD upgraded acquisition system is properly working. In particular, the digital signal processing shows that the CsI PSA is under control and that the fast and slow variables are well calculated. While the experimental points well reproduce the theoretical curve expected for the polar angle θ distributions of the normalized yields (Fig. **??**), the distributions in the azimuthal angle ϕ feature a dishomogeneity. Nonetheless, no regularity can be observed which might be ascribable to a beam misalignment (Fig. A.7, Fig. A.8). The data dispersion might be attributable to the differing efficiency of the detectors.

Bibliography

[1] NUCL-EX Collaboration INFN: http://www.bo.infn.it/nucl-ex/.

[2] L. Morelli *et al.*, J. Phys. G: Nucl. Part. Phys. **43**, 045110 (2016).

[3] G. Baiocco et al. Phys. Rev. C **87**, 054614 (2013).

[4] A. Camaiani *et al.*, Phys. Rev. C, **97**, 44607 (2018).

[5] K.S. Krane, *Introductory nuclear physics*, ed. John Wiley and Sons (1988).

[6] D. Durand, E. Suraud and B. Tamain, *Nuclear Dynamics in the Nucleonic Regime*, ed. IoP, London (2001). ed. John Wiley and Sons (1988).

[7] R. A. Broglia and A. Winther, *Heavy Ion Reactions* ed. CRC Press Taylor Francis Group, (2018).

[8] G. D. Westfall *et. al.*, Phys. Rev. Lett, **37**, 18 (1976), p. 1202.

[9] S. Braibant, G. Giacomelli and M. Spurio *Particles and Fundamental Interactions*, edited by Springer Science & Business Media (2012).

[10] R. Bass, *Nuclear reactions with heavy ions*, Springer Nature (1980).

[11] P. Fröbrich and L. Lipperheide, *Theory of Nuclear Reactions*, ed. Oxford Science Publications (1996).

[12] M. Bruno *et. al.*, Eur. Phys. J. A **49**, 128, (2013).

[13] W.R. Leo, *Techniques for Nuclear and Particle Physics Experiments: A How-To approach*, Springer, New York (1994).

[14] Bougault *et. al.*, Eur. Phys. J. A. **50**, 47 (2014).

[15] S. Carboni *et. al.*, Nucl. Instr. Meth. A **107**, 145 (2013).

[16] G. Pasquali *et al.*, Nucl. Instr. Meth. A **570**, 126 (2007).

[17] FAZIA Collaboration: http://fazia.in2p3.fr/?lang=en.

[18] C.A.Ur, *The Tandem-ALPI-PIAVE Accelerator Complex of LNL*, AIP Conference Proceedings, Vol. **1530**. No. 1. American Institute of Physics (2013).

[19] Encyclopaedia Britannica: https://www.britannica.com/.

[20] INFN Legnaro National Laboratories: https://www.lnl.infn.it/index.php/en/.

[21] M. Pârlog *et al.*, Nucl. Instr. Meth. A **482**, 693 (2002).

[22] L. Morelli *et al.*, Nucl. Instr. Meth. A **305**, 620 (2010).

[23] S. Valdré, PhD Thesis: *Competition between heavy-ion reaction mechanisms as a function of the system isospin* (2015).

[24] G. F. Knoll, *Radiation Detection and Measurements*, ed. John Wiley and Sons, New York (1989).

[25] C. Frosin, PhD Thesis: *The* ^{16}O+^{12}C *reaction at* 90.5, 110 *and* 130 *MeV beam energy* (2016).

[26] G.Casini *et. al.*, LNL 2004 Ann. Rep., p.215.

[27] C.Frosin *et. al.*, Nucl. Instr. Meth. A **951**, 163018 (2019).

[28] W. Hauser and H. Feshbach, Phys. Rev. **87**, 366 (1952).

[29] Z. Chen and C.K. Gelbke, Phys. Rev. C **38**, 2360 (1988).

[30] NUDAT2 online database: http://www.nndc.bnl.gov/nudat2/